ATOMISTIC-CONTINUUM MECHANICAL MODELS FOR DEFORMATIONS OF SINGLE-WALLED CARBON NANOTUBES

A Dissertation

Presented to the Faculty of the Graduate School

of Cornell University

in Partial Fulfillment of the Requirements for the Degree of

Doctor of Philosophy

by

Karthick Chandraseker

January 2009

ATOMISTIC-CONTINUUM MECHANICAL MODELS FOR
DEFORMATIONS OF SINGLE-WALLED CARBON NANOTUBES

Karthick Chandraseker, Ph.D.
Cornell University 2009

Carbon nanotubes (CNTs) are nanometer sized cylinders made of carbon atoms which possess extraordinary electrical, thermal, and mechanical properties. Their potential applications include such diverse areas as conductive and high strength composites, energy storage and conversion devices, sensors, field emission displays and radiation sources, hydrogen storage media, and nanometer sized semiconductor devices, probes and interconnects. A single-walled carbon nanotube (SWNT) is a CNT formed from a single atomic layer comprised of a hexagonal network of carbon atoms that has been rolled up to form a seamless, hollow cylinder, and it is of interest to understand how the underlying atomic structure determines its macroscopic properties. The present dissertation deals with models to study the influence of atomic structure on the macroscopic mechanical properties of SWNTs.

In describing such atomic systems, all-atom simulations using appropriate energetic descriptions are accurate, and often employed. However, these are limited by computational expense to a small number of atoms and time steps. Alternatively, continuum models capture a collective behavior of atoms and are computational efficient. However, the accuracy of traditional continuum models suffers from surface, interface and size effects, and ambiguities in model parameters. Hence, there is a need to develop atomistically enriched continuum models which combine the accuracy of all-atom simulations and the efficiency

of continuum analyses.

The present dissertation focuses on two zero-temperature, atomistically enriched, large-strain, elastic continuum models to study mechanical deformations of SWNTs – (i) a two-dimensional, quasicontinuum membrane model, and (ii) a one-dimensional rod model. The membrane SWNT model has been employed in prior, published work to predict localized effects such as buckled mode shapes of the effective continuum in severe twist and bending deformations. In the present dissertation, modifications to the existing membrane model are proposed, and implemented in studying coupled extension and twist deformations of SWNTs. The rod model is motivated by the need to model global behavior of long SWNTs in which the aforementioned localized effects are not of significant interest. It is a unified, large-strain SWNT model capable of simultaneously accounting for (a) bending, (b) twist, (c) shear, (d) extension, (e) coupled extension and twist, and (f) coupled bending and shear deformation modes. Both the atomistic-continuum SWNT models in the present dissertation demonstrate the benefits of accounting for important anisotropic and large-strain effects as improvements over employing traditional, linearly elastic, isotropic, small-strain, continuum models. It is envisioned that the ideas presented in this dissertation can be extended to other atomic systems such as silicon or boron nitride nanotubes by use of appropriate lattices and energetic descriptions.

BIOGRAPHICAL SKETCH

Karthick Chandraseker was born on Aug 9, 1982 in Kolkata (Calcutta), India. He was raised in Chennai (Madras), India, where he did his schooling at Padma Seshadri Bala Bhavan Senior Secondary School and Junior College. He then joined the Indian Institute of Technology, Madras (IIT-Madras) in 1999 for his Bachelor's degree in Naval Architecture and Ocean Engineering. Following his graduation from IIT-Madras in 2003, Karthick moved to the United States of America to pursue his Ph.D. at Cornell University in Ithaca, NY. He spent three months, each during the summer of 2006 and Fall of 2007, working at the General Electric (GE) Global Research Center in Niskayuna, NY. Following his graduation from the Department of Theoretical and Applied Mechanics at Cornell University, Karthick will join the Lifing Technologies Laboratory at the GE Global Research Center in Niskayuna, NY, where his work will primarily involve solid mechanics and materials modeling.

To Amma, Appa, and Kavitha.

ACKNOWLEDGEMENTS

I am indeed thrilled to be in this position of writing a note of appreciation to all who have supported and wished me well.

I consider it fortunate to have been under the mentorship of Professor Subrata Mukherjee, my dissertation supervisor and chair of my special committee. His contributions extend far beyond technical advice on my research. His patience, availability, understanding, enthusiasm, and sustained encouragement at all times form key ingredients of this dissertation. I am indebted to him for his willingness to share his immense academic experience, and for several conversations that have helped me gain perspective outside of academic work.

My thanks are due to Professor Timothy Healey and Professor Tomás Arias for serving on my committee, and for valuable suggestions during the course of my dissertation work. In particular, I wish to acknowledge Professor Healey's course on 'Nonlinear Elasticity' and his many insights into the Cosserat rod model which forms the basis of Chapter 5 in the present dissertation, and Professor Arias' course on 'Computational Physics' that introduced me to density functional theory and related numerical methods. My thanks are due to Jeffrey Paci (University of Victoria) and Professor George Schatz (Northwestern University) for their valuable collaboration on the rod model which forms part of Chapter 5 in the present dissertation. I wish to thank Professor Paul Dawson for useful discussions pertaining to the two-dimensional membrane model in Chapter 3 of this dissertation, as well as several of the Cornell faculty whose courses played a valuable role in my educational experience at Cornell. I have also greatly benefited from members of the Cornell faculty with whom I have worked as a teaching assistant – to them I owe the teaching experience I have gained at Cornell.

I cannot understate the company of my friends in Ithaca, whose names I refrain from listing for the sole fear of missing out a few. Their presence has been a great source of inspiration and entertainment. I owe greatly to them for making my stay in Ithaca an enriching experience.

I wish to thank my teachers from high school, junior college and undergraduate studies at IIT-Madras, my long-standing friends, as well as family members for their wishes, valuable support and faith over the years.

No acknowledgement could possibly be complete without thanking my parents and my sister for their unconditional affection and unstinting support in all my endeavors.

Finally, I wish to acknowledge the financial support towards this dissertation – Grant # EEC-0303674 of the National Science Foundation to Cornell University, and teaching assistantships from the Department of Theoretical and Applied Mechanics, as well as the Sibley School of Mechanical and Aerospace Engineering at Cornell University. Grant # CHE-0550497 of the National Science Foundation to Northwestern University enabled the collaboration with Jeffrey Paci and Professor George Schatz on the rod model.

TABLE OF CONTENTS

LIST OF TABLES

LIST OF FIGURES

CHAPTER 1

INTRODUCTION

Recent developments in micro- and nano-manipulation of systems have ushered in a new era of modeling efforts, which seek to validate experiments as well as provide a framework to predict and explain behavior difficult to observe experimentally. Such efforts have also been inspired by materials in which extraordinary macroscopic properties emerge from their underlying atomic structure. An example of such a material is a carbon nanotube (CNT) – a nanometer sized cylinder made of carbon atoms. CNTs possess remarkable strength and ductility, and can be either electrically conducting or semi-conducting based on their underlying atomic structure. These intriguing properties of CNTs, some of which stem from the close connection between CNTs and graphite, have aroused a strong interest in their possible use in nano-electro-mechanical systems (NEMS) such as nanowires, or as active components in electronic devices such as field-effect transistors.

A single-walled carbon nanotube (SWNT), which is the primary system of study in the present dissertation, is a CNT formed from a single atomic layer comprised of a hexagonal network of carbon atoms that has been rolled up to form a seamless, hollow cylinder (Figure 1.1). Depending on the axis about which the planar sheet is rolled up, the SWNTs formed may be categorized into chiral, armchair, and zigzag ones (Figure 1.1). SWNTs are the fundamental structural units that form the building blocks of other atomic systems such as multi-walled CNTs, nanotube ropes and rings, and offer exciting potential applications in diverse areas utilizing their superior mechanical, electrical, thermal, and optical properties. Among the many applications of SWNTs is a NEMS

oscillator. This is of interest in attogram sensitive mass detection of airborne pathogens, radio-frequency signal processing, and as a model system for investigating quantum phenomena in macroscopic systems.

Electrical actuation and detection of guitar-string oscillation modes of clamped SWNT oscillators [75] have shown that the resonance frequencies can be widely tuned (3 – 200 MHz), and that the devices can be used to transduce small forces (force sensitivities of about 10^{-15} N $Hz^{-1/2}$) [75]. These experiments motivate studies of large, elastic deformations of SWNTs in a dynamic, coupled electro-mechanical setting in which electronic properties such as the band gap have also been observed to change with mechanical deformations [77]. However, there are intrinsic difficulties in experimentally carrying out such studies with challenges in dispersing, sorting, and placing CNTs on a substrate [25, 75]. Hence, accurate modeling and simulation tools are necessary to drive these efforts, and understand how atomic structure determines macroscopic properties of such materials. The present dissertation deals with models that account for the influence of atomic structure on the macroscopic mechanical properties of SWNTs.

Characterization of the mechanical properties of SWNTs using elastic moduli such as the Young's modulus, Poisson's ratio, or the flexural rigidity has been the subject of several studies [35, 48, 53, 68, 74]. The assumption of elastic behavior stems from the observation of SWNTs undergoing large, reversible deformations [42, 99] without developing lattice defects, in spite of reports of brittle fracture [100], and computational predictions of the onset of plastic deformations [61, 80].

Methods to characterize elastic properties of CNTs can be broadly classified

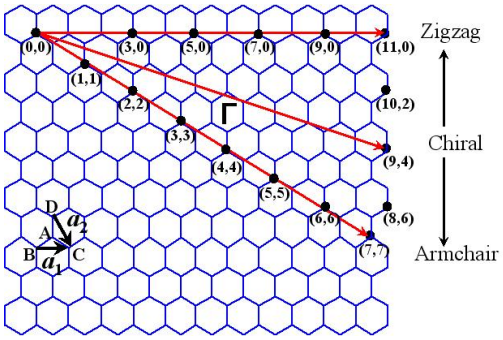

(a) Rolling of a planar graphene sheet into an SWNT

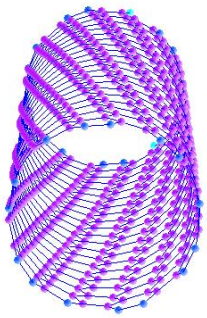

(b) A chiral $(9, 6)$ SWNT

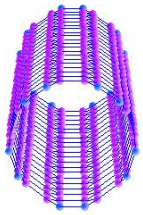

(c) An armchair $(5, 5)$ SWNT

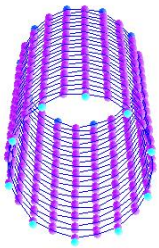

(d) A zigzag $(10, 0)$ SWNT

Figure 1.1: Rolling of a planar graphene sheet into SWNTs drawn on the same scale. Figures (b,c,d) have been produced using the software in [57].

into atomistic or continuum-based approaches. Atomistic methods to extract elastic constitutive properties for CNTs include tight-binding models [40], *ab initio* calculations [48, 74, 88], or use of analytic potentials [16, 66, 67]. Such approaches can be computationally expensive and suffer from the limitations of approximate polynomial fits or finite-difference approximations of derivatives which can lead to significant numerical errors [74]. Moreover, these approaches do not provide information about the relation between the continuum properties and the atomistic potential. All-atom molecular dynamic (MD) simulations using appropriate energetic descriptions are accurate, and often em-

ployed to obtain an atomic-scale description of systems such as CNTs, as well as biomolecules and biological processes. However, computational expense severely limits the size of atomic systems and time scales that can be studied using MD to obtain meaningful information. For example, the current limitations on computer power permit simulations of around 10 million integration steps, i.e., in the multi-nanosecond range, which is short by a factor of around 1000 million for many important biological processes [90].

On the other hand, elastic continuum models can be useful to study long-range phenomena of extended atomic systems since they capture a collective behavior of atoms and offer computational efficiency by reducing degrees of freedom. However, in spite of the robustness and economy of continuum mechanics, use of traditional continuum models for CNTs can lead to inconsistencies [96] due to surface, interface and size effects, and ambiguities associated with model parameters such as elastic moduli and CNT wall thickness taken from the literature. Hence, there is a need to develop atomistically enriched continuum models which combine the accuracy of all-atom simulations and the efficiency of continuum analyses.

The present dissertation focuses on two zero-temperature, atomistically enriched, large-strain, elastic, continuum models (referred to as atomistic-continuum models in the present dissertation) to study mechanical deformations of SWNTs – (i) a two-dimensional, quasicontinuum membrane model, and (ii) a one-dimensional rod model. In both these models, the SWNT is treated as a hyperelastic material, i.e., an ideally elastic material for which the stress-strain relationship derives from a strain energy density function, with the capability to account for material as well as geometric nonlinearities that may arise in large-

strain regimes. Sections 1.1 and 1.2, in the following, respectively contain a summary of different atomistic and continuum descriptions applicable to modeling SWNTs. The two SWNT models presented in this dissertation are also placed in the context of the described approaches.

1.1 Atomistic energy descriptions

Atomistic energy descriptions can be broadly classified into *ab initio*, empirical, first-principles, and semi-empirical ones.

Ab initio approaches such as the post-Hartree-Fock schemes [18] provide approximate solutions to the electronic Schrödinger's equation for the atomic system. This makes them highly transferable, quantitatively reliable, and amenable to systematic control of accuracy through choice of basis set size or sampling of the first Brillouin zone (FBZ). However, they tend to be restricted to either periodic systems or small collections of atoms because of their computational expense.

Empirical potentials such as the Lennard-Jones pair potential [49] and the Tersoff-Brenner multi-body potential [8, 9, 86] contain parameterized, closed-form expressions for the energies between atoms in terms of bond lengths and orientations by taking into account the influence of surrounding atoms up to a certain radius of influence. Parameters in the potentials are usually fit to experiments or *ab initio* simulations based on specific physical criteria. Hence, empirical potentials can suffer from the limitations of transferability from one system to another. However, they offer tremendous computational savings, and hence can be applied to large atomic systems. Further, closed-form expressions

enable analytic evaluation of derivatives as required in computations of stresses and forces, although the accuracy of the results is limited by the extent of applicability of a given potential to a certain atomic system.

The first-principles method, density functional theory (DFT), is currently the most popular way of performing electronic structure calculations [41, 46]. It provides a rigorous reformulation of Schrödinger's equation for a many-electron system into a problem of estimating the wave function and corresponding energy of an effective single-electron system. While this approach is exact, it is stated in terms of an unknown exchange and correlation functional. A large number of approximate expressions for this unknown functional have now been developed (such as the local-density-approximation (LDA) [41, 46]) which can frequently provide accurate predictions for the structure and energetics of systems that contain less than about 200 atoms. In Chapter 4 of the present dissertation, DFT is employed to estimate Young's moduli of representative chiral, armchair and zigzag SWNTs.

As a means to trade-off accuracy and computational expense in performing atomistic simulations, various approaches have been developed that attempt to exploit the benefits of *ab initio* and empirical approaches, and hence termed as semi-empirical methods. Semi-empirical methods such as PM3 [82, 83] or AM1 [19] are based on approximations such as the Neglect of Differential Diatomic Overlap (NDDO) [65], and obtain some parameters from empirical data. They are important in treating large molecules where *ab initio* methods can be expensive while empirical methods may be inaccurate.

In the present dissertation, the empirical Tersoff-Brenner potential [8, 86] is used to model interatomic energies in the two-dimensional, quasicontinuum

membrane SWNT model [3, 14, 101] (Chapters 2, 3, and 4). It is demonstrated that the use of this potential can lead to numerical results that depend on the values of the empirically fit parameters in the potential, as mentioned previously in this section. Chapter 4 on the two-dimensional, quasicontinuum membrane model also contains a computation of the Young's modulus for representative SWNTs using a DFT approach.

The atomistic simulations for the one-dimensional rod model (Chapter 5) are performed using a density-functional-based tight-binding (DFTB) method [21, 22, 27] maintaining self-consistency in electronic charges (SCC). This semi-empirical method is best viewed as an approximation to DFT, and is parameterized based on LDA-DFT calculations. It has been tested and shown to reproduce, quite accurately, the mechanical properties of brittle materials such as diamond, CNTs, and graphene, as predicted by DFT, while being on the order of 100 times faster than DFT based on first-principles [21, 22, 27].

1.2 Elastic continuum models of SWNTs

Elastic continuum models of SWNTs can be broadly classified into one-, two-, and three-dimensional ones.

An example of a three-dimensional SWNT model is a space truss network with linearly elastic, isotropic bars representing carbon bonds and atomic locations represented by nodes in a network [50] that assumes a fixed connectivity between carbon atoms in an essentially molecular-mechanics-based approach. The atomic interactions are assumed to be captured through tensile, flexural, and torsional rigidities in the connecting bars, and the corresponding stiffness

properties are computed in terms of force field constants of an assumed interatomic potential. Such a model makes assumptions on the geometry and dimensions of the bars. Further, it takes into account all the atoms in a given SWNT segment without any coarse-graining, and can hence be computationally expensive.

Two-dimensional continuum SWNT models have been based on an elastic, thin-shell model with the Young's modulus and wall thickness as input parameters assumed from other calculations [63]. In the large-strain regime, the quasicontinuum approach, proposed originally for bulk crystals [79, 84, 85], has been used for atomistic-continuum modeling of mechanical deformations of CNTs [2, 3, 12, 13, 14, 44, 52, 101] to derive a hyperelastic, membrane model based on the empirical Tersoff-Brenner interatomic potential [8, 86] to describe atomistic energies. It is noted that this membrane model possesses a bending stiffness (unlike a traditional membrane) that arises out of the changes in bond angles that are captured by the Tersoff-Brenner interatomic potential (details in Chapter 2), and in this sense, is similar to a shell model. The quasicontinuum, membrane SWNT model has been employed in the past [2, 3, 14, 44, 101] to obtain SWNT elastic moduli [3, 14, 44, 101], as well as study rippling and buckling modes in severe bending and twist deformations [2, 3]. As mentioned previously, this is one of the SWNT models detailed, subsequently, in the present dissertation (Chapters 2, 3, and 4). The key contributions of the present dissertation to the membrane model are summarized in Section 1.3.

Finally, one-dimensional models of SWNTs have been based on the Bernoulli-Euler beam model [28] in order to study their transverse strengths, bending, and vibrational properties (for example, in [75, 87]), with the Young's

modulus and wall thickness as input parameters assumed from other calculations. Although this approach may be sufficient to compute linearized material properties of the effective continuum, it is restricted to small strains, and assumes that the continuum is isotropic and linearly elastic. In [34], the authors present a modified Cosserat rod approach applied to SWNTs with deformable cross-sections. Although this model is capable of large deformations, it still assumes the material to be linearly elastic and isotropic. In the present dissertation, an atomistic-continuum rod model of SWNTs is developed which can exhibit geometric as well as material nonlinearity [38]. The notable features of this model are summarized in Section 1.3.

1.3 Contributions and organization

The present section summarizes the key contributions and describes the organization of the present dissertation.

- As mentioned in Section 1.2, the quasicontinuum, membrane SWNT model has been employed in the past [2, 3, 14, 44, 101] to obtain SWNT elastic moduli [3, 14, 44, 101], as well as study rippling and buckling modes in severe bending and twist deformations [2, 3]. An important ingredient of this approach is the Cauchy-Born (CB) hypothesis [17, 23, 98] that relates bond lengths to the deformation of the continuum, and its subsequent modifications [2, 3, 13] as necessary for application to SWNTs modeled as curved, two-dimensional membranes. A key assumption in the CB rule is that of the deformation being homogeneous at the atomic scale. The basis of this assumption is investigated, and modifications to

the CB rule to deal with inhomogeneous deformations are proposed in the present dissertation in Chapter 2, and implemented in the context of a specific class of deformations in Chapter 3.

- Prior work on the SWNT membrane model [2, 3, 44, 52, 101] assumes a planar (graphene) reference configuration. In the present dissertation, a cylindrical reference configuration is employed which enables a study of variations in the constitutive properties with diameter and chirality of SWNTs that arise from the anisotropy and change in strain energy resulting from the finite deformation required to roll up a planar graphene sheet into an SWNT [2, 3].

- Examples of the three configurations of SWNTs – chiral, armchair, and zigzag – are shown in Figure 1.1(b-d). As an illustration, it is seen that chiral SWNTs contain a helical arrangement of atoms which can cause them to twist when extended and vice versa. Further investigation on the helical idealization of SWNTs can be found in Chapter 5 and Appendix B. In the present dissertation, this coupling behavior is investigated in Chapter 3, as well as taken into account in determining constitutive properties in Chapter 4.

- The one-dimensional rod model of SWNTs developed in the present dissertation (Chapter 5) is motivated by the global behavior of long SWNTs (microns in length) of interest in nano-oscillators (for example, in [75, 87]), for which one-dimensional models are computationally more efficient than two-dimensional ones. As mentioned in Section 1.2, the one-dimensional models in the literature are limited by linearly elastic and isotropic material assumptions which do not take into account couplings between deformation modes, such as the extension-twist coupling

described previously. The rod model developed in Chapter 5 is a unified, large-strain approach that takes into account (a) bending, (b) twist, (c) shear, (d) extension, (e) coupled extension and twist, and (f) coupled bending and shear deformations. As noted in [51], coupling responses can modify electronic, thermal, and mechanical properties of CNTs, underscoring their importance in NEMS devices that exploit electro-, thermo-, chemico-, and optico-mechanical response of CNTs. For example, torques produced in multi-walled CNT-based rotational bearings, oscillators, and nanomotor shafts can result in axial strains that can modify the oscillatory response. Conversely, axial strains generated during transverse vibrations of SWNTs can result in torsional strains which not only affect the predicted resonant frequencies of the SWNTs, but can also change their electronic properties. Pulsed voltage biases and laser fields can easily exploit the coupling response to realize tunable rotational oscillators and regulators.

The present dissertation is organized as follows. Chapter 2 describes the two-dimensional, quasicontinuum, hyperelastic membrane SWNT model. Chapter 3 describes the implementation of this membrane model to study kinematic coupling between extension and twist deformations of SWNTs. Chapter 4 describes the implementation of the membrane model to obtain elastic moduli and stress-strain curves for SWNTs subject to coupled extension and twist deformations. Chapter 5 presents the details of the atomistic-continuum, one-dimensional rod model of SWNTs developed in the present dissertation. Chapter 6 concludes the dissertation with some remarks on future work.

CHAPTER 2

TWO-DIMENSIONAL QUASICONTINUUM MEMBRANE MODEL

2.1 Introduction

In the present chapter, the quasicontinuum approach, proposed originally for bulk crystals [79, 84, 85], but which has also been used for atomistic-continuum modeling of mechanical deformations of CNTs [2, 3, 12, 13, 44, 52, 101], is presented, with a focus on applications to SWNTs.

The approach, outlined in Figure 2.1, essentially consists of formulating a hyperelastic, continuum strain energy density function for a two-dimensional continuum representation of the SWNT based on interatomic bond energies over a representative unit cell of the atomic lattice. This, effectively, connects the atomic system to the deformation of the continuum thereby leading to an atomistic-continuum framework. The essential ideas can also be found in other works dealing with the quasicontinuum method for bulk materials [79, 84, 85].

Referring to Figure 2.1, the end goal is to obtain a strain energy density function relating the continuum stress (the second Piola-Kirchhoff stress tensor, $\mathbf{T}$, in a Lagrangian description) and the continuum strain (the Green-Lagrangian strain tensor, $\mathbf{E} = \frac{1}{2}(\mathbf{F}^T\mathbf{F} - \mathbf{I})$, with $\mathbf{I}$ being the second-rank identity tensor) which, for a hyperelastic material, is a function of the continuum deformation gradient, $\mathbf{F}$. The intermediate steps are as follows. First, the continuum deformation gradient, $\mathbf{F}$, is used to relate the undeformed and deformed bond lengths using the CB rule (Section 2.4). This results in the deformed bond lengths being expressed in terms of $\mathbf{E}$. Finally, the deformed bond lengths are used, along with a choice

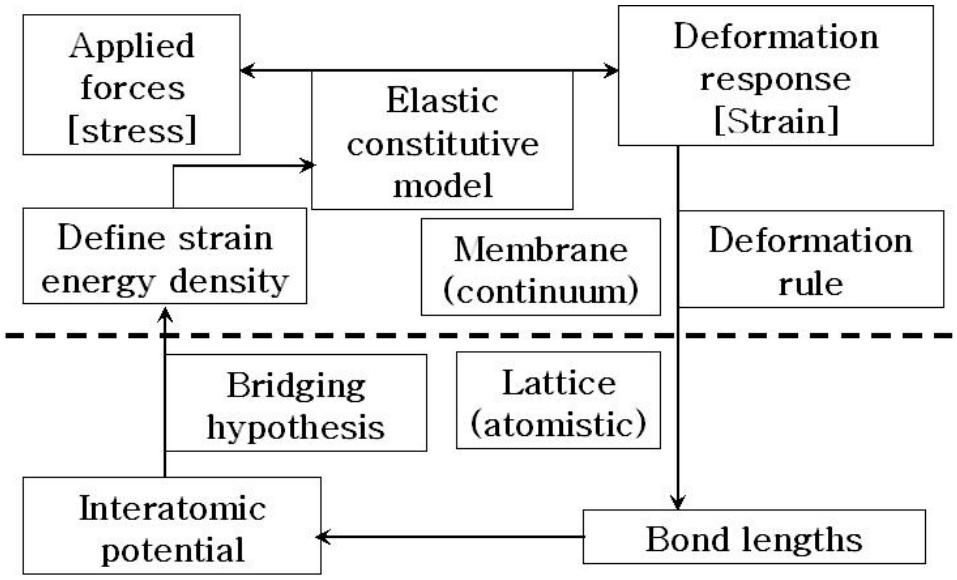

Figure 2.1: Overview of the two-dimensional, quasicontinuum membrane model.

of the interatomic energy description, and an appropriate atomistic-continuum bridging hypothesis, to define a hyperelastic, continuum strain energy density function. The framework was originally proposed for bulk materials [79, 84, 85] and subsequently modified [2, 3, 12, 13, 44, 52, 101] to suit its application to CNTs.

The present chapter is organized as follows. Section 2.2 describes an empirical interatomic potential widely applied to study the mechanics of CNTs. Section 2.3 describes the mapping that converts a planar graphene sheet to a cylindrical SWNT. As will be subsequently elaborated in Chapters 3 and 4, this is essential because it takes into account the anisotropy and change in strain energy that results from the finite deformation required to roll up a planar sheet into a cylindrical tube [3, 14]. Section 2.4 describes the CB rule in its original form applicable to bulk crystals, as well as its subsequent modifications arising from the atomic lattice, curved geometry of the continuum membrane, and in-

homogeneous deformations, required in order to be applicable to SWNTs in this dissertation. Section 2.5 describes the final step in the approach – the atomistic-continuum bridging hypothesis – that results in the definition of a hyperelastic, continuum strain energy density function in terms of the deformed bond lengths and the interatomic potential.

2.2 Interatomic potential description

In the present work on the two-dimensional, quasicontinuum membrane model, a particular interatomic energy description – the empirical Tersoff-Brenner interatomic potential [8, 86] – is employed. This interatomic potential has been widely employed to study the mechanics of CNTs [16, 29, 96], including the nucleation of defects [73, 91]. In the present work, it is assumed that the topology of the bond network does not change, i.e., there is no bond breaking or formation. Following [8], an expression for the bond energy between carbon atoms i and j is

$$V(a(i,j)) = V_R(a(i,j)) - \bar{B}(i,j)V_A(a(i,j)) \quad , \tag{2.1}$$

where $a(i,j)$ is the distance between carbon atoms i and j, V_R and V_A are repulsive and attractive pair terms, respectively, given by

$$V_R(a) = \frac{D^{(e)}}{S-1}\exp[-\sqrt{2S}\beta(r-R^{(e)})]\,f_c(a) \tag{2.2}$$

and

$$V_A(a) = \frac{D^{(e)}S}{S-1}\exp[-\sqrt{2/S}\beta(r-R^{(e)})]\,f_c(a) \quad , \tag{2.3}$$

where $\beta, R^{(e)}, D^{(e)}$, and S are parameters. The term, $\bar{B}(i,j)$ in Equation 2.1, is given by $\bar{B}(i,j) = \frac{1}{2}[B(i,j) + B(j,i)]$, and represents a multi-body coupling between the bond from atom i to atom j, and the local environment of atom i, with

$$B(i,j) = \left[1 + \sum_{k\neq i,j} G[\theta(i,j,k)]\,f_c[a(i,k)]\right]^{-\delta} \quad , \tag{2.4}$$

where δ is a parameter, G and f_c are continuous functions defined as

$$G(\theta) = a_0\left[1 + \frac{c_0^2}{d_0^2} - \frac{c_0^2}{d_0^2 + (1+\cos\theta)^2}\right] \quad , \tag{2.5}$$

where a_0, c_0, and d_0 are parameters, and

$$f_c(a) = \begin{cases} 1 & a < R^{(1)} \\ (1/2)\left\{1 + \cos\left[\frac{\pi(a-R^{(1)})}{R^{(2)}-R^{(1)}}\right]\right\} & R^{(1)} \leq a \leq R^{(2)} \\ 0 & a > R^{(2)} \end{cases} \quad , \tag{2.6}$$

where $R^{(1)}$ and $R^{(2)}$ are parameters. Further, in Equation 2.4, k denotes other carbon atoms besides i and j, and $\theta(i,j,k)$ is the angle between the bonds $i-j$ and $i-k$, which can be expressed as

$$\theta(i,j,k) = \arccos[\frac{a(i,j)^2 + a(i,k)^2 - a(j,k)^2}{2\,a(i,j)\,a(i,k)}] \quad . \tag{2.7}$$

The potential given by [8] contains two sets of values, tabulated in Table 2.2, for the 10 parameters $\delta, a_0, c_0, d_0, R^{(1)}, R^{(2)}, R^{(e)}, D^{(e)}, \beta$, and S.

Table 2.1: Two sets of values for the parameters in the Tersoff-Brenner [8, 86] interatomic potential for carbon.

Parameter	Value (set # 1)	Value (set # 2)
$D^{(e)}$	6.325 eV	6.00 eV
S	1.29	1.22
β	15 nm^{-1}	21 nm^{-1}
$R^{(e)}$	0.1315 nm	0.1390 nm
$R^{(1)}$	0.17 nm	0.17 nm
$R^{(2)}$	0.20 nm	0.20 nm
δ	0.80469	0.5
a_0	0.011304	0.00020813
${c_0}^2$	19^2	330^2
${d_0}^2$	2.5^2	3.5^2

The first set is a good fit with the bond lengths, while the second fits the stretching force constants well. As noted in Section 1.2, the use of this interatomic potential enables the capture of changes in bond angles that leads to a bending stiffness in the membrane model (unlike a traditional membrane) and in this sense, the quasicontinuum membrane is similar to a shell. Throughout the present dissertation, any reference to the quasicontinuum, SWNT membrane model is assumed to refer to this non-traditional, shell-like, membrane model that possesses a bending stiffness.

2.3 Mapping of a planar graphene sheet into an SWNT

In some of the published work dealing with a two-dimensional, quasicontinuum membrane model of SWNTs, such as [44, 52, 101], the SWNT deformation analysis is performed by mapping the deformed SWNT back to a planar sheet, and measuring the energies of the atoms on the SWNT by considering their mapped positions on the cylinder. In the present dissertation, it is consistently assumed that bond lengths are measured as Euclidean distances between atoms on the deformed cylinder, and the energies of atoms are measured in the cylindrical configuration.

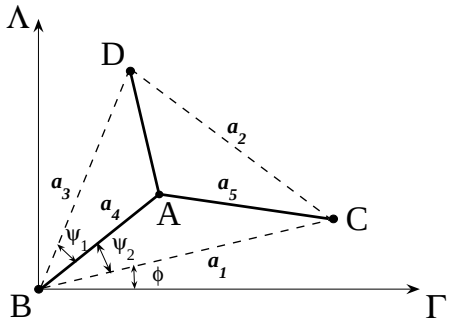

Figure 2.2: A representative atom, A, and its nearest neighbors B, C, D, and bonds AB, AC, AD. $a_1 = \overrightarrow{BC}$ and $a_2 = \overrightarrow{DC}$.

The present section summarizes the computation of cylindrical positions of atoms on an SWNT by mapping a planar graphene sheet to a cylindrical SWNT based on its chirality. This models the rolling process of a planar sheet of graphene into a cylindrical SWNT by minimizing the binding energy of a representative atom in the cylindrical SWNT with respect to certain lengths in the planar graphene sheet.

A representative carbon atom, A, and its nearest neighbors, B, C, D, on a pla-

nar graphene sheet, are shown in Figure 2.2. The vectors $a_k,\ k = 1, 2, 3, 4, 5$, shown in the figure, have lengths a_k. The length of the vector $\overrightarrow{AD}$, as well as the angles ψ_1 and ψ_2 in Figure 2.2, can be obtained as functions of $a_k,\ k = 1, 2, 3, 4, 5$, which are, in turn, computed from minimizing the binding energy of atom A.

The graphene sheet is rolled into a cylinder whose circumferential vector is the chiral vector, $\mathbf{\Gamma}$. Its length is the circumference of the SWNT, so that the diameter of the SWNT is $d = \Gamma/\pi$, where $\Gamma = |\mathbf{\Gamma}|$. The translational vector along the SWNT longitudinal axis, $\mathbf{\Lambda}$, is also denoted in Figure 2.2. Its magnitude equals the axial period of the SWNT. According to the definition of the chiral indices of an SWNT,

$$\mathbf{\Gamma} = na_1 + ma_2 \quad , \tag{2.8}$$

where n and m are integers ($n \geq |m| \geq 0$), and (n, m) is the chirality of the SWNT $-$ $(n, 0)$ is called a zigzag, (n, n) is called an armchair, and the general case $n > |m| > 0$ is called a chiral SWNT (Figure 1.1). Referring to Figure 2.2, it is straightforward to show that

$$\Gamma = \sqrt{n^2a_1^2 + m^2a_2^2 + nm(a_1^2 + a_2^2 - a_3^2)}, \quad \phi = \cos^{-1}\left(\frac{\mathbf{\Gamma} \cdot a_1}{\Gamma a_1}\right) \quad . \tag{2.9}$$

Now, the mapped atomic positions of the points A, C, D in Figure 2.2 in the rolled-up SWNT are considered. In cylindrical polar coordinates, with B as the reference point, it is seen that

$$R(A) = R(B) = R(C) = R(D) = d/2 \quad ,$$

$$
\begin{aligned}
&Z(A) = a_4 \sin(\psi_2 + \phi), \quad Z(B) = 0, \quad Z(C) = a_1 \sin(\phi) \quad , \\
&Z(D) = a_3 \sin(\psi_1 + \psi_2 + \phi) \quad , \\
&\Theta(A) = \frac{2a_4 \cos(\psi_2 + \phi)}{d}, \quad \Theta(B) = 0, \quad \Theta(C) = \frac{2a_1 \cos(\phi)}{d} \quad , \\
&\Theta(D) = \frac{2a_3 \cos(\psi_1 + \psi_2 + \phi)}{d} \quad .
\end{aligned}
\tag{2.10}
$$

Finally, if $a^{(0)}(X, Y)$ denotes the Euclidean distance (which is also the bond length when X and Y are nearest neighbors) between two atoms X and Y ($X, Y = A, B, C, D$), when X, Y are located on the surface of the SWNT, it follows that

$$
a^{(0)}(X, Y) = \sqrt{\frac{d^2}{2}\Big[1 - \cos(\Theta(Y) - \Theta(X))\Big] + (Z(Y) - Z(X))^2} \quad . \tag{2.11}
$$

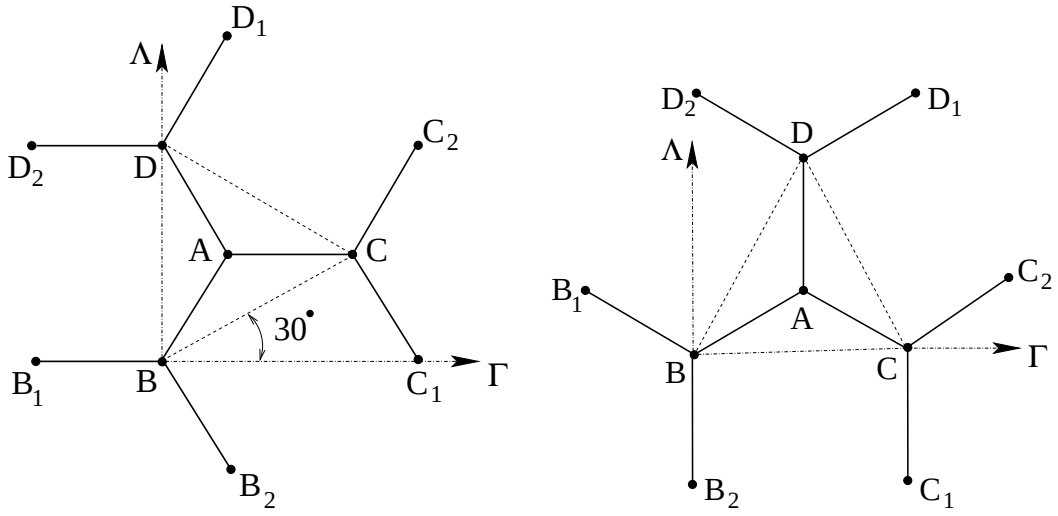

(a) Atomic structure of an armchair SWNT (b) Atomic structure of a zigzag SWNT

Figure 2.3: Atomic structure of armchair and zigzag SWNTs. The figures show nearest neighbors B, C, D of atom A, and the nearest neighbors of B, C, D.

The angle, θ, in Equation 2.5, is obtained from $a^{(0)}(X, Y)$ ($X, Y = A, B, C, D$) by using the cosine rule – Equation 2.7. Given m, n, the parameters in the Tersoff-

Brenner potential (Table 2.2, and the bond lengths $a^{(0)}(X, Y)$, the binding energy per atom (V) associated with atom A (half of the energy from each bond is counted towards the binding energy for atom A) can be written as

$$V = \frac{1}{2}[V(a(A, B)) + V(a(A, C)) + V(a(A, D))] \quad , \tag{2.12}$$

which is now known as a function of $a_k,\ k = 1, 2, 3, 4, 5$. The final step is to minimize the binding energy for atom A. This leads to

$$\frac{\partial V}{\partial a_k} = 0, \quad k = 1, 2, 3, 4, 5 \tag{2.13}$$

to solve for $a_k,\ k = 1, 2, 3, 4, 5$.

$a(B, B_1) = a(C, A)$	$a(D, D_2) = a(C, A)$
$a(B, B_2) = a(D, A)$	$a(C, C_1) = a(D, A)$
$a(C, C_2) = a(B, A)$	$a(D, D_1) = a(B, A)$
$a(A, B_1) = a(C, B)$	$a(A, B_2) = a(D, B)$
$a(A, C_1) = a(D, C)$	$a(A, C_2) = a(B, C)$
$a(A, D_1) = a(B, D)$	$a(A, D_2) = a(C, D)$

Box 1: Relationships between the interatomic Euclidean distances for all SWNTs.

Implementation of Equation 2.4, for the atoms B, C, D in Figure 2.2, requires consideration of the nearest neighbors X_1, X_2 of X, where atom X represents B, C, D (Figure 2.3). The relations needed for including these interactions are listed in Box 1. These relations are used to obtain bond lengths and angles which are required to calculate the binding energy for atom A (Figure 2.3) as

per the Tersoff-Brenner interatomic potential, and hold good during imposed deformation as well, based on assumed periodicity of the graphene lattice.

2.4 The Cauchy-Born rule

This section presents a study of the CB rule as applied to the deformation analysis of SWNTs that are modeled as two-dimensional membranes. The bond vectors in the SWNT are assumed to deform according to the local deformation gradient, as per the CB rule, or a modified version thereof.

2.4.1 Bulk crystals

The CB rule [17, 23] provides a natural, kinematic connection between deformations at the atomistic and continuum scales without other phenomenological input. It enables a relation between deformed and undeformed bond lengths in an atomic lattice by homogenizing the continuum deformation at the atomic scale. Essential ideas can be found in other works dealing with the deformation analysis of SWNTs (for example, in [2, 3, 12, 13, 44, 52, 79, 85, 101]), and are summarized in the present dissertation. The CB rule states that the vector defined by a pair of atoms deforms according to the local deformation gradient, i.e.,

$$\mathbf{a} = \mathbf{F}(\mathbf{X}) \cdot \mathbf{A} \quad , \tag{2.14}$$

where $\mathbf{A}$ refers to the undeformed bond vector, $\mathbf{a}$ refers to the deformed bond vector, and $\mathbf{F}$ refers to the local deformation gradient at material point $\mathbf{X}$. This

hypothesis describes crystal behavior well as long as the continuum deformation is nearly homogeneous in the scale of the crystal. The CB rule (with a homogeneous **F** at the atomic scale) has been successfully applied to space-filling crystals represented as complex Bravais lattices by [79, 84, 85]. However, as will be subsequently elaborated in Chapter 3, the two-dimensional SWNT membrane model in the present dissertation is employed in the context of a class of deformations that is, in general, assumed to be spatially inhomogeneous at the atomic scale. Hence, modifications are necessary to the CB rule to account for possible spatial inhomogeneities in **F**. Further modifications are necessary, to account for the curved geometry of SWNTs, and the two-atom basis of the honeycomb graphene lattice. These modifications are discussed below.

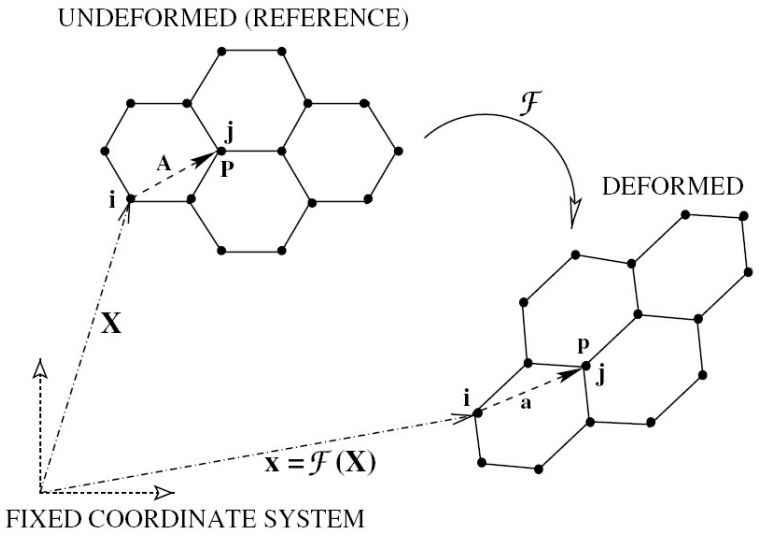

Figure 2.4: The direct map $\mathcal{F}$ ($\mathcal{F}(P) = p$).

2.4.2 Modifications for inhomogeneous deformations

It is demonstrated below that in the case of inhomogeneous deformations at the atomic scale, the CB rule is only approximate. Further, it is shown that, in such

cases, the mean value theorem in calculus [37] can be used as a guide to modify the CB rule (Equation 2.14) to account for the spatial inhomogeneity of $\mathbf{F}$ at the atomic scale. To deal with inhomogeneities such as defects and non-local effects, mixed continuum-atomistic approaches have been proposed by [79, 84] in the context of finite element (FE) formulations.

The following illustrates the relation between the CB rule and the exact expression for the deformed bond vectors in the case of an arbitrary deformation imposed on a bulk solid, in which atoms are assumed to lie in a three-dimensional continuum. From Figure 2.4, and from the map $p = \mathcal{F}(P)$, it is seen that

$$\mathbf{a} = \mathcal{F}(\mathbf{X} + \mathbf{A}) - \mathcal{F}(\mathbf{X}) \quad . \tag{2.15}$$

By expanding the right hand side of Equation 2.15 in a Taylor series about $\mathbf{X}$, and using $\mathbf{F} = \boldsymbol{\nabla}\mathcal{F}$, Equation 2.15 is rewritten as

$$\mathbf{a} = \mathbf{F}(\mathbf{X}) \cdot \mathbf{A} + \frac{1}{2!}\nabla\mathbf{F}(\mathbf{X}) : (\mathbf{A} \otimes \mathbf{A}) + \frac{1}{3!}\boldsymbol{\nabla}\boldsymbol{\nabla}\mathbf{F}(\mathbf{X}) \diamond (\mathbf{A} \otimes \mathbf{A} \otimes \mathbf{A}) + h.o.t \quad , \tag{2.16}$$

where '$\diamond$' denotes the action of a fourth rank tensor on a third rank tensor that results in a vector, ':' denotes the action of a third rank tensor on a second rank tensor that results in a vector, '$\otimes$' denotes the standard tensor product [81], and '*h.o.t*' denotes higher order terms. Equation 2.16 gives the exact expression for the deformed bond vector (as obtained directly from the deformation map) and shows that the deformed bond vector depends not only on $\mathbf{F}$, but on its gradients as well. If $\mathbf{F}$ is spatially uniform, all its gradients vanish, and the Taylor

series reduces to the standard CB rule (Equation 2.14), which becomes exact in this case. Hence, the Taylor series holds the key to the degree of homogenization enforced on $\mathbf{F}$. A key idea to note is that, even in the case of inhomogeneous deformations at the atomic scale, if the deformation map, $\mathcal{F}$, is differentiable on the closed interval $[\mathbf{X}, \mathbf{X}+\mathbf{A}]$, the mean value theorem in calculus [37] guarantees the existence of some $\mathbf{X}_\alpha \in [\mathbf{X}, \mathbf{X} + \mathbf{A}]$ that allows Equation 2.15 to be rewritten as

$$\mathbf{a} = \mathbf{F}(\mathbf{X}_\alpha) \cdot \mathbf{A} \quad . \tag{2.17}$$

This idea provides the basis for modifying the CB rule to account for inhomogeneous deformations at the atomic scale, as will be subsequently discussed in detail in Section 4.2.2, in the context of a particular class of inhomogeneous deformations.

2.4.3 Curved membrane modification

The standard CB rule (Equation 2.14) requires modification to be applicable to two-dimensional membranes (which are, geometrically, two-dimensional manifolds) instead of bulk crystals. In such cases, Equation 2.14 needs to be interpreted in terms of $\mathbf{F}$ mapping tangent vectors to the manifold at point $\mathbf{X}$, from the undeformed to the deformed domains [56]. Here, it is possible to use either a three-dimensional (bulk) $\mathbf{F}$ or a two-dimensional (surface) $\mathbf{F}$ – the actions of both these operators on tangent vectors to two-dimensional manifolds, are identical [81]. In the present work (details in Chapter 3), a three-dimensional deformation gradient evaluated at the surface of the SWNT, is employed. Since

all the carbon atoms are assumed to lie on the same cylindrical surface, this means that there is no radial variation of **F**. Further, in the case of curved membranes, the bond vectors are, in fact, chords and not tangent vectors (and the chord $\approx$ tangent approximation gets worse as the curvature increases). For such domains, the standard CB rule has been extended using the idea of an exponential map [2, 3] and termed as the exponential CB rule. This modification is summarized below.

In this modification, the bond lengths are viewed as intrinsic distances in the two-dimensional continuum, which are essentially geodesics connecting the two atoms on the surface (although, for energetic considerations, the bond lengths are always measured as the Euclidean straight-line distances between carbon atoms). To be able to apply the CB rule in this case, it is necessary to first 'unwrap' the geodesic onto the tangent plane at **X**, then apply **F** to this geodesic vector to obtain the deformed geodesic vector lying on the deformed tangent plane, and finally 'wrap' the deformed geodesic back onto the deformed surface to obtain the Euclidean bond lengths. The exponential map provides the mathematical means to perform the 'unwrapping' and 'wrapping' operations described above. It is noted, from Section 2.4.2, that if a three-dimensional **F** is used in the CB rule with the SWNT atoms assumed to lie in the three-dimensional continuum, the standard CB rule (without any modification, i.e., using the bond vectors as chords) gives the exact solution if **F** is spatially uniform [12]. In such an approach, modifications to the CB rule become necessary only if **F** is inhomogeneous at the atomic scale.

The notion of the exponential map modification to the CB rule is made more specific in the following. The starting point here is the undeformed SWNT with

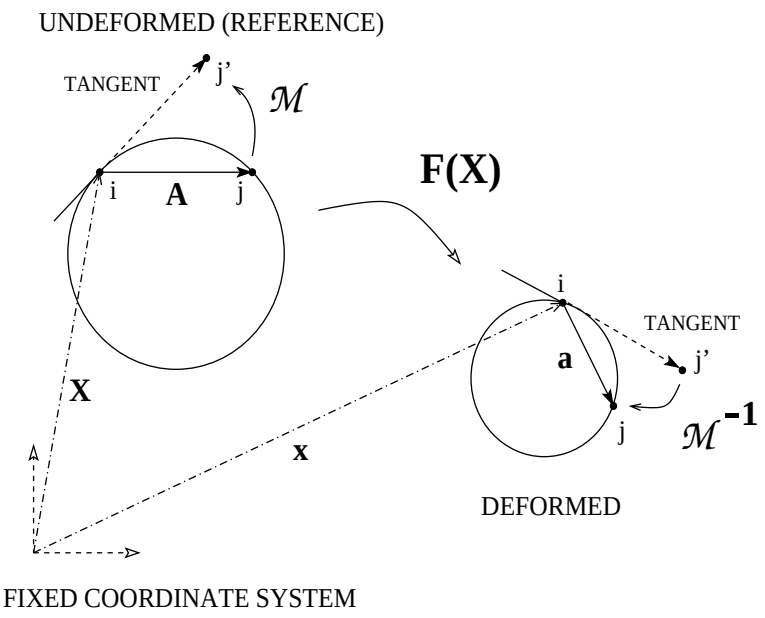

Figure 2.5: The exponential CB rule for SWNTs modeled as two-dimensional, curved manifolds [2].

the atom positions obtained as described in Section 2.3. A continuous deformation denoted by $\mathbf{x} = \mathcal{F}(\mathbf{X})$ is considered, where $\mathbf{X}$ and $\mathbf{x}$ denote the positions of a material point in the undeformed and deformed configurations respectively. The deformation gradient is obtained as $\mathbf{F} = \boldsymbol{\nabla}_{\mathbf{X}}\mathcal{F}$. The Euclidean bond vectors before and after deformation are denoted by $\mathbf{A}$ and $\mathbf{a}$ respectively. As mentioned previously, the exponential CB rule effectively replaces $\mathbf{F}$ in Equation 2.14 by a composition of three operations – an 'unwrapping' of the geodesic connecting the atoms onto the tangent plane at $\mathbf{X}$ (this operation is denoted here by $\mathcal{M}$), operation of $\mathbf{F}$ on this geodesic vector to obtain the deformed geodesic vector lying on the deformed tangent plane, and finally a 'wrapping' of the deformed geodesic vector back onto the deformed surface (this operation is denoted by $\mathcal{M}^{-1}$) to obtain the Euclidean bond lengths.

This sequence is graphically shown in Figure 2.5, and may be expressed as follows:

$$\mathbf{a} = \mathcal{M}^{-1}\mathbf{F}(\mathbf{X})\mathcal{M}\mathbf{A} \quad . \tag{2.18}$$

This results in obtaining the Euclidean deformed bond lengths in terms of $\mathbf{F}$.

2.4.4 Bravais multi-lattice modification

When dealing with an SWNT, special attention needs to be paid to the fact that graphene is a Bravais multi-lattice consisting of two woven simple sub-lattices (Figure 2.6). A centrosymmetric (simple Bravais) lattice is one that has pairs of bonds in opposite directions around each atom. The CB rule ensures equilibrium for such a structure for arbitrary, imposed, homogeneous deformations [17, 85]. The graphene lattice that forms an SWNT, however, is not centrosymmetric, but consists of two different sub-lattices (a Bravais multi-lattice), each of which is centrosymmetric (Figure 2.6). The standard crystal elasticity treatment of multi-lattices is to assume that the homogeneous deformation affects each of the simple lattices [17, 85].

Additional kinematic variables describing the relative shifts of the simple lattices must be introduced to properly describe the configurations of uniformly strained multi-lattices. An in-plane shift vector, $\boldsymbol{\eta}$, becomes necessary in such a case to relate an atom pair when each of the atoms in the pair lies on different sub-lattices [2, 3, 12, 13, 44, 52, 79, 85, 101]. This leads to a modification in Equation 2.18 as follows:

$$\mathbf{a}(i,j) = \mathcal{M}^{-1}\mathbf{F}(\mathbf{X})\mathcal{M}\left[\mathbf{A}(i,j) + \boldsymbol{\eta}\right] \quad , \tag{2.19}$$

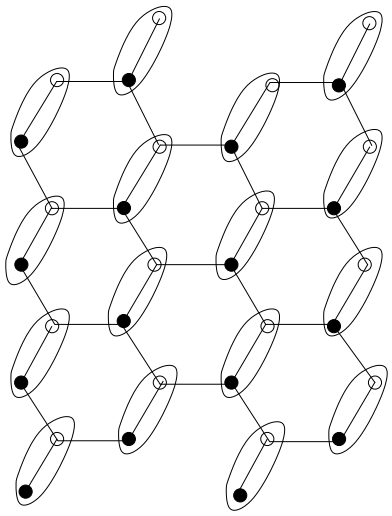

Figure 2.6: The graphene lattice viewed as a Bravais multi-lattice – either a simple Bravais hexagonal lattice with two basis atoms (a pair of filled and empty circles), or two woven simple Bravais hexagonal lattices (the collection of filled and empty circles separately) shifted relative to each other.

when atoms i and j belong to different sub-lattices, while $\boldsymbol{\eta} = \mathbf{0}$ otherwise. It is noted, from above, that a deformed bond length, a, in general, is a function of $\mathbf{E}$ and $\boldsymbol{\eta}$. This is shown explicitly through analytic expressions provided in Section 4.2. In practice, the shift vector can be accounted for by providing additional degrees of freedom to the coordinates of the representative atom in the undeformed configuration, and finding these additional displacements by minimizing the binding energy of the representative atom for each imposed deformation, $\mathbf{F}$. In the present two-dimensional membrane continuum, $\boldsymbol{\eta}$ has only in-plane components (specifically, with respect to a cylindrical basis, the only allowed components are η_Θ and η_Z, with the radial component constrained to be zero). Since the internal relaxation due to the shift vectors is applied to the reference configuration, material frame indifference of the deformed bond lengths to rigid body rotations is automatically guaranteed. In fact, this guarantees material frame indifference even when an exact deformation map (Equation 2.16)

is used to obtain the deformed bond lengths instead of the CB rule (viewed as a truncated Taylor series). This is made clear in the context of a specific deformation map in Chapter 3. This implementation approach also ensures that the internal relaxation can be easily incorporated in the analytic expressions for the deformed bond vectors derived subsequently in Sections 3.3 and 4.2.2. In all of the above equations involving **F** or **E**, it is noted that when the deformation is inhomogeneous, these tensors need to be evaluated at a specific point on each bond in order to apply the above equations and obtain the deformed bond lengths, as described in Section 2.4.2.

2.5 Continuum strain energy density expressed in terms of interatomic potentials

The deformed bond lengths obtained from Equation 2.19 are used along with Equation 2.1 to define a hyperelastic, continuum strain energy density function, W, for the two-dimensional membrane SWNT model.

A representative unit cell of the graphene lattice, indicated in Figure 2.7, containing two carbon atoms [20], is considered. In view of the two-atom basis for graphene, its entire structure can be generated by replicating the parallelogram in Figure 2.7 without gaps or overlaps. This leads to the following definition of W [2, 3, 12, 13, 44, 52, 101]:

$$W(\mathbf{E}, \boldsymbol{\eta}(\mathbf{E})) \equiv \widehat{W}(\mathbf{E}) = \frac{\sum_{cell} V(a(i,j))}{\Omega_{cell}} \quad , \tag{2.20}$$

where the bond energies are summed over the domain of the representative unit

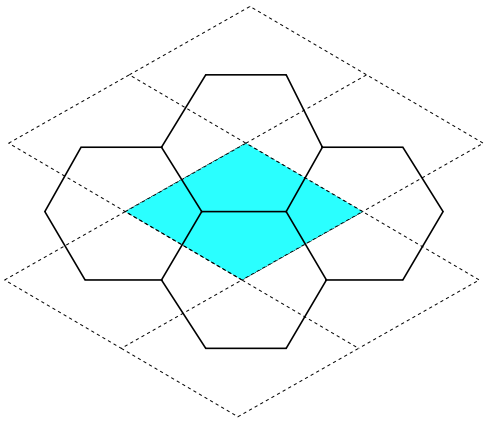

Figure 2.7: The shaded parallelogram shown above is the unit cell in a graphene sheet.

cell of area Ω_{cell} in the cylindrical configuration. This area is assumed to be preserved while rolling up a planar graphene sheet, and hence can be computed from the planar configuration shown in Figure 2.7. It is noted here that W is frame-indifferent to rigid body rotations since it depends only on the deformed bond lengths which have been shown to be frame-indifferent in Section 2.4.4. This hyperelastic strain energy density also depends on the undeformed crystal structure and inherits its symmetries. Further, when the deformation is inhomogeneous, $\mathbf{E}$ varies in space. However, the above definition of W implies that as long as the deformed bond lengths are obtained by evaluating $\mathbf{E}$ at a specific point on each bond, W is uniform over the unit cell (i.e., it does not contain an explicit spatial variation within the unit cell). This leads to an approximation of the total energy in the domain as the sum of unit cell energies.

The second Piola-Kirchhoff stress tensor, $\mathbf{T}$, is obtained as the derivative of the strain energy density function, $\widehat{W}$, with respect to the Green-Lagrangian strain, $\mathbf{E}$, as follows:

$$\mathbf{T}(\mathbf{E}) = \frac{d\widehat{W}}{d\mathbf{E}} = \left.\frac{\partial W}{\partial \mathbf{E}}\right|_{\boldsymbol{\eta}} + \left.\frac{\partial W}{\partial \boldsymbol{\eta}}\right|_{\boldsymbol{E}} \cdot \frac{d\boldsymbol{\eta}}{d\mathbf{E}} = \left.\frac{\partial W}{\partial \mathbf{E}}\right|_{\boldsymbol{\eta}} \quad , \tag{2.21}$$

since the relaxed shift vector, $\boldsymbol{\eta} = \hat{\boldsymbol{\eta}}$, is chosen such that (referring to earlier discussion on the shift vector) $\left.\frac{\partial W}{\partial \boldsymbol{\eta}}\right|_{\boldsymbol{E}} = \mathbf{0}$. The fourth-rank Lagrangian elasticity tensor, $\mathbb{C}$, at the onset of deformation has the form [12, 14, 101]

$$\mathbb{C} = \left.\frac{d\mathbf{T}(\mathbf{E})}{d\mathbf{E}}\right|_{\mathbf{E}=\mathbf{0}} = \left[\frac{\partial^2 W}{\partial \mathbf{E}\partial \mathbf{E}} - \frac{\partial^2 W}{\partial \mathbf{E}\partial \boldsymbol{\eta}} \cdot \left[\frac{\partial^2 W}{\partial \boldsymbol{\eta}\partial \boldsymbol{\eta}}\right]^{-1} \cdot \frac{\partial^2 W}{\partial \boldsymbol{\eta}\partial \mathbf{E}}\right]\Bigg|_{\mathbf{E}=\mathbf{0}} \quad , \tag{2.22}$$

where the reference configuration is assumed to be stress-free, i.e., $\mathbf{T}(\mathbf{0}) = \mathbf{0}$. Further, as noted in [2, 3, 12, 101], the above definition of the strain energy density (Equation 2.20) leads to stresses with units of force per unit length because W is defined as the strain energy per unit area (rather than per unit volume) of the continuum. A consequence of this choice is that the stress and modulus tensors, $\mathbf{T}(\mathbf{E})$ and $\mathbb{C}$, defined in Equations 3.4–2.22, are actually the (conventional) stress × wall thickness and (conventional) modulus × wall thickness, respectively. This issue is further addressed while interpreting numerical results in Section 4.4.

In the following chapter, the two-dimensional, quasicontinuum, hyperelastic membrane SWNT model is implemented to study the kinematic coupling between extension and twist in SWNTs.

CHAPTER 3

KINEMATIC COUPLING BETWEEN EXTENSION AND TWIST USING THE QUASICONTINUUM MEMBRANE MODEL

3.1 Introduction

This chapter presents a study of coupled extension and twist deformations in SWNTs. Aspects of the CB rule (Section 2.4) related to spatial inhomogeneity of the deformation gradient, **F**, at the atomic scale, are investigated in the context of a specific class of extension-twist deformation problems. Analytic expressions are derived for the deformed bond lengths using the standard CB rule, as well as its modified versions (Section 2.4). The extension-twist deformation problem is chosen because of its simplicity in being able to describe a deformation map, which makes it possible to compare the modified CB rules against the exact solution (i.e., the exact analytic expression for the deformed bond vectors) arising directly from the deformation map (Section 2.4.2). This approach provides insights into the CB rule and its possible modifications for use in more complicated deformations where an explicit deformation map is not available. Specifically, it is demonstrated that in the case of inhomogeneous deformations at the atomic scale for which the CB rule is only approximate (as mentioned in Section 2.4.2), the mean value theorem in calculus [37] can be used as a guide to modify the CB rule (Equation 2.14) to account for the spatial inhomogeneity of **F** at the atomic scale. The deformed bond lengths are subsequently used to formulate a hyperelastic continuum strain energy density function based on interatomic potentials (as described in Section 2.5).

The deformation map (and hence **F**, the bond vectors, and the continuum

strain energy density function) contains certain parameters, some of which are imposed and others determined as a result of energy minimization in a standard variational formulation. Numerical results for kinematic coupling and binding energy per atom are presented in the case of imposed extension and twist deformations on representative chiral, zigzag, and armchair SWNTs using the CB rule and its modifications, as well as the exact solution based directly on the deformation map. Although the ideas presented in this chapter are investigated only in the context of SWNTs, they are also applicable to other lattices.

This chapter is organized as follows. A generalized deformation map that models coupled extension and twist of a thin-walled, circular cylinder is presented in Section 3.2, and an analysis of the equivalence between the strong and weak forms of static equilibrium for this proposed deformation map follows in Sections 3.2.1 and 3.2.2. The deformation gradient ($\mathbf{F}$) derived from this map happens to be inhomogeneous, in general. Hence, in the context of this coupled extension-twist deformation, possible modifications to the CB rule are presented in Section 3.3 (in conjunction with the previous discussions in Section 2.4.1) to deal with the inhomogeneity in $\mathbf{F}$ using analytic expressions for the deformed bond lengths derived from different approaches. Finally, numerical results are presented in Section 3.4 to illustrate the suggested modifications in the context of two different deformation problems. In the first problem, discussed in Section 3.4.1, the coupling between extension and twist deformations imposed on SWNTs is studied, while in the second, discussed in Section 3.4.2, the variation of the binding energy per atom with imposed extension on SWNTs, is studied. A discussion of the results and some concluding remarks in Section 3.5 complete the chapter.

3.2 Generalized extension and twist of a thin-walled circular cylinder

A generalized extension-twist deformation map is presented in Box 2 in terms of cylindrical polar coordinates, and illustrated in Figure 3.1.

$$r = \gamma R$$
$$\theta = \Theta + f(Z;k)$$
$$z = (1+\epsilon)Z$$

Box 2: The generalized extension-twist deformation map.

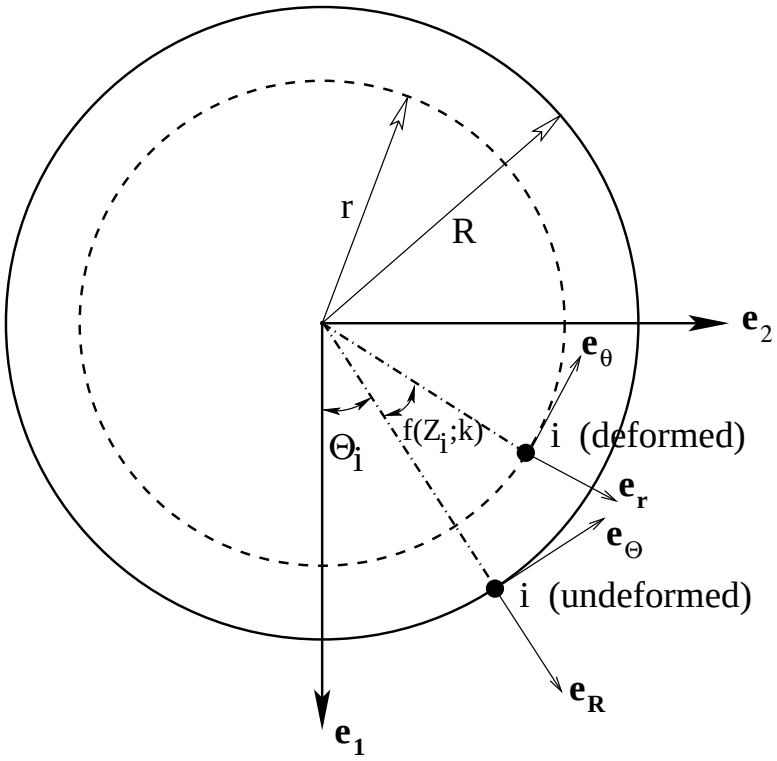

Figure 3.1: Undeformed and deformed states corresponding to the generalized extension-twist deformation map in Box 2.

In Box 2, r and R are the deformed and undeformed radii of cross-section of a thin-walled, circular cylinder respectively, γ is a parameter that captures

the change in cross-sectional radius, θ and Θ are, respectively, the deformed and undeformed polar angles on the cylindrical cross-section, z and Z are the deformed and undeformed axial coordinates respectively, ϵ is the axial strain, and f, parameterized by k, is a sufficiently smooth and differentiable function of Z. For example, in the special case when $f(Z;k) \equiv kZ$, k is the angle of twist per unit undeformed length of the cylinder. It is noted that the deformation map in Box 2 is, in general, inhomogeneous owing to the presence of f. As is evident, this deformation maps an undeformed cylinder onto a deformed cylinder (Figure 3.1).

The present section is organized as follows. First, the local (strong) form of the equilibrium equations is presented in Section 3.2.1. Next, the variational (weak) form of equilibrium based on energy minimization, is presented in Section 3.2.2. Both formulations are consistently Lagrangian, i.e., all equations are expressed in terms of the undeformed configuration. It is assumed that there are no body forces (i.e., volumetrically distributed forces) under consideration, and the deformation in Box 2 is assumed to be achieved by the application of surface tractions alone. It is useful in this context to refer to Ericksen's theorem, a proof of which can be found in [62]. The theorem states that homogeneous deformations are the only deformations (of an unconstrained, isotropic, elastic solid) which can be achieved by the application of surface tractions alone, independent of the form of the strain energy density function. In the present work, however, the equivalent continuum material is not assumed to be isotropic and, therefore, Ericksen's theorem does not apply. Finally, the correspondence between the two formulations is investigated. Contrary to the formulation of a standard boundary-value-problem, the correspondence between the strong and weak forms is not trivial in the present case because the deformations have been

prescribed and not obtained as solutions to the field equations with boundary conditions. The analysis also enables the establishment of conditions on f for equivalence of the two formulations.

3.2.1 Local form of the static equilibrium equations

It is convenient to perform the present analysis by employing two sets of cylindrical basis vectors. A referential set of basis vectors, $\{\mathbf{e}_R, \mathbf{e}_\Theta, \mathbf{e}_Z\}$, and a deformed set of basis vectors, $\{\mathbf{e}_r, \mathbf{e}_\theta, \mathbf{e}_z\}$, are introduced. The two sets of basis vectors are related by an orthogonal transformation given as follows (Figure 3.1):

$$\begin{aligned}
\mathbf{e}_r &= \mathbf{e}_R \cos(f) + \mathbf{e}_\Theta \sin(f) \\
\mathbf{e}_\theta &= -\mathbf{e}_R \sin(f) + \mathbf{e}_\Theta \cos(f) \\
\mathbf{e}_z &= \mathbf{e}_Z \quad .
\end{aligned} \tag{3.1}$$

In terms of these basis vectors, the deformation gradient, $\mathbf{F}$, can be evaluated to be

$$\mathbf{F} = \gamma(\mathbf{e}_r \otimes \mathbf{e}_R + \mathbf{e}_\theta \otimes \mathbf{e}_\Theta) + \gamma R f' \mathbf{e}_\theta \otimes \mathbf{e}_Z + (1+\epsilon)\mathbf{e}_z \otimes \mathbf{e}_Z \quad , \tag{3.2}$$

where f' denotes the derivative of f with respect to Z. The corresponding expression for the Green-Lagrangian strain tensor, $\mathbf{E} = \frac{1}{2}(\mathbf{F}^T\mathbf{F} - \mathbf{I})$ (with $\mathbf{I}$ being the second-rank identity tensor), is

$$\mathbf{E} = \frac{1}{2}\left(\gamma^2 - 1\right)(\mathbf{e}_R \otimes \mathbf{e}_R + \mathbf{e}_\Theta \otimes \mathbf{e}_\Theta) + \frac{1}{2}\gamma^2 R f'(\mathbf{e}_\Theta \otimes \mathbf{e}_Z + \mathbf{e}_Z \otimes \mathbf{e}_\Theta) + \frac{1}{2}(\gamma^2 R^2 f'^2 + 2\epsilon + \epsilon^2)\mathbf{e}_Z \otimes \mathbf{e}_Z \quad . \tag{3.3}$$

The second Piola-Kirchhoff stress tensor, **T**, is obtained as the derivative of the strain energy density function, $\hat{W}$, with respect to **E** as follows:

$$\mathbf{T} = \frac{d\hat{W}}{d\mathbf{E}} = \left.\frac{\partial W}{\partial \mathbf{E}}\right|_{\hat{\boldsymbol{\eta}}} + \left.\frac{\partial W}{\partial \boldsymbol{\eta}}\right|_{\hat{\boldsymbol{\eta}}} \cdot \left.\frac{d\boldsymbol{\eta}}{d\mathbf{E}}\right|_{\hat{\boldsymbol{\eta}}} = \left.\frac{\partial W}{\partial \mathbf{E}}\right|_{\hat{\boldsymbol{\eta}}} \quad , \tag{3.4}$$

since the relaxed shift vector $\hat{\boldsymbol{\eta}}$ is chosen such that (Section 2.4.4)

$$\left.\frac{\partial W}{\partial \boldsymbol{\eta}}\right|_{\hat{\boldsymbol{\eta}}} = \mathbf{0} \quad . \tag{3.5}$$

The first Piola-Kirchhoff stress tensor, **S**, is obtained as

$$\mathbf{S} = \mathbf{F} \cdot \mathbf{T} \quad . \tag{3.6}$$

Next, the referential version of the equilibrium equations without body forces is presented in cylindrical polar coordinates. First, it is assumed that the surfaces of the thin-walled cylinder are traction-free, i.e.,

$$\mathbf{S} \cdot \mathbf{e}_R = \mathbf{0} \tag{3.7}$$

on the outer and inner lateral surfaces. However, since the SWNT is a single-atomic layer thick with a vanishingly small wall thickness, Equation 3.7 is as-

sumed to be true through the 'thickness' as well. The equilibrium equations, in conjunction with Equation 3.7, along $\{\mathbf{e}_R, \mathbf{e}_\Theta, \mathbf{e}_Z\}$ respectively, are given as [28]

$$\begin{aligned}
&\frac{1}{R}\frac{\partial S_{R\Theta}}{\partial \Theta} - \frac{1}{R}S_{\Theta\Theta} + \frac{\partial S_{RZ}}{\partial Z} = 0 \\
&\frac{1}{R}S_{R\Theta} + \frac{1}{R}\frac{\partial S_{\Theta\Theta}}{\partial \Theta} + \frac{\partial S_{\Theta Z}}{\partial Z} = 0 \\
&\frac{1}{R}\frac{\partial S_{Z\Theta}}{\partial \Theta} + \frac{\partial S_{ZZ}}{\partial Z} = 0 \quad .
\end{aligned} \tag{3.8}$$

Using Equations 3.1 and Equation 3.2 in Equation 3.6, and projecting Equations 3.8 along $\mathbf{e}_r$ gives

$$T_{\Theta\Theta} + 2Rf'T_{\Theta Z} + f'^2R^2T_{ZZ} = 0 \quad . \tag{3.9}$$

Similarly, projecting Equations 3.8 along $\mathbf{e}_\theta$ gives

$$\frac{\partial T_{\Theta\Theta}}{\partial \Theta} + f'R\frac{\partial T_{\Theta Z}}{\partial \Theta} + R\frac{\partial T_{\Theta Z}}{\partial Z} + f''R^2T_{ZZ} + f'R^2\frac{\partial T_{ZZ}}{\partial Z} = 0 \quad . \tag{3.10}$$

Finally, projecting Equations 3.8 along $\mathbf{e}_z$ gives

$$\frac{\partial T_{\Theta Z}}{\partial \Theta} + R\frac{\partial T_{ZZ}}{\partial Z} = 0 \quad . \tag{3.11}$$

Further, the stress measures in the present problem, can be assumed to be independent of the polar coordinate, Θ. Thus, Equations 3.10 and 3.11 can be further reduced to

$$\frac{\partial}{\partial Z}[T_{\Theta Z} + f' R T_{ZZ}] = 0 \quad , \tag{3.12}$$

and

$$\frac{\partial T_{ZZ}}{\partial Z} = 0 \quad , \tag{3.13}$$

respectively. Equations 3.12 and 3.13, along with Equation 3.9, form the final set of static equilibrium equations in local form for the present problem.

3.2.2 Weak form of the static equilibrium equations: Principle of stationary potential energy

The total potential energy of any given deformation map, Ψ, can be written as

$$\Pi(\Psi) = \Pi_{int} - \Pi_{ext} + \Pi_{nb} \quad , \tag{3.14}$$

where Π_{int} is the internal (strain) energy of the system, given as

$$\Pi_{int} = \int_{\Omega_0} \hat{W}(\mathbf{E}(\Psi)) d\Omega_0 \quad , \tag{3.15}$$

where Ω_0 is the undeformed domain, Π_{ext} contains the body forces, and Π_{nb} contains the non-bonded interactions. As mentioned earlier, the presence of body forces is not considered in the present problem. Non-bonded interactions [2], which account for forces acting between non-bonded pairs of atoms, are

also excluded in the present problem. According to the principle of stationary potential energy, the equilibrium configurations, Φ, of the system, are stationary points of the potential energy functional. Therefore, it follows that

$$\delta\Pi(\Phi) \equiv \frac{\partial}{\partial\beta}\Pi(\Phi + \beta\Upsilon)\Big|_{\beta=0} = 0 \quad , \tag{3.16}$$

for all admissible variations, Υ, that satisfy the specified displacement boundary conditions. In connection with the deformation map prescribed in Box 2 and Equation 3.3, it is useful, at this stage, to consider $\hat{W}$ as a function of γ, k and ϵ, i.e.,

$$\hat{W}(\mathbf{E}) \equiv \tilde{W}(\gamma, k, \epsilon) \quad . \tag{3.17}$$

The following sub-sections investigate the possibility of satisfying the local equilibrium equations (Equations 3.12, 3.13, and 3.9) by minimizing $\tilde{W}$ with respect to its arguments. Here, the following distinction is made. If ϵ is imposed, and γ and k determined by minimization, the problem is called an imposed extension problem. On the other hand, if k is prescribed, and γ and ϵ are obtained through minimization, the problem is called an imposed twist problem.

Imposed extension problem

In the present problem, ϵ is imposed, and γ and k are obtained through minimization of $\tilde{W}$. Accordingly, it is required that $\frac{\partial\tilde{W}}{\partial\gamma} = 0$. Using this condition, along with Equation 3.3 and 3.4, gives

$$T_{\Theta\Theta} + 2Rf'T_{\Theta Z} + f'^2R^2T_{ZZ} = 0 \quad , \tag{3.18}$$

which is precisely Equation 3.9 obtained from the local form of static equilibrium. In addition, it is also required that $\frac{\partial \tilde{W}}{\partial k} = 0$, which leads to

$$\frac{\partial f'}{\partial k}[T_{\Theta Z} + f'RT_{ZZ}] = 0 \quad . \tag{3.19}$$

Assuming $\frac{\partial f'}{\partial k} \neq 0$, it follows that

$$T_{\Theta Z} + f'RT_{ZZ} = 0 \quad , \tag{3.20}$$

which satisfies Equation 3.12. With regard to satisfying Equation 3.13, the following relation between the second Piola-Kirchhoff stress and the Cauchy stress is noted:

$$\mathbf{T} = J\mathbf{F}^{-1} \cdot \sigma \cdot \mathbf{F}^{-T} \quad , \tag{3.21}$$

where $J = det(\mathbf{F})$, from which it follows that

$$T_{ZZ} = \frac{\gamma^2}{(1+\epsilon)}\sigma_{zz} \quad . \tag{3.22}$$

Since σ_{zz} is constant under imposed extension, Equation 3.22 implies that Equation 3.13 is also satisfied. Hence, the imposed extension minimization problem satisfies the required equilibrium equations (without body forces) for arbitrary $f(Z;k)$ satisfying $\frac{\partial f'}{\partial k} \neq 0$.

Imposed twist problem

In the present problem, k is imposed, and γ and ϵ are obtained through minimization of $\tilde{W}$. As in the previous sub-section, it is first noted that $\frac{\partial \tilde{W}}{\partial \gamma} = 0$, which gives Equation 3.18, and hence satisfies Equation 3.9. In addition, it is also required that $\frac{\partial \tilde{W}}{\partial \epsilon} = 0$, leading to

$$(1 + \epsilon)T_{ZZ} = 0 \Rightarrow T_{ZZ} = 0 \quad , \tag{3.23}$$

which satisfies Equation 3.13. Equation 3.23, along with Equation 3.22, also implies

$$\sigma_{zz} = 0 \quad . \tag{3.24}$$

Using Equation 3.23 in Equation 3.12, it is required that

$$T_{\Theta Z} = constant \quad , \tag{3.25}$$

in order to satisfy the full set of equilibrium equations. Using Equation 3.21, combined with the result from Equation 3.24, it follows that

$$T_{\Theta Z} = \gamma \sigma_{\theta z} \quad . \tag{3.26}$$

Now, a necessary condition is generated, to satisfy Equation 3.25, by considering a small-strain theory. From Saint Venant's theory of torsion [28], and from using Box 2, it follows that

$$\sigma_{\theta z} = G\gamma R f' \quad , \tag{3.27}$$

where G is the twist modulus of the material in a small-strain theory. Finally, from using Equation 3.27 and Equation 3.26 in Equation 3.25, it follows that

$$f' = constant \quad , \tag{3.28}$$

as the necessary condition to satisfy static equilibrium (without body forces) in the imposed twist problem.

In summary, it is noted that the imposed extension problem satisfies equilibrium for arbitrary f (satisfying $\frac{\partial f'}{\partial k} \neq 0$), while the imposed twist problem requires the condition $f' = constant$.

3.3 Bond vector deformations

In the present section, analytic expressions are obtained for the deformed bond vectors between any two atoms denoted by i and j using the CB rule and its modifications (Section 2.4). The deformed bond vectors, obtained directly using the deformation map (Box 2), serve as a basis for evaluating the accuracy of these deformation rules. Subscripts i and j, in the following, are labels used to denote the corresponding atoms.

3.3.1 Modified Cauchy-Born rule in the generalized extension-twist problem

In the following discussion, the Euclidean bond vectors before and after deformation are denoted by **A** and **a** respectively. The projected geodesic vector lying on a tangent plane to the undeformed SWNT is denoted by $\tilde{\mathbf{A}}$, and the deformed geodesic vector (lying on a tangent plane to the deformed SWNT) obtained from directly using the deformation map (Box 2) is denoted by $\tilde{\mathbf{a}}$, while the deformed geodesic vector obtained from the exponential CB rule (Section 2.4.3) is denoted by $\hat{\mathbf{a}}$.

As discussed in Section 2.4.3, the exponential CB rule effectively replaces **F** in Equation 2.14 by a composition of three operations – first 'unwrapping' the geodesic connecting the atoms onto the tangent plane at **X** (this operation is denoted here by $\mathcal{M}$), then applying **F** to this geodesic vector to obtain the deformed geodesic vector lying on the deformed tangent plane, and finally 'wrapping' the deformed geodesic vector back onto the deformed surface (this operation is denoted by $\mathcal{M}^{-1}$) to obtain the Euclidean bond lengths. This process is graphically shown in Figure 2.5, and mathematically expressed in Equation 2.18.

In the context of the extension-twist deformation problem (Box 2), the undeformed geodesic vector directed from atom i to atom j, when 'unwrapped' onto the undeformed tangent plane at a referential material point, is given (in cylindrical polar coordinates) by

$$\begin{aligned}\tilde{\mathbf{A}} &= \mathcal{M}\mathbf{A} \\ &= R(\Theta_j - \Theta_i)\mathbf{e}_\Theta + (Z_j - Z_i)\mathbf{e}_Z \quad .\end{aligned} \tag{3.29}$$

Next, the deformed geodesic vector, obtained directly by using the deformation map given in Box 2 (and hence the infinite Taylor series denoted in Equation 2.16), can be written as

$$\begin{aligned}\tilde{\mathbf{a}} &= \mathcal{F}(\tilde{\mathbf{A}}) \\ &= \gamma R(\theta_j - \theta_i)\mathbf{e}_\theta + (z_j - z_i)\mathbf{e}_z \\ &= \gamma R[(\Theta_j - \Theta_i) + \{f(Z_j) - f(Z_i)\}]\mathbf{e}_\theta + (1+\epsilon)(Z_j - Z_i)\mathbf{e}_z \quad .\end{aligned} \tag{3.30}$$

It is noted that use of the direct deformation map, as given by Equation 2.16, leads to a higher gradient theory where $W \equiv \hat{W}(\mathbf{F}, \boldsymbol{\nabla}\mathbf{F}, \boldsymbol{\nabla}\boldsymbol{\nabla}\mathbf{F}, \ldots)$. Though the definition of stress measures (and hence the use of the local formulation) is not as straightforward as in the case when $W \equiv \hat{W}(\mathbf{F})$, the weak formulation (Section 3.2.2) can still be used directly to perform deformation simulations. Also, comments related to material frame indifference and symmetry made in Section 2.5, apply to the use of the direct map as well.

Now, the deformed geodesic vector is obtained by using the exponential CB rule (using Equations 4.4 and 3.2 in Equation 2.18). However, since $\mathbf{F}$, in general, varies with space in the present analysis, it is evaluated at an intermediate point

$\mathbf{X}_\alpha$ lying on the undeformed geodesic vector directed from atom i to atom j, and is given by

$$\hat{\mathbf{a}} = \mathbf{F}(\mathbf{X}_\alpha) \cdot \tilde{\mathbf{A}} = \gamma R[(\Theta_j - \Theta_i) + (Z_j - Z_i) f'(Z_\alpha)]\mathbf{e}_\theta + (1 + \epsilon)(Z_j - Z_i)\mathbf{e}_z \quad , \tag{3.31}$$

where Z_α is the undeformed axial coordinate of this intermediate point. Comparing Equations 3.31 and 3.30 enables the determination of the point, $\mathbf{X}_\alpha$, at which the exponential CB rule (Equation 2.18) gives the exact solution as obtained from Equation 2.16. This is obtained as the solution of

$$f'(Z_\alpha) = \frac{f(Z_j) - f(Z_i)}{Z_j - Z_i} \quad . \tag{3.32}$$

It is noted that, since f is assumed to be a differentiable function between Z_i and Z_j, the mean value theorem states that Equation 3.32 can always be solved to obtain Z_α [37]. It is useful, at this point, to refer to Section 2.4.2 (Equation 2.17) in which a discussion on applying the CB rule for general, inhomogeneous deformations is provided in the context of bulk crystals. As an illustration of the application of Equation 3.32, it is noted that when $f(Z; k) \equiv kZ$, Equation 3.32 is identically satisfied for all choices of $\mathbf{X}_\alpha$, and the exponential CB rule yields the exact deformed bond vectors (and bond lengths) independent of the point at which $\mathbf{F}$ (in Equation 2.14) is evaluated. However, if $f(Z; k) \equiv kZ^2$, Equation 3.32 gives the best location to apply the CB rule to be $Z_\alpha = \frac{1}{2}(Z_i + Z_j)$, which corresponds to the mid point of the 'unwrapped' undeformed bond vector. For all other choices of Z_α, the result from the CB rule is, clearly, only approximate as pointed out in Section 2.4.2.

The actual length of the deformed bond vector, i.e., the Euclidean distance between atoms i and j in the deformed configuration (Figure 2.5), is obtained by 'wrapping' the deformed geodesic (Equation 3.31) back onto the deformed cylinder, and is given by

$$\begin{aligned} a(i,j) &= |\mathbf{a}| \\ &= |\mathcal{M}^{-1}\hat{\mathbf{a}}| \\ &= \sqrt{[4\gamma^2 R^2 \sin^2\{\frac{1}{2}((\Theta_j - \Theta_i) + (Z_j - Z_i) f'(Z_\alpha))\} + (1+\epsilon)^2 (Z_j - Z_i)^2]} \quad . \end{aligned} \tag{3.33}$$

As mentioned before, for a choice of the 'unwrap' point ($\mathbf{X}_\alpha$) given by Equation 3.32, this expression coincides with the exact expression obtained directly from using the deformation map (Box 2). For all other choices of α, this expression is, in general, only approximate. In principle, such an approximation can be improved by successively adding higher order terms of the Taylor series denoted in Equation 2.16.

Equation 4.5 is used to perform deformation simulations on SWNTs in Section 3.4. In the following sub-section, Section 3.3.2, some general observations are presented on the nature of the deformation gradient, $\mathbf{F}$, pertaining to the CB rule, which generalize some of the conclusions drawn in the present section.

3.3.2 Observations on the deformation gradient related to the Cauchy-Born rule

A setting similar to the one in Section 3.2.1 is considered[1]. A set of basis vectors, $\{\mathbf{e}_I\}$ $(I = 1, 2, 3)$, are defined to describe the undeformed configuration, while a set of basis vectors, $\{\mathbf{e}_i\}$, $(i = 1, 2, 3)$ are defined to describe the deformed configuration such that these sets of basis vectors are related by an orthogonal transformation, $\mathbf{Q}$, similar to Equations 3.1, i.e.,

$$\mathbf{e}_i = Q_{iI}\mathbf{e}_I \quad . \tag{3.34}$$

For convenience, the undeformed basis vectors are also expressed in terms of a fixed Cartesian basis $\{\mathbf{e}_\alpha\}$ $(\alpha = 1, 2, 3)$ as follows:

$$\mathbf{e}_I = R_{I\alpha}\mathbf{e}_\alpha \quad , \tag{3.35}$$

and it is further noted that $Q_{iI}Q_{jI} = \delta_{ij}$, $R_{I\alpha}R_{J\alpha} = \delta_{IJ}$, where δ_{ij} is the Kronecker delta function defined by

$$\delta_{ij} = \begin{cases} 1, & i = j \\ 0, & i \neq j \end{cases} \quad . \tag{3.36}$$

It is also to be noted that the basis vectors, $\{\mathbf{e}_I\}$, $\{\mathbf{e}_i\}$, and the orthogonal transformations, $\mathbf{Q}$ and $\mathbf{R}$, vary in space in general (as also seen from Equation

[1]In the present section (Section 3.3.2), lower as well as upper case Latin and Greek indices range from 1 to 3, and indices repeated in the same term are summed over their respective ranges unless explicitly stated otherwise.

3.1 for the cylindrical basis vectors). In terms of these basis vectors, the deformation gradient, **F**, and the undeformed geodesic vector can be expressed (in forms generalizing Equations 3.2 and 4.4 respectively) as

$$\mathbf{F} = F_{iJ}\mathbf{e}_i \otimes \mathbf{e}_J \quad , \tag{3.37}$$

and

$$\tilde{\mathbf{A}} = \tilde{A}_I \mathbf{e}_I \quad . \tag{3.38}$$

It is noted that the components $\tilde{A}_I$ are constants (cf. with Equation 4.4), while the components F_{iJ} may either be constants or vary in space depending on the specific deformation map. In the present deformation considered (Box 2), this depends on the choice of $f(Z;k)$. From Equation 3.2, it is evident that F_{iJ} would be constant in the present case if $f(Z;k)$ is constant (pure extension problem) or linear (kZ), while it would vary with space otherwise. Using the exponential CB rule (Section 2.4.3), the deformed geodesic vector is expressed (as a generalized version of Equation 3.31) in terms of the fixed Cartesian basis as follows:

$$\hat{\mathbf{a}} = F_{iJ}\tilde{A}_J Q_{iI} R_{I\alpha}\mathbf{e}_\alpha \quad . \tag{3.39}$$

In Equation 3.39, it is noted that the components of $\hat{\mathbf{a}}$ are inhomogeneous, in general, owing to the presence of **Q** and **R**, irrespective of whether the components F_{iJ} vary with space. However, the magnitude of $\hat{\mathbf{a}}$ can be found (using the orthogonality of **Q** and **R**) to be

$$\hat{a} = \sqrt{F_{iJ}F_{iK}\tilde{A}_J\tilde{A}_K} \quad . \tag{3.40}$$

This shows that the deformed geodesic length, obtained from the exponential CB rule, would be independent of the spatial variation in **F** if its components F_{iJ} are constants. For the deformations considered in the present work, this also means that the deformed bond lengths would be independent of the spatial variation in **F** if its components are constants, which is in agreement with the conclusions drawn from Section 4.2.2. Using a similar approach, one can observe that similar conclusions hold even if **F** is expressed in a fully referential basis ($\mathbf{F} = F_{IJ}\mathbf{e}_I \otimes \mathbf{e}_J$). In this case, the magnitude of the deformed geodesic vector would be equal to $\sqrt{F_{IJ}F_{IK}\tilde{A}_J\tilde{A}_K}$, and the deformed bond lengths would be independent of the spatial variation in **F** if its components F_{IJ} are constants. Finally, as mentioned in Section 2.4.2, it is observed that the standard CB rule (with no modification using the exponential map) gives the exact deformed bond vector if the components of **F** are spatially constant with respect to the fixed Cartesian basis (as would occur, for example, in the case of simple tension, or uniform radial expansion and contraction of a circular cylinder) because the gradient-based terms in Equation 2.16 would automatically vanish in such a case.

3.4 Deformation simulations

In the present section, the results of SWNT deformation analyses are discussed corresponding to specific choices of $f(Z;k)$ in Box 2.

3.4.1 $f(Z;k) \equiv kZ$: Imposed twist and extension problems

Some of the published work that deals with SWNTs under imposed twist and extension (Section 3.2.2) [12, 13, 44, 52, 101] involves a deformation map as given in Box 2, with $f(Z;k) \equiv kZ$. As shown in Section 3.2.2 (Equation 3.28), this is the only choice for f which can be maintained in equilibrium without body forces for an imposed twist problem. In [12], deformation analysis is performed using the standard CB rule (Equation 2.14) without constraining the atoms to lie on a single surface. It is shown that the bond lengths (and the kinematic coupling plots) obtained from the standard CB rule coincide with those obtained from the direct deformation map only for small values of k. This differs from the present approach in which the exponential CB rule is used with all the atoms lying on a single surface (the radial component of $\boldsymbol{\eta}$, η_R, is constrained to be zero in the present work – Equation 2.19). In the present case, since f' is a constant, Equation 3.32 implies that the deformed bond vector (and hence the kinematic coupling results – induced extension obtained under imposed twist) obtained from the exponential CB rule is independent of the point at which $\mathbf{F}$ is evaluated. Also, Equation 3.32 implies that this deformed bond vector is exact (Equations 3.30 and 3.31 coincide). This has, however, been shown to not be true if the standard CB rule is used [12], and hence the exponential map modification becomes essential in this case to obtain the exact bond lengths.

Kinematic coupling results are presented (using the exponential CB rule and $\eta_R = 0$) for imposed twist in Figures 3.2(a) and 3.2(b), and imposed extension in Figures 3.2(c) and 3.2(d), for representative chiral $(9, 6)$, zigzag $(10, 0)$, and armchair $(5, 5)$ SWNTs corresponding to parameter set 1 (Table 2.2) of the Tersoff-Brenner interatomic potential (Section 2.2). The results from using parameter set

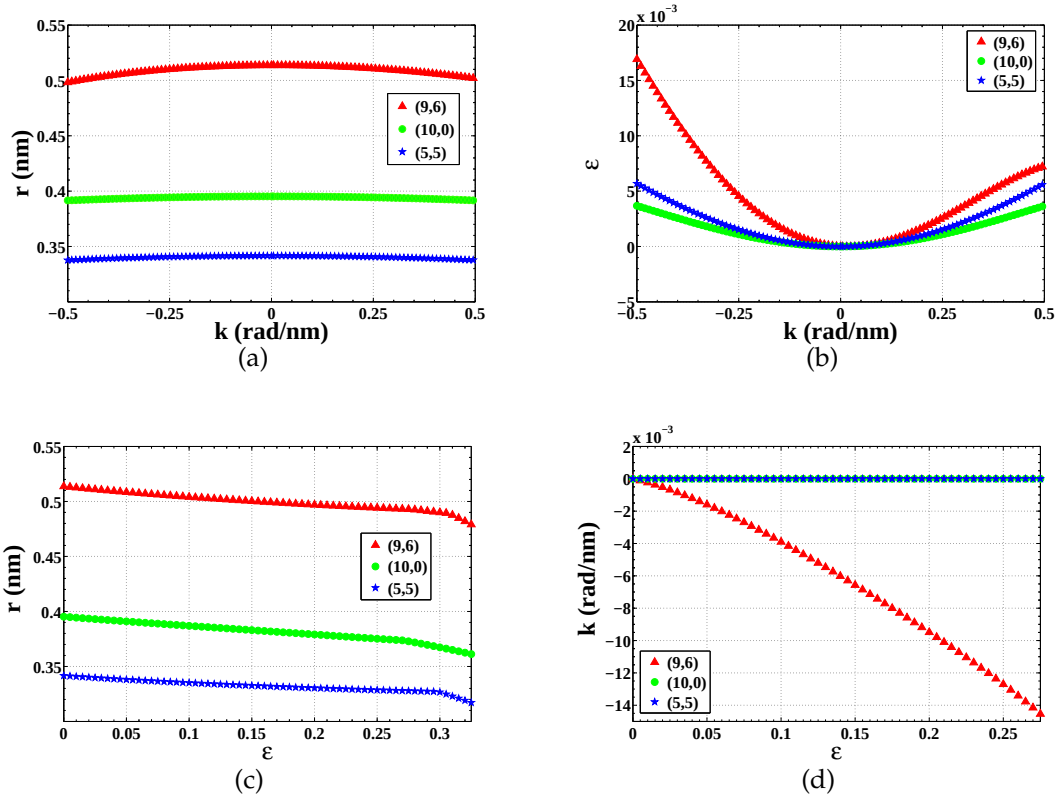

Figure 3.2: Kinematic coupling plots for representative chiral $(9, 6)$, zigzag $(10, 0)$, and armchair $(5, 5)$ SWNTs corresponding to $f(Z; k) \equiv kZ$, using parameter set 1 (Table 2.2) of the Tersoff-Brenner potential (Section 2.2).

2 (Table 2.2) of the Tersoff-Brenner potential are qualitatively similar, but quantitatively different (not shown). This aspect of the Tersoff-Brenner potential used in the quasicontinuum membrane model is discussed subsequently in Chapter 4 (Section 4.5), in estimating elastic moduli and stress-strain curves. In Figure 3.2(a), it is observed that there is a small decrease in the radii of the SWNTs for large values of the twist parameter, k. In Figure 3.2(b), it is observed that the chiral SWNT exhibits an asymmetric coupling between extension and twist, for imposed twist. The armchair and zigzag SWNTs, however, exhibit a symmetric extension $\epsilon(k)$ about $k = 0$. Further, the chiral SWNT exhibits the largest $|\epsilon|$ for large values of $|k|$. In the case of imposed extension, it is noted that the changes

in radius caused by extension (Poisson's effect [28] – Figure 3.2(c)) are, in general, much larger than those caused by twist (Figure 3.2(a)). The chiral SWNT twists under imposed extension (Figure 3.2(d)), while the armchair and zigzag SWNTs do not (i.e., the induced twists for the armchair and zigzag SWNTs are zero throughout the range of imposed extension). This behavior is related to the atomic arrangements in the SWNTs (Figure 1.1 and Appendix B). This aspect of the kinematic coupling is explored again, in detail in Section 5.5.2, using a completely independent approach with a one-dimensional rod model of SWNTs.

Some of the prior, published work related to extension-twist coupling in SWNTs is discussed in the present context. In [30], an approach is presented for using bond-stretching and bond-bending modes to describe gap energy modulation by external strains, dimensional and torsional deformations caused by charge injection, and stretch-induced torsion. The dependence of these properties on the SWNT chirality is investigated, the stretch-induced twist as a function of the chiral angle is derived, and it is shown that the stretch-induced twist vanishes for armchair and zigzag SWNTs – in agreement with the results in the present work (see also Section 5.5.2 and Appendix B). A direct quantitative comparison is not made since [30] conclude that the absolute magnitude of these effects may strongly depend on the details of the empirical model used for calculations. In [31], a nonlinear stick-spiral model is developed, based on a molecular mechanics concept, to investigate elastic behavior of an SWNT under axial, radial, and torsion conditions, including extension-twist coupling in chiral SWNTs with special attention paid to the effects of SWNT chirality and size. [51] use classical MD with the second generation reactive empirical bond order (REBO) potential [9] to characterize strain-induced twist limited to chiral SWNTs. However, the differences in the atomistic descriptions between these

and the present work make it difficult to carry out a direct comparison.

Further, it is mentioned here that a simplified version of the Tersoff-Brenner [8, 86] potential is employed in the present work (Section 2.2). The same, simplified version is also used by [2, 3, 44, 52, 101]. In particular, $F(i, j)$ (called F_{ij} in [8]) is assumed to be zero in the expression for $\bar{B}(i, j)$ in [8] (called $\bar{B}_{ij}$ in Equation 10 of [8]). The primary reason for doing this is to employ an analytically convenient form of the interatomic potential (there is no intrinsic difficulty in using the complete expressions in [8]). The consequences of using this form of the potential are discussed in detail in [12]. It is observed that the assumed form is exact for this class of problems for imposed strains of up to about 30% (after which the bond order of some of the carbon atoms changes – bonds may break and new bonds may form). This is in agreement with some earlier results on tensile yield strains of SWNTs using MD calculations at temperatures of about 600 K [97, 94]. In particular, [97] reports a strong temperature dependence on the value of the yield strain (with values as high as 55% at 50 K, decreasing to about 25% at 1200 K), and a weak dependence on the chirality of SWNTs. The assumed form is, however, exact for the imposed twist problem throughout the plotted range of imposed k ($-0.5 \leq k \leq 0.5$) because no changes are observed in the bond orders of the carbon atoms throughout this range of imposed k.

3.4.2 $f(Z; k) \equiv kZ^2$: Imposed extension problem

In the present section, numerical results are presented for imposed extension problems with $f(Z; k) \equiv kZ^2$ (this satisfies the conditions obtained in Section 3.2.2). Since this choice of deformation ($f(Z; k) \equiv kZ^2$) is difficult to realize

physically, plots of the binding energy per atom in the deformed configurations are presented (instead of kinematic coupling plots), i.e., the binding energy per atom (E_b) for representative chiral $(9, 6)$, zigzag $(10, 0)$, and armchair $(5, 5)$ SWNTs using parameter set 1 (Table 2.2) of the Tersoff-Brenner interatomic potential. As in the case of Section 3.4.1, the results from using parameter set 2 (Table 2.2) of the Tersoff-Brenner potential are qualitatively similar, but quantitatively different (not shown).

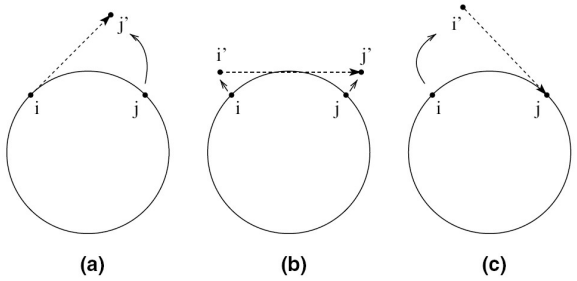

Figure 3.3: Various 'unwrapping' rules – (a) start point, (b) mid point, and (c) end point.

For the present problem, Equation 3.32 gives the best location to apply the exponential CB rule to be $Z_\alpha = \frac{1}{2}(Z_i + Z_j)$ (it is noted that since α lies on the geodesic connecting i and j, it also follows that $\Theta_\alpha = \frac{1}{2}(\Theta_i + \Theta_j)$) – henceforth referred to as the 'mid point rule' – where the deformed bond vectors obtained from the direct map and the exponential CB rule coincide. Results are also presented from applying the exponential CB rule at the locations of each of the two atoms, i and j. These are denoted as the 'start point rule' and the 'end point rule' respectively. Figure 3.3 illustrates these different 'unwrapping' rules.

In Figure 3.4, the binding energy per atom (as a function of imposed ϵ) obtained using the three deformation rules mentioned above, are compared for each type of SWNT. It is observed, as expected, that for all the SWNTs, results from the 'mid point rule' coincide exactly with those from the direct deforma-

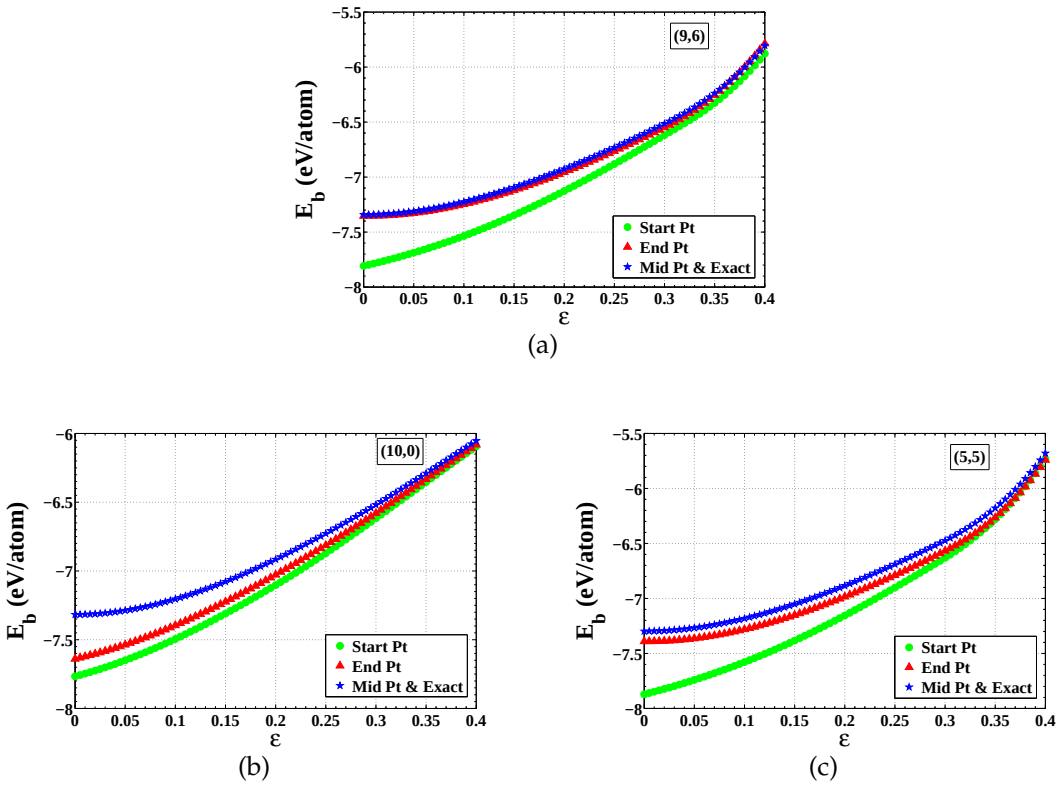

Figure 3.4: Comparison of binding energy per atom (E_b) from different rules for representative (a) chiral $(9, 6)$, (b) zigzag $(10, 0)$, and (c) armchair $(5, 5)$ SWNTs corresponding to $f(Z; k) \equiv kZ^2$, using parameter set 1 (Table 2.2) of the Tersoff-Brenner potential (Section 2.2). Results from the 'mid point' rule coincide exactly with those from the direct map (here called the exact solution).

tion map (referred to as the exact solution). The results from the 'start point' and 'end point' rules, however, do not agree with the exact solution – as expected from the discussion in Section 4.2.2.

3.5 Concluding remarks

In concluding the present chapter, the following remarks are in order.

- The modified CB rule has been employed to study deformations that are assumed to be inhomogeneous at the atomic scale. For a specific class of generalized extension-twist deformations on SWNTs, the present work deals with determining a point (on the undeformed bond) at which to evaluate **F** in the exponential CB rule (Equation 2.18) so that the deformed bond vectors coincide with the exact expression given by the direct map (Box 2).

- Numerical results are presented for extension-twist problems with $f(Z;k) \equiv kZ$ and $f(Z;k) \equiv kZ^2$ (Box 2). The 'mid point rule' (Section 3.4) is analytically shown to give a deformed bond vector coincident with the exact expression determined from the map. Numerical results for imposed extension are presented for this problem using the 'mid point rule', as well as the 'start point' and 'end point' rules (Section 3.4). It is analytically shown that in the case when $f(Z;k) \equiv kZ$, the deformed bond lengths obtained from the exponential CB rule coincide with the exact solution (Section 4.2.2) independent of the point at which **F** is evaluated. However, when $f(Z;k) \equiv kZ^2$, the 'mid point rule' alone gives the exact solution while the 'start point' and 'end point' rules do not.

- For more complicated deformations, the 'mid point rule' does not, in general, yield the exact solution. However, in these cases, if a deformation map is available, the mean value theorem can be utilized to obtain a location at which the CB rule gives the exact solution (Equation 3.32).

- In the absence of a generalization of the exponential CB rule for inhomogeneous deformations without an explicit deformation map, the 'mid point rule' can still be heuristically recommended based on the fact that the mid point is unbiased relative to any other point on a bond. A Taylor series

calculation shown in Appendix A lends further support to this idea.

In the following chapter, the two-dimensional, quasicontinuum, hyperelastic membrane SWNT model is employed to obtain elastic moduli and stress-strain curves for SWNTs subject to coupled extension and twist deformations.

CHAPTER 4

ELASTIC MODULI AND STRESS-STRAIN CURVES IN EXTENSION AND TWIST USING THE QUASICONTINUUM MEMBRANE MODEL

4.1 Introduction

The present chapter deals with the computation of elastic moduli and stress-strain curves for SWNTs subject to coupled extension and twist deformations using the quasicontinuum membrane model introduced in Section 2. The primary contributions in this chapter, to computing the stress-strain curves and elastic moduli of SWNTs, are summarized below.

4.1.1 Extension-twist coupling effects

As discussed in Chapter 3, there are notable extension-twist coupling effects in SWNTs [12, 13, 30, 31, 51]. One of the goals of the present chapter is to take these coupling effects into account in determining elastic moduli and stress-strain curves for SWNTs. Explicit expressions for the bond lengths and elastic moduli are presented in Section 4.2 to elucidate the effects of extension-twist coupling on the elastic moduli and stress-strain curves.

4.1.2 Cylindrical reference configuration

In determining these constitutive properties, as mentioned in Chapter 2 (Sections 2.1 and 2.3) and Chapter 3, a cylindrical reference configuration is em-

ployed in the quasicontinuum membrane SWNT model in the present work [12, 13, 14] rather than a planar graphene sheet [2, 3, 44, 52, 101]. This enables the study of variations in the constitutive properties, with diameter and chirality of SWNTs, that arise from the anisotropy and change in strain energy resulting from the finite deformation required to roll up a planar graphene sheet into an SWNT [2, 3]. The bond lengths are measured as Euclidean distances, and the exponential CB rule, discussed in Section 2.4, is employed to obtain bond lengths and overcome the deficiencies of the standard CB rule when applied to curved two-dimensional membranes (Section 2.4). Although [2, 3] provide an excellent demonstration of the efficacy of the exponential CB rule through FEM simulations of severe twist and bending deformations on SWNTs, the elastic moduli are still calculated for a planar graphene sheet and considered to be representative of SWNT values.

4.1.3 DFT approach

As discussed in Chapter 2, the Tersoff-Brenner empirical interatomic potential is used to model the bond energies, which enables an analytic evaluation of the derivatives of the strain energy density function rather than a numerical approach. The obtained values for the extension and twist elastic moduli indicate that they do not depend strongly on the chirality of the SWNTs [3, 14, 44, 70, 101]. The relative magnitudes of the extension and twist moduli, obtained from this approach, fall within the well known range in classical elasticity theory in most cases, and the computed values for the moduli agree well with existing experimental results and atomistic studies that employ the same interatomic potential. However, it is demonstrated in the present chapter,

that the use of the Tersoff-Brenner interatomic potential in the quasicontinuum membrane SWNT model can lead to results that depend on the values of parameters in the potential (Table 2.2). Hence, the present chapter also includes a computation of the Young's modulus using a DFT approach [48, 74] (Section 1) by performing unit cell relaxations that avoid the use of an empirical potential. A comparison between the moduli obtained from both approaches brings to notice the advantages and limitations of the corresponding methods.

The present chapter is organized as follows. The analysis of SWNTs subject to tension and torsion is presented in Section 4.2, which also contains an explicit analytic formula for the bond lengths, along with certain key expressions for evaluating stresses and elastic moduli. Details of the DFT unit cell simulations are presented in Section 4.3. Section 4.4 presents numerical values of the elastic moduli and stress-strain curves for representative chiral, armchair, and zigzag SWNTs subject to coupled extension-twist deformations, and compares the values obtained in the present work with experimental values and atomistic simulations in the literature, along with values of Young's moduli from the DFT approach in the present work. A discussion of these results, and some concluding remarks, complete the chapter.

4.2 Tension and Torsion of SWNTs

As discussed in Chapter 3, the extension-twist coupling effects in SWNTs [12, 13, 14] can be taken into account in determining their elastic moduli and stress-strain curves. It is convenient to study their constitutive behavior by prescribing a deformation map as given in Box 2 (Section 3.2) which allows exten-

sion and twist deformations to be treated in a unified manner. For clarity, this is reproduced below in Box 3 with the specific choice of $f(Z;k) \equiv kZ$, where k is the angle of twist per unit undeformed length of the SWNT modeled as a thin-walled circular cylinder (Section 3.2).

As before in Section 3.2, r and R, in Box 3, are the deformed and undeformed radii of cross-section of a thin-walled, circular cylinder respectively, γ is a parameter that captures the change in cross-sectional radius, θ and Θ are, respectively, the deformed and undeformed polar angles on the cylindrical cross-section, z and Z are the deformed and undeformed axial coordinates respectively, ϵ is the axial strain, and k is the angle of twist per unit undeformed length of the cylinder. The deformation map in Box 3 is clearly a special case of the more general deformation map (Box 2) considered in Section 3.2, in which the satisfaction of the equations of static equilibrium without body forces, as well as the equivalence between the strong and weak forms of implementing such a map, have been investigated.

$$\boxed{\begin{aligned} r &= \gamma R \\ \theta &= \Theta + kZ \\ z &= (1+\epsilon)Z \end{aligned}}$$

Box 3: The coupled extension-twist deformation map.

In the present section, the static equilibrium equations, for the specific coupled extension-twist problem in Box 3, are first presented in Section 4.2.1. Next, the expression for the interatomic bond lengths is given in Section 4.2.2 in terms of the Green-Lagrangian strain tensor components, which proves to be important in determining the stresses and elastic moduli subsequently. Finally, the

expressions for the second Piola-Kirchhoff stress, as well as the Young's and twist moduli, are presented in Section 4.2.3.

4.2.1 Static equilibrium equations

As before in Section 3.2.1, with the assumptions of the lateral surfaces of the thin-walled cylinder being traction-free and the stress measures being axisymmetric (i.e., independent of the cylindrical polar coordinate, Θ), the final forms of the equilibrium equations are (details in Section 3.2.1)

$$\begin{aligned} T_{\Theta\Theta} + 2RkT_{\Theta Z} + k^2R^2T_{ZZ} &= 0 \\ \frac{\partial}{\partial Z}[T_{\Theta Z} + kRT_{ZZ}] &= 0 \\ \frac{\partial T_{ZZ}}{\partial Z} &= 0 \quad . \end{aligned} \tag{4.1}$$

Similarly, following Section 3.2.1, the expression for the Green-Lagrangian strain tensor can be evaluated to be

$$\mathbf{E} = \frac{1}{2}\left(\gamma^2 - 1\right)(\mathbf{e}_R \otimes \mathbf{e}_R + \mathbf{e}_\Theta \otimes \mathbf{e}_\Theta) + \frac{1}{2}\gamma^2 Rk(\mathbf{e}_\Theta \otimes \mathbf{e}_Z + \mathbf{e}_Z \otimes \mathbf{e}_\Theta) + \frac{1}{2}(\gamma^2R^2k^2 + 2\epsilon + \epsilon^2)\mathbf{e}_Z \otimes \mathbf{e}_Z \quad , \tag{4.2}$$

where $\{\mathbf{e}_R, \mathbf{e}_\Theta, \mathbf{e}_Z\}$ is the set of cylindrical basis vectors spanning the undeformed configuration. Further, in relation to the deformation map in Box 3 and Equation 4.2, and the strain energy density function prescribed by the quasicontinuum hypothesis (Section 2.5), it is useful to consider the hyperelastic strain energy density function, $\widehat{W}$, as a function of γ, k, and ϵ (as in Section 3.2.2), i.e.,

$$\widehat{W}(\mathbf{E}) \equiv \widetilde{W}(\gamma, k, \epsilon) \quad . \tag{4.3}$$

From Section 3.2.2, it is recalled that the local equilibrium Equations 4.1 can be satisfied by minimizing $\widetilde{W}$ with respect to its arguments in accordance with the principle of stationary potential energy. This allows for a straightforward implementation of the coupled extension-twist deformation simulations. Again, recalling from Section 3.2.2, if ϵ is imposed, and γ and k are determined by minimization of $\widetilde{W}$, the problem is termed an imposed extension problem. On the other hand, if k is prescribed, and γ and ϵ are obtained through minimization of $\widetilde{W}$, the problem is termed as one of imposed twist. The aforementioned minimizations are all performed using a BFGS [10, 26, 33, 78] quasi-Newton minimization subroutine in the MATLAB® software.

4.2.2 Bond length deformations

Referring to the discussion in Section 2.4.3, the undeformed geodesic vector directed from atom i to atom j, when 'unwrapped' onto the undeformed tangent plane at a referential material point, is given (in cylindrical polar coordinates) by

$$\begin{aligned} \widetilde{\mathbf{A}} &= \mathcal{M}\mathbf{A} \\ &= R(\Theta_j - \Theta_i)\mathbf{e}_\Theta + (Z_j - Z_i)\mathbf{e}_Z \quad . \end{aligned} \tag{4.4}$$

The actual length of the deformed bond vector, i.e., the Euclidean distance between atoms i and j in the deformed configuration (Figure 2.5), is obtained by

'wrapping' the deformed geodesic back onto the deformed cylinder (Equation 2.18), and can be derived in terms of the cylindrical polar components of **E** as follows:

$$\begin{aligned} a(i,j) &= |\mathbf{a}| \\ &= |\mathcal{M}^{-1}\mathbf{F}(\mathbf{X})\mathcal{M}\mathbf{A}| \\ &= \sqrt{[4\gamma^2 R^2 \sin^2(\Delta\theta) + (\Delta z)^2]} \quad , \end{aligned} \tag{4.5}$$

where

$$\begin{aligned} \Delta\theta &= \frac{(E_{\Theta Z} + E_{Z\Theta})(Z_j - Z_i) + (1 + 2E_{\Theta\Theta})R(\Theta_j - \Theta_i)}{2\left[\sqrt{1 + 2E_{\Theta\Theta}}\right]\gamma R} \\ \Delta z &= \left[\sqrt{1 + 2E_{ZZ} - \frac{(E_{\Theta Z} + E_{Z\Theta})^2}{1 + 2E_{\Theta\Theta}}}\right](Z_j - Z_i) \quad . \end{aligned} \tag{4.6}$$

In the above equations, if i and j belong to different sub-lattices, the only modification required is to replace $\Theta_i \leftarrow \Theta_i + \eta_\Theta$, and $Z_i \leftarrow Z_i + \eta_Z$ in order to get the bond lengths corresponding to Equation 2.19. Otherwise, $\eta_\Theta = \eta_Z = 0$.

As shown in Section 3.3, the deformed bond length for this problem (Box 3), obtained from the exponential CB rule, is exact, i.e., it coincides with the expression obtained by directly employing the map in Box 3 to the cylindrical polar coordinates of atoms, and is also independent of the point **X** in Equation 4.5 at which the exponential CB rule is applied. Section 3.3 contains a detailed investigation of inhomogeneous deformations in which such is not the case.

4.2.3 Evaluating stresses and elastic moduli

In the present section, details are presented on evaluating Equations 3.4 and 2.22 using the strain energy density function (W) defined in Equation 2.20. It is noted that this definition is based on the binding energy for a representative carbon atom in the lattice, which involves neighboring carbon atoms as required by the multi-body coupling term in the Tersoff-Brenner interatomic potential (Equation 2.1) – typically, nearest and next-to-nearest neighbor interactions. Section 2.3 contains details on identifying the relevant bonds and calculation of the binding energy for a representative carbon atom. In the following, it is assumed that W is completely expressed in terms of Euclidean interatomic lengths alone, i.e., $W(\mathbf{E}, \boldsymbol{\eta}(\mathbf{E})) \equiv \overline{W}(a(i, j))$, where i and j refer to all the relevant carbon atoms to be considered. This can be done by expressing the required bond angles in terms of Euclidean lengths (Equation 2.7) incorporating the shift vector as mentioned following Equation 4.6. Further, all the derivatives in the following are assumed to be evaluated at $\boldsymbol{\eta} = \hat{\boldsymbol{\eta}}$, the relaxed shift vector (as in Equations 3.4 and 2.22), and summation is implied on all repeated indices over the energetically relevant bond lengths.

Referring to Equation 3.4, it follows that

$$\mathbf{T} = \left.\frac{\partial W}{\partial \mathbf{E}}\right|_{\boldsymbol{\eta}} = \frac{\partial \overline{W}}{\partial a_p}\frac{\partial a_p}{\partial \mathbf{E}} \quad . \tag{4.7}$$

Further, the individual terms comprising Equation 2.22 can be evaluated as follows:

$$\frac{\partial^2 W}{\partial \mathbf{E} \partial \mathbf{E}} = \frac{\partial^2 \overline{W}}{\partial a_m \partial a_n} \left[\frac{\partial a_m}{\partial \mathbf{E}} \otimes \frac{\partial a_n}{\partial \mathbf{E}} \right] + \frac{\partial \overline{W}}{\partial a_p} \frac{\partial^2 a_p}{\partial \mathbf{E} \partial \mathbf{E}} \tag{4.8}$$

$$\frac{\partial^2 W}{\partial \mathbf{E} \partial \boldsymbol{\eta}} = \frac{\partial^2 \overline{W}}{\partial a_m \partial a_n} \left[\frac{\partial a_m}{\partial \mathbf{E}} \otimes \frac{\partial a_n}{\partial \boldsymbol{\eta}} \right] + \frac{\partial \overline{W}}{\partial a_p} \frac{\partial^2 a_p}{\partial \mathbf{E} \partial \boldsymbol{\eta}} \tag{4.9}$$

$$\frac{\partial^2 W}{\partial \boldsymbol{\eta} \partial \boldsymbol{\eta}} = \frac{\partial^2 \overline{W}}{\partial a_m \partial a_n} \left[\frac{\partial a_m}{\partial \boldsymbol{\eta}} \otimes \frac{\partial a_n}{\partial \boldsymbol{\eta}} \right] + \frac{\partial \overline{W}}{\partial a_p} \frac{\partial^2 a_p}{\partial \boldsymbol{\eta} \partial \boldsymbol{\eta}} \tag{4.10}$$

$$\frac{\partial^2 W}{\partial \boldsymbol{\eta} \partial \mathbf{E}} = \frac{\partial^2 \overline{W}}{\partial a_m \partial a_n} \left[\frac{\partial a_m}{\partial \boldsymbol{\eta}} \otimes \frac{\partial a_n}{\partial \mathbf{E}} \right] + \frac{\partial \overline{W}}{\partial a_p} \frac{\partial^2 a_p}{\partial \boldsymbol{\eta} \partial \mathbf{E}} \quad , \tag{4.11}$$

where Equations 4.8 and 4.10 evaluate to fourth rank and second rank tensors respectively, and Equations 4.9 and 4.11 evaluate to third rank tensors. All the derivatives of $a(i, j)$ with respect to $\boldsymbol{E}$ and $\boldsymbol{\eta}$ can be analytically evaluated using Equations 4.5 and 4.6, while the derivatives of $\overline{W}$ can be analytically evaluated from the expression for the potential in Equation 2.1 (Section 2.2). It is noted that Equations 4.7–4.11 may be evaluated at any stage of deformation for which the bond lengths and shift vector have been determined (Section 4.2.1). Typically, Equation 4.7 is applied throughout the range of imposed deformation to obtain the stress-strain curves, and Equations 4.8–4.11 are evaluated at the onset of deformation ($\mathbf{E} = \mathbf{0}$) in order to obtain the linearized elastic moduli.

Now, it is straightforward to derive expressions for the Young's and twist moduli using the components of the linearized elasticity tensor at the onset of deformation ($\mathbf{E} = \mathbf{0}$). First, components of the Lagrangian elasticity tensor are obtained from Equation 2.22. Next, the non-zero components of $\mathbb{C}$ and $\mathbf{T}$, for the coupled extension-twist problem described in Box 3, are identified. The actual values of Young's modulus (Y) and twist modulus (G) are next determined from the incremental stress-strain relations that govern this coupled problem. At the onset of deformation, it follows that

$$Y = \frac{\delta T_{ZZ}}{\delta E_{ZZ}} \tag{4.12}$$

$$G = \frac{\delta T_{\Theta Z}}{2\,\delta E_{\Theta Z}} \tag{4.13}$$

in terms of the appropriate incremental stress and strain components.

From the dependence of the deformed bond lengths on the components of **E** (Equations 4.5 and 4.6), it can be concluded that the only non-zero components of $\mathbb{C}$ for this coupled extension-twist deformation (Box 3) are C_{ZZZZ}, $C_{ZZ\Theta\Theta}$, $C_{ZZ\Theta Z}$, $C_{\Theta Z\Theta Z}$, $C_{\Theta Z\Theta\Theta}$, and $C_{\Theta\Theta\Theta\Theta}$ (along with their symmetric permutations). Similarly, the only non-zero components of the stress tensor, **T**, for this extension-twist problem, can be shown to be T_{ZZ}, $T_{\Theta Z}$, and $T_{\Theta\Theta}$. The incremental stress-strain relations relevant to the determination of the Young's and twist moduli are

$$\delta T_{ZZ} = C_{ZZZZ}\,\delta E_{ZZ} + C_{ZZ\Theta\Theta}\,\delta E_{\Theta\Theta} + 2\,C_{ZZ\Theta Z}\,\delta E_{\Theta Z} \tag{4.14}$$

$$\delta T_{\Theta Z} = C_{\Theta ZZZ}\,\delta E_{ZZ} + C_{\Theta Z\Theta\Theta}\,\delta E_{\Theta\Theta} + 2\,C_{\Theta Z\Theta Z}\,\delta E_{\Theta Z} \tag{4.15}$$

$$\delta T_{\Theta\Theta} = C_{ZZ\Theta\Theta}\,\delta E_{ZZ} + C_{\Theta\Theta\Theta\Theta}\,\delta E_{\Theta\Theta} + 2\,C_{\Theta Z\Theta\Theta}\,\delta E_{\Theta Z} \quad , \tag{4.16}$$

where δ denotes an increment in the appropriate quantity. The procedure to express the Young's and twist moduli, in terms of the above components of $\mathbb{C}$, is presented below.

Evaluating the Young's modulus

The expression for the Young's modulus can be derived from a stress state resulting from simple imposed extension, in which the Lagrangian measures of axial tension and axial strain are related. In this case, an incremental stress-strain relationship for the axial tension, as shown in Equation 4.14, can be written. In order to relate δT_{ZZ} and δE_{ZZ}, the additional equations $\delta T_{\Theta Z} = 0$ and $\delta T_{\Theta\Theta} = 0$ (Equations 4.15 and 4.16 respectively), are used at the onset of deformation ($\mathbf{E} = \mathbf{0}$) to express $\delta E_{\Theta Z}$ and $\delta E_{\Theta\Theta}$ in terms of δE_{ZZ}. It is noted [12] (p. 320, footnote 3) that during imposed extensional deformation for the chiral SWNT, it is possible to have $T_{\Theta Z} \neq 0$ even if the corresponding Cauchy stress component, $\sigma_{\theta z} = 0$. However, at the onset of deformation, it is true that $\sigma_{\theta z} = T_{\Theta Z} = 0$. Finally, it follows that

$$\delta T_{ZZ} = Y \, \delta E_{ZZ} \quad , \tag{4.17}$$

where the Young's modulus, Y, is given as

$$Y = C_{ZZZZ} + \underline{\nu^{(e)}_{\Theta\Theta} \, C_{ZZ\Theta\Theta} + \nu^{(e)}_{\Theta Z} \, C_{ZZ\Theta Z}} \quad , \tag{4.18}$$

with dimensionless quantities, $\nu^{(e)}_{\Theta\Theta}$ and $\nu^{(e)}_{\Theta Z}$, defined as

$$\begin{aligned} \nu^{(e)}_{\Theta\Theta} &= \tfrac{\Delta^{(e)}_{\Theta\Theta}}{\Delta^{(e)}} \\ \nu^{(e)}_{\Theta Z} &= \tfrac{2\Delta^{(e)}_{\Theta Z}}{\Delta^{(e)}} \quad , \end{aligned} \tag{4.19}$$

where $\Delta^{(e)}$, $\Delta^{(e)}_{\Theta\Theta}$, and $\Delta^{(e)}_{\Theta Z}$ are determinants given by

$$
\begin{aligned}
\Delta^{(e)} &= \begin{vmatrix} C_{\Theta\Theta\Theta\Theta} & 2C_{\Theta Z\Theta\Theta} \\ C_{\Theta Z\Theta\Theta} & 2C_{\Theta Z\Theta Z} \end{vmatrix} \\
\Delta^{(e)}_{\Theta\Theta} &= \begin{vmatrix} -C_{ZZ\Theta\Theta} & 2C_{\Theta Z\Theta\Theta} \\ -C_{ZZ\Theta Z} & 2C_{\Theta Z\Theta Z} \end{vmatrix} \\
\Delta^{(e)}_{\Theta Z} &= \begin{vmatrix} C_{\Theta\Theta\Theta\Theta} & -C_{ZZ\Theta\Theta} \\ C_{\Theta Z\Theta\Theta} & -C_{ZZ\Theta Z} \end{vmatrix} \quad . \qquad (4.20)
\end{aligned}
$$

It is noted that the underlined terms in Equation 4.18 represent the contributions due to twisting under imposed extension and the Poisson's effect (change in SWNT diameter due to axial strain). Further, the above expression for Y is a generalized version of Equation 36 in [101] which holds in the case of no extension-twist coupling under imposed extension, and can also be obtained from evaluating the slopes of the extensional stress-strain curves at the onset of deformation. The values of Y for representative chiral, armchair, and zigzag SWNTs obtained from the above approach, as well as from the slopes of stress-strain curves, are tabulated and compared in Section 4.4.

Evaluating the twist modulus

An approach that parallels the one presented in Section 4.2.3 is followed. The expression for the twist modulus can be derived from a stress state resulting from simple imposed twist, in which the appropriate Lagrangian measures of torsional stress and strain are related. In this case, an incremental stress-strain relationship for the torsional (shear) stress can be written as shown in Equation 4.15. In order to relate $\delta T_{\Theta Z}$ and $\delta E_{\Theta Z}$, the additional equations $\delta T_{ZZ} = 0$ and

$\delta T_{\Theta\Theta} = 0$ (Equations 4.14 and 4.16 respectively), are used at the onset of deformation ($\mathbf{E} = \mathbf{0}$) to express δE_{ZZ} and $\delta E_{\Theta\Theta}$ in terms of $\delta E_{\Theta Z}$. Finally, it follows that

$$\delta T_{\Theta Z} = G\,(2\,\delta E_{\Theta Z}) \quad , \tag{4.21}$$

where the twist modulus, G, is given as

$$G = C_{\Theta Z \Theta Z} + \underline{\nu^{(t)}_{\Theta\Theta}\, C_{\Theta Z \Theta\Theta} + \nu^{(t)}_{ZZ}\, C_{ZZ\Theta Z}} \quad , \tag{4.22}$$

with dimensionless quantities, $\nu^{(t)}_{\Theta\Theta}$ and $\nu^{(t)}_{ZZ}$, defined as

$$\begin{aligned} \nu^{(t)}_{\Theta\Theta} &= \tfrac{\Delta^{(t)}_{\Theta\Theta}}{\Delta^{(t)}} \\ \nu^{(t)}_{ZZ} &= \tfrac{\Delta^{(t)}_{ZZ}}{\Delta^{(t)}} \quad , \end{aligned} \tag{4.23}$$

where $\Delta^{(t)}$, $\Delta^{(t)}_{\Theta\Theta}$, and $\Delta^{(t)}_{\Theta Z}$ are determinants given by

$$\begin{aligned} \Delta^{(t)} &= \begin{vmatrix} C_{ZZ\Theta\Theta} & C_{ZZZZ} \\ C_{\Theta\Theta\Theta\Theta} & C_{ZZ\Theta\Theta} \end{vmatrix} \\ \Delta^{(t)}_{\Theta\Theta} &= \begin{vmatrix} -C_{ZZ\Theta Z} & C_{ZZZZ} \\ -C_{\Theta Z\Theta\Theta} & C_{ZZ\Theta\Theta} \end{vmatrix} \\ \Delta^{(t)}_{ZZ} &= \begin{vmatrix} C_{ZZ\Theta\Theta} & -C_{ZZ\Theta Z} \\ C_{\Theta\Theta\Theta\Theta} & -C_{\Theta Z\Theta\Theta} \end{vmatrix} \quad . \end{aligned} \tag{4.24}$$

It is noted that the underlined terms in Equation 4.22 represent the contributions due to extension and change in diameter under imposed twist. Further, G can also be obtained from evaluating the slopes of the torsional stress-strain curves at the onset of deformation. The values of G for representative chiral, armchair and zigzag SWNTs, obtained from the above approach, as well as from the slopes of stress-strain curves, are tabulated and compared in Section 4.4.

4.3 Evaluation of Young's modulus using DFT

In the present section, representative chiral $(4,1)$, armchair $(5,5)$, and zigzag $(5,0)$ SWNTs are considered. The coordinates of all the atoms in a single translational unit cell, along with the length of each translational unit cell, are obtained using the SWNT generator in [43] ([92], for example, contains formulas to generate carbon atom coordinates in an SWNT). One translational unit cell of the $(4,1)$ SWNT contains 28 atoms, while the $(5,5)$ and $(5,0)$ SWNT unit cells each contain 20 atoms. DFT simulations are performed [5] by relaxing the coordinates of these atoms for imposed axial strains on the translational unit cell. These simulations are performed within the generalized gradient approximation (GGA) as proposed by Perdew-Burke-Ernzerhof (PBE) [64]. Ultrasoft Vanderbilt [89] pseudopotentials are used, and the wavefunctions are expanded in a plane-wave basis set with a 50 Rydberg energy cut-off and 240 Rydberg charge density cut-off [58]. A cell size of 13.8 Å $\times$ 13.8 Å is used for the coordinates perpendicular to the axial direction [58] to allow for sufficient lateral separation between neighboring SWNTs (in order to consider them to be isolated). The in-plane dimension of 13.8 Å is considered sufficient because the $(4,1)$, $(5,0)$, and $(5,5)$ SWNTs have relaxed diameters of 3.801 Å, 4.082 Å, and 6.869 Å re-

spectively. The relaxations are performed using the BFGS [10, 26, 33, 78] quasi-Newton minimization algorithm.

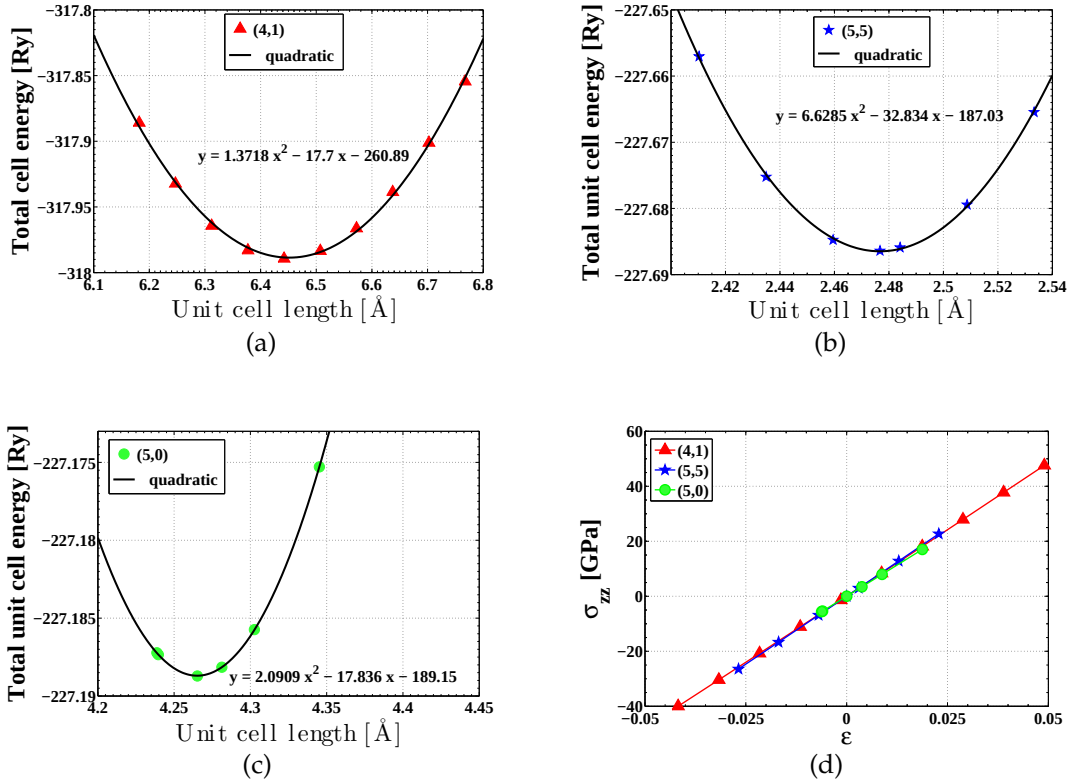

Figure 4.1: Total unit-cell relaxed energies and stress-strain plots for representative chiral $(4,1)$, zigzag $(5,0)$, and armchair $(5,5)$ SWNTs using plane-wave pseudopotential DFT (Section 4.3).

For sampling the irreducible Brillouin zone, the k-points are generated automatically using the Monkhorst-Pack algorithm [60], with grid-offsets of one-half of the lattice translation vectors [7] in the case of the $(5,5)$ and $(5,0)$ SWNTs (resulting in 4 special k-points with the appropriate lattice symmetries taken into account, for both the $(5,5)$ and $(5,0)$ SWNTs), while a Γ-point sampling (1 k-point) is used in the case of the $(4,1)$ SWNT. Although a finer k-point grid can be chosen for the $(4,1)$ SWNT, a Γ-point sampling is used in view of computational efficiency because the algorithms used in [5] are optimized for Γ-point simula-

tions. These choices are primarily dictated by the lengths of the translational unit cells and desired levels of accuracies in total unit cell energies in each case. The relaxed equilibrium configurations of the SWNTs have the following translational unit-cell lengths: 2.477 Å for the $(5,5)$, 4.265 Å for the $(5,0)$, and 6.451 Å for the $(4,1)$ SWNT. Since the translational unit-cell lengths of the considered SWNTs are less than 50% of the in-plane dimensions (13.8 Å), a finer grid along the axial direction is employed. The total unit cell energies obtained from single, self-consistent runs of a Monkhorst-Pack grid resulting in 4 special k-points (for both the $(5,5)$ and $(5,0)$ SWNTs), and a grid resulting in 15 k-points for the $(5,5)$ and 18 k-points for the $(5,0)$ SWNT, differ by less than 0.0033% (relative error) for the $(5,5)$ SWNT, and 0.0064% (relative error) for the $(5,0)$ SWNT. In the case of the $(4,1)$ SWNT, the total unit cell energies from single, self-consistent runs of a Γ-point sampling and a Monkhorst-Pack grid resulting in 4 k-points, differ by less than 0.03% (relative error). These relative errors are assumed to be acceptable.

Strains are applied by varying the axial coordinates of the carbon atoms at the edges of the tube, which are constrained to lie within a plane perpendicular to the tube axis. The other coordinates of the edge carbon atoms and all coordinates of the other carbon atoms are then relaxed at each applied strain with the optimized atomic configuration from a previous (and lower) value of strain serving as the initial configuration for the following value of strain. The converged total unit cell energies are plotted against the lengths of the translational unit cell, and a least-squares parabolic fit is performed through these data points. The L2-norms (in milli-Rydberg) of the difference between the parabolic energy fit and the actual data points, averaged over the number of data points, are 1.404, 1.511, and 0.856 for the $(4,1)$, $(5,5)$, and $(5,0)$ SWNTs, respectively.

Next, the force of tension is obtained as the slope of this parabolic fit, and the stress values are computed by dividing the force by the product of the current value of the SWNT circumference and an assumed SWNT wall thickness of 3.35 Å [14, 95, 101] (interlayer spacing in bulk graphite) – as mentioned in Section 2.5. Finally, the slopes of the stress-strain curves are used to estimate the Young's moduli. This numerical procedure (that uses the slope of the stress-strain curve) corresponds to Equation 4.17, which relates the axial stress and axial strain.

4.4 Deformation simulations and moduli values

The present section discusses stress-strain curves and elastic moduli obtained from coupled extension-twist deformations on representative SWNTs.

Stress-strain curves are presented in Figure 4.2 for both parameter sets in the Tersoff-Brenner interatomic potential (Section 2.2). In the case of imposed extension (Figures 4.2(a) and 4.2(c)), the true (Cauchy) stress, σ_{zz}, is plotted against the axial strain, ϵ. In the case of imposed twist (Figures 4.2(b) and 4.2(d)), the true (Cauchy) stress, $\sigma_{\theta z}$, is plotted against the strain measure, kR. It is noted that a constant wall thickness of 3.35 Å [14, 95, 101] is assumed in estimating these stresses. This wall thickness is assumed to be independent of the loading and merely serves to compare the numerical results with other values published in the literature. The hyperelastic model used in the present work is strictly that of a two-dimensional membrane that does not require a value for the wall thickness (Section 2.5). The slopes of the stress-strain curves serve to estimate the elastic moduli. The numerical values are further validated by computing the elastic moduli using Equations 4.18–4.20, and Equations 4.22–4.24.

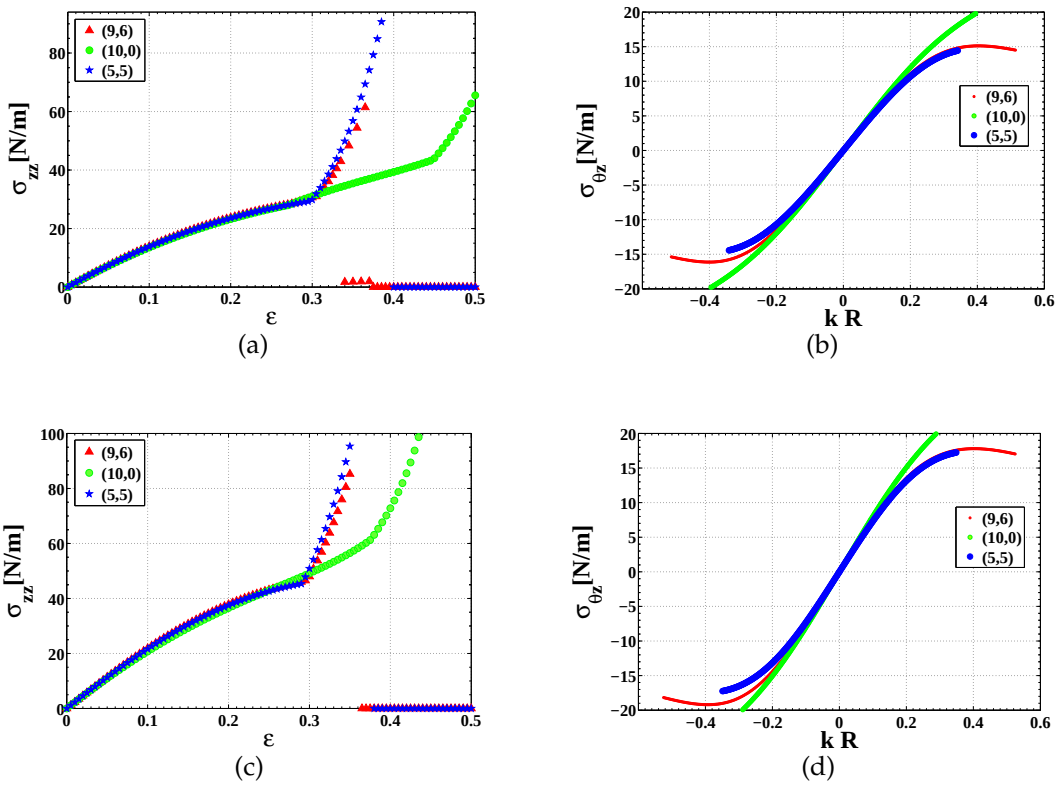

Figure 4.2: Stress-strain plots for representative chiral $(9, 6)$, zigzag $(10, 0)$, and armchair $(5, 5)$ SWNTs using parameter set 1 of the Tersoff-Brenner interatomic potential (Section 2.2) in (a) and (b), and parameter set 2 in (c) and (d).

A summary of the numerical results obtained from these calculations is presented in Tables 4.4–4.4. Although the Young's modulus (Y) and the twist modulus (G) are computed using a Lagrangian elasticity tensor, $\mathbb{C}$ (Equation 2.22), and the slopes of the (true) stress-strain curves yield Eulerian measures of the moduli, it is noted that the corresponding values are being compared at the onset of deformation ($\mathbf{E} = \mathbf{0}$), where both the Eulerian and the Lagrangian measures become identical.

As pointed out in [6, 31, 93], as well as subsequently investigated in Chapter 5, the elastic properties of SWNTs are nonlinear and strain-dependent. In

the present Chapter, however, only the moduli at the onset of deformation are reported. A more detailed discussion on how they vary over the deformation range is postponed to Chapter 5.

It is observed, from Figure 4.2, that the stress-strain curves for different SWNTs are coincident up to reasonably large strains. The values of moduli obtained from the slopes of the stress-strain curves differ by a few percent from those calculated using the elasticity tensor. This is because the slopes are approximate numerical estimates, while the values obtained from the modulus tensor calculation correspond to Equation 4.18 (for Y) and Equation 4.22 (for G), and are more accurate analytic results.

Table 4.1: Young's modulus values from slope of the stress-strain curves (Figure 4.2(a)) and modulus calculation (Equation 4.18) using parameter set 1 of the Tersoff-Brenner interatomic potential (Section 2.2) and SWNT wall thickness of 3.35 Å [14, 95, 101].

Type of SWNT	Y [GPa] (slope of curve)	Y [GPa] (modulus calculation)
$(9, 6)$ Chiral	455	470
$(5, 5)$ Armchair	455	457
$(10, 0)$ Zigzag	455	464

From Tables 4.4–4.4, a good agreement between the values obtained from the slopes of the stress-strain curves (Figure 4.2) and the ones obtained from calculation of the modulus tensor (Equations 4.18 and 4.22), is observed. The slopes of the curves in Figure 4.2 agree well with the stress-strain curves presented in [44] (for pure extension and pure twist), and the Young's moduli agree

Table 4.2: Young's modulus values from slope of the stress-strain curves (Figure 4.2(c)) and modulus calculation (Equation 4.18), with parameter set 2 of the Tersoff-Brenner interatomic potential (Section 2.2) and SWNT wall thickness of 3.35 Å [14, 95, 101].

Type of SWNT	Y [GPa] (slope of curve)	Y [GPa] (modulus calculation)
$(9, 6)$ Chiral	687	693
$(5, 5)$ Armchair	687	670
$(10, 0)$ Zigzag	687	684

Table 4.3: Twist modulus values from slope of the stress-strain curves (Figure 4.2(b)) and modulus calculation (Equation 4.22), with parameter set 1 of the Tersoff-Brenner interatomic potential (Section 2.2) and SWNT wall thickness of 3.35 Å [14, 95, 101].

Type of SWNT	G [GPa] (slope of curve)	G [GPa] (modulus calculation)
$(9, 6)$ Chiral	187	188
$(5, 5)$ Armchair	192	193
$(10, 0)$ Zigzag	176	177

well with the values reported in [101] (475 GPa for parameter set 1 and 705 GPa for parameter set 2 of the Tersoff-Brenner interatomic potential (Section 2.2)), and [3] ($\approx$ 704 GPa), assuming a wall thickness of 3.35 Å, although, as noted previously (Section 4.1.2), both these previous studies [3, 101] are performed on planar graphene sheets. The Young's moduli corresponding to parameter set 2 of the Tersoff-Brenner interatomic potential (Section 2.2) have further been reported in [101] to fall well within the range of values reported by several experimental and atomistic studies of SWNTs (for example, in [16, 59, 71, 72, 102]), although the values are smaller than a more widespread estimate of $\approx$ 1000 GPa

Table 4.4: Twist modulus values from slope of the stress-strain curves (Figure 4.2(d)) and modulus calculation (Equation 4.22), with parameter set 2 of the Tersoff-Brenner interatomic potential (Section 2.2) and SWNT wall thickness of 3.35 Å [14, 95, 101].

Type of SWNT	G [GPa] (slope of curve)	G [GPa] (modulus calculation)
$(9, 6)$ Chiral	239	240
$(5, 5)$ Armchair	245	246
$(10, 0)$ Zigzag	224	226

for the Young's modulus (close to the Young's modulus of graphene).

The values of twist moduli presented in Tables 4.4 and 4.4 have not been reported before in the literature using the quasicontinuum membrane model for SWNTs (cylindrical reference configuration), although the G values corresponding to parameter set 2 of the Tersoff-Brenner interatomic potential (Section 2.2) in Table 4.4 agree well with values for graphene reported in [3] ($\approx$ 249 GPa) using the same interatomic potential with a wall thickness of 3.35 Å. The G values corresponding to parameter set 2 of the Tersoff-Brenner interatomic potential (Section 2.2) in Table 4.4, are somewhat close, though smaller, compared to that of graphite – 330 GPa [71], and 450 GPa for SWNTs – reported in [53, 54] using an empirical force-constant model and an empirical lattice dynamics model respectively, and a value of 414 GPa for graphite and $\approx$ 390 GPa for SWNTs – reported in [66] ($\approx$ 15% lower than the value reported in [53, 54]) using a perturbation technique within a lattice-dynamical model. Since the reported Y values in this work are also somewhat smaller than the more widespread estimate of $\approx$ 1000 GPa (as also pointed out in [3, 101]), it is concluded that the quasicontinuum membrane SWNT model using the empirical Tersoff-Brenner

interatomic potential (Section 2.2) consistently underestimates both these elastic moduli. This observation is in agreement with [58] where similar conclusions are drawn for the mechanical properties of defected CNTs estimated using the second-generation Brenner potential [9] (the second-generation Brenner potential [9] has been reported in [3] to closely match the Tersoff-Brenner potential [8] (Section 2.2) in estimating elastic properties of SWNTs). It is also interesting to note that the shear modulus for nanotube ropes has been reported in several studies, for example, in [71, 72], and has been observed to be particularly small ($\approx 1 - 7$ GPa, in [71, 72]) compared to that for an individual SWNT ($\approx 200 - 300$ GPa in the present work, 450 GPa in [53, 54], and 390 GPa in [66]).

Finally, it is noted that the discussion, in Section 3.4.1, on the use of a 'simplified' version of the Tersoff-Brenner potential [8] (Section 2.2) in the quasicontinuum membrane model, is applicable in the present section as well – it is observed that the assumed form is exact (and the corresponding results reliable within the assumed model) for this class of problems for imposed strains of up to about 30% and imposed twist of up to about $-0.75 \leq kR \leq 0.75$ (after which the bond order of some of the carbon atoms changes – bonds may break and new bonds may form).

The total unit-cell energies and stress-strain curves for the $(5, 0)$, $(5, 5)$, and $(4, 1)$ SWNTs, from the DFT calculations, are plotted in Figures 4.1. The values of Young's modulus obtained from the unit-cell DFT relaxations (slopes of the stress-strain curves) are as follows: 990 GPa for the $(5, 5)$, 965 GPa for the $(4, 1)$, and 906 GPa for the $(5, 0)$ SWNT. These values are closer to the widespread estimate of $\approx$ 1000 GPa for SWNTs (for example, in [47, 48, 53, 54, 58, 59, 71, 72, 88, 102]) than the results given in Tables 4.4–4.4 from using the quasicontin-

uum membrane model with the Tersoff-Brenner empirical interatomic potential (Section 2.2).

Finally, there is a small variation in the computed Young's and twist moduli with chirality and diameter of the SWNTs, obtained from both the quasicontinuum and DFT approaches presented in this chapter. This has been investigated in the literature for both single-walled and multi-walled nanotubes, as well as nanotube ropes (for example, in [6, 15, 31, 39, 47, 51, 53, 54, 58, 59, 67, 74, 71, 72, 88, 93]). The present work captures this variation in a natural manner by assuming a cylindrical reference configuration (Section 4.1.2).

4.5 Concluding remarks

This chapter performs a study of two different approaches to estimate the elastic moduli and constitutive laws for SWNTs – a quasicontinuum membrane SWNT model using the Tersoff-Brenner empirical interatomic potential (Section 2.2), and a DFT unit-cell relaxation approach. The following remarks are in order.

- The results from the quasicontinuum approach using the Tersoff-Brenner interatomic potential with two different parameter sets (Section 2.2) yield qualitatively similar results, but quantitatively different values for the elastic moduli.
- The results (for the Young's modulus) from the DFT simulations match values from available experimental and atomistic studies better than the quasicontinuum approach, although the computations in this case are far more expensive than the quasicontinuum approach.

- SWNT twisting simulations with the DFT approach have not been attempted owing to the limitation of translational periodicity that arbitrary twist deformations do not satisfy. Therefore, the twist modulus is not calculated using the DFT approach.
- The two approaches studied in the present work – the quasicontinuum method and DFT – have been coupled in DFT-based (Kohn-Sham DFT, as well as orbital-free DFT) local quasicontinuum approaches [24] that are free of interatomic potentials fit with parameters, although this approach also has the limitation of being extremely computer intensive.
- It can be inferred, from the numerical results, that empirical interatomic potentials, in the context of a quasicontinuum approach, are best suited to obtain efficient qualitative predictions, while more accurate atomistic simulations are necessary to extract quantitatively accurate parameter values for use in suitable continuum models of atomic systems.

The next chapter presents the one-dimensional SWNT rod model developed in the present dissertation.

CHAPTER 5

ONE-DIMENSIONAL COSSERAT ROD MODEL

5.1 Introduction

The focus of the present chapter is an atomistic-continuum model of SWNTs based on an elastic rod theory which can exhibit geometric as well as material nonlinearity [38]. In particular, the SWNT is modeled as a one-dimensional elastic continuum with some finite thickness bounded by the lateral surface. Exploitation of certain symmetries in the underlying atomic structure leads to suitable representations of the continuum elastic strain energy density in terms of strain measures that capture extension, twist, bending, and shear deformations [38]. Bridging between the atomic scale and the effective continuum is carried out by parameterization of the continuum elastic energy and determination of the parameters using unit-cell atomistic simulations over a range of deformation magnitudes and types. Specifically, the proposed model takes into account (a) bending, (b) twist, (c) shear, (d) extension, (e) coupled extension and twist, and (f) coupled bending and shear deformations. The extracted parameters reveal benefits of accounting for important anisotropic and large-strain effects as improvements over employing traditional, linearly elastic, isotropic, small-strain continuum models to simulate deformations of SWNTs. It is envisioned that the proposed approach and the extracted model parameters can serve as a useful input to simulations of SWNT deformations using existing nonlinearly elastic continuum rod codes based, for example, on the finite element method (FEM).

5.1.1 Motivations, contributions and organization

The following are viewed as the key motivations and contributions of the present work:

- Linearized, isotropic elastic properties adequately describe material behavior under small strains. However, in SWNTs undergoing large strains, there are effects such as the coupling between extension and twist [12, 13, 14, 30, 31, 51] (investigated in Chapters 3 and 4 in the present dissertation) which would be undetectable in an isotropic material. While these studies demonstrate the presence of anisotropy at large strains, it is of interest to also explore and characterize other deformation modes and the couplings thereof in SWNTs. The proposed rod model for SWNTs in the present work is capable of material as well as geometric nonlinearity and takes into account (a) bending, (b) twist, (c) shear, (d) extension, (e) coupled extension and twist, and (f) coupled bending and shear deformations. Prior, published work on elastic moduli has taken into account cases (a)−(d), individually, for small strains, and past work, including [12, 13, 14, 30, 31, 51], and Chapters 3 and 4 in the present dissertation, has considered case (e). But this is the first effort at a unified large-strain approach that takes into account all of these modes for SWNTs.
- While two-dimensional membrane models of SWNTs (for example, in [2, 3, 12, 13, 14]) have been useful to predict localized effects such as buckled mode shapes of the effective continuum, they may not be computationally efficient to model global behavior of long SWNTs (microns in length) of interest in nano-oscillators (for example, in [75, 87]). A one-dimensional model is better suited to such an application. However, one-dimensional

models published so far are limited by linearly elastic and isotropic material assumptions which do not take into account the aforementioned couplings.

- Finally, since this is a parameterized continuum model of an atomic system, it is possible to apply this model, by suitable parameter estimation, to other atomic systems such as silicon [76] or boron nitride [32] nanotubes by use of appropriate lattices and energetic descriptions to perform unit cell simulations.

More specifically, in the present work, the SWNT is modeled as a one-dimensional continuum curve joining the centroids of a stack of rigid cross-sections whose motions are tracked by a set of orthonormal basis vectors (called 'directors' – Section 5.2) attached to each cross-section (Figure 5.1). Motions of the directors, viewed as material fibers in the cross-section, determine strain measures for the rod – extension, twist, shear (rotations of cross-sections about in-plane directors), and bending strains. The nonlinearly elastic strain energy density is obtained from representation theorems proved in [38] by invoking principles of material objectivity (Section 5.3.1) and transverse material symmetry (Section 5.3.2). By choosing an explicit representation, the strain energy density is expressed as a function of the strains. The coefficients in this expression capture effects of direct extension, twist, bending, and shear, as well as coupled extension-twist and bending-shear. The atomistic-continuum bridging is performed by determining these coefficients from unit cell simulations.

This chapter is organized as follows. Section 5.2 discusses the kinematics of the Cosserat rod model and defines the strain measures in the theory. Section 5.3 presents a hyperelastic constitutive model (in which the stress-strain rela-

tionship derives from a strain energy density function) that provides the means to model geometric as well as material nonlinearity including representations of the strain energy density arising from physical restrictions of objectivity and transverse material symmetry. Section 5.4 motivates the applicability of the hyperelastic constitutive model to SWNTs and presents the atomistic-continuum bridging hypothesis that enables application of the rod model to SWNTs. Section 5.5 presents some details of the parameter-fitting procedure including numerical results for the parameters over a range of deformation magnitudes and types. A discussion of these results, and some concluding remarks, complete the chapter.

5.2 Kinematics of the Cosserat rod model

The present section describes the kinematics of static deformations in the Cosserat rod model including definitions of the strain measures and their physical significance. This section serves as a precursor to a later discussion on the constitutive model and strain energy density representations.

The rod model has been successful in capturing deformations of a variety of long, slender structures such as marine cables [36], MEMS components [11], SWNTs [34], and DNA [4, 45, 55, 90], each having their respective material constitutive behavior. The rod model is a large deformation, nonlinearly elastic generalization of models such as the Bernoulli-Euler and Timoshenko beams [28] that are restricted to small strains and linearly elastic materials. This generalization enables capturing aspects of systems such as DNA and SWNTs that are not portrayed at small strains such as the coupling between different defor-

mation modes [12, 13, 14, 45, 55]. The focus of the present work is to develop a rod model of SWNTs that is based on the underlying atomic structure and able to capture primary deformation modes as well as characterize the couplings between them.

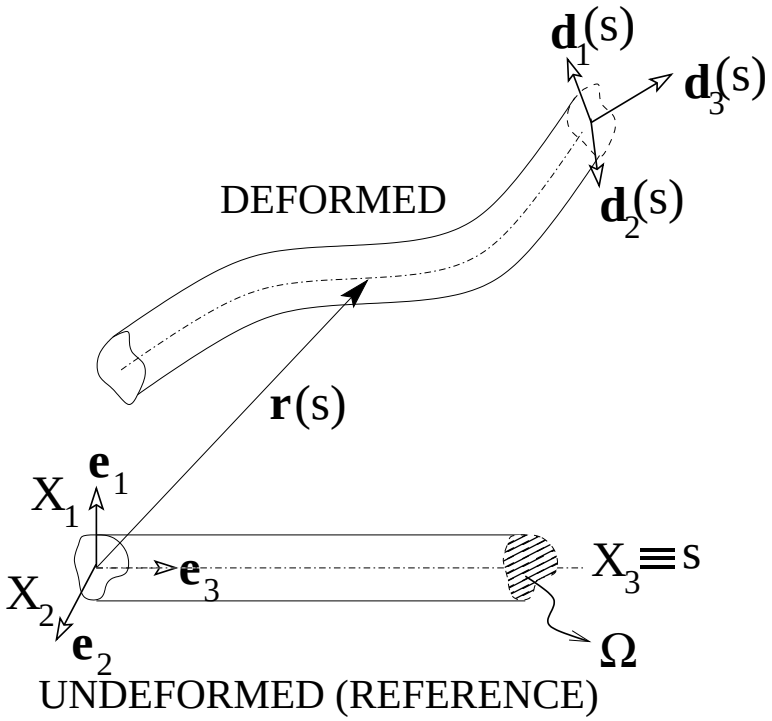

Figure 5.1: Cosserat rod as defined by the centroidal curve and directors.

Referring to Figure 5.1, $\{\mathbf{e}_1, \mathbf{e}_2, \mathbf{e}_3\}$ is assumed to denote a fixed, right-handed, orthonormal basis. It is assumed that the reference configuration of the rod is straight, stress-free and parallel to $\mathbf{e}_3$ with a prismatic cross-section, and that plane sections remain plane after deformation. Rods that are initially bent – a common situation in practice – can be modeled by extending the theory presented below. Let the arc-length coordinate (of the centerline) in the undeformed rod be denoted by s, and the position vector (with respect to some fixed origin) of the material point originally at s in the reference configuration be denoted by $\mathbf{r}(s)$. Let the rotation of the cross-section spanned by $\{\mathbf{e}_1, \mathbf{e}_2\}$ at s in the

undeformed rod be denoted by $\mathbf{R}(s)$. The first two unit vectors of the orthonormal field defined by

$$\mathbf{d}_i(s) = \mathbf{R}(s)\mathbf{e}_i; \quad i = 1, 2, 3 \tag{5.1}$$

are called directors in the special Cosserat theory employed here, from which it follows that

$$\mathbf{d}_i \cdot \mathbf{d}_j = \delta_{ij}, \quad \mathbf{d}_3 = \mathbf{d}_1 \times \mathbf{d}_2; \quad i, j = 1, 2, 3 \quad , \tag{5.2}$$

where δ_{ij} is the Kronecker delta function defined previously in Equation 3.36.

The deformed configuration of the rod is uniquely specified by the fields $\mathbf{r}(s)$ and $\mathbf{R}(s)$. Differentiation of Equation 5.1 with respect to s (denoted by primes) yields

$$\mathbf{d}_i' = \mathbf{R}'\mathbf{R}^T\mathbf{d}_i; \quad i = 1, 2, 3 \quad . \tag{5.3}$$

Since the tensor field

$$\mathbf{K} \equiv \mathbf{R}'\mathbf{R}^T \tag{5.4}$$

is skew-symmetric, there is a unique vector field, κ, such that

$$\mathbf{d}_i' = \kappa \times \mathbf{d}_i; \quad i = 1, 2, 3 \quad , \tag{5.5}$$

i.e., κ is the axial vector of $\mathbf{K}$. Differentiation of $\mathbf{r}(s)$ with respect to s gives[1]

$$\mathbf{r}' = \nu_i \mathbf{d}_i \quad , \tag{5.6}$$

while

$$\kappa = \kappa_i \mathbf{d}_i \quad . \tag{5.7}$$

The scalars ν_i, κ_i are the 'strains' in this theory [1] – ν_1, ν_2 are 'shears', ν_3 is the axial 'stretch' (the *true* stretch in the length of the centerline is given by $| \mathbf{r}' | = \sqrt{{\nu_1}^2 + {\nu_2}^2 + {\nu_3}^2}$), κ_1, κ_2 are 'curvatures', and κ_3 is the 'twist'.

Examples of the primary deformation modes are given in Figure 5.2 to illustrate the physical meanings of these strain definitions.

From Figure 5.2(a), the only non-zero strain is the axial strain, $\epsilon \equiv \nu_3 - 1$, while in Figure 5.2(b), κ_3 physically corresponds to the angle of twist per unit undeformed length. From Figure 5.2(c), the shear strain, ν_1, is related to the angle of shear, α, while the true stretch is $\sqrt{1 + \alpha^2}$. Finally, from Figure 5.2(d), κ_2 corresponds to the bending angle per unit undeformed length (L), otherwise known as the bending curvature. The deformed length of the rod is given by the arc length $\lambda\gamma L$, and is equal to the undeformed length (L) in the case of bending without stretching the centerline if $\lambda\gamma = 1$, in which case the curvature, γ, expectedly results to be the reciprocal of λ, the radius of curvature.

[1] Throughout this chapter, lower case Latin indices range from 1 to 3 while lower case Greek indices range from 1 to 2. Indices repeated in the same term are summed over their respective ranges unless explicitly stated otherwise.

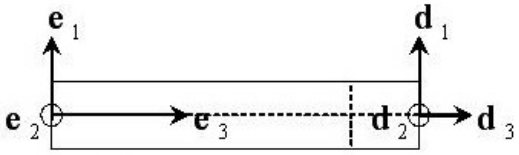

$$\mathbf{r}(s) = \lambda s \mathbf{e}_3$$

$$\mathbf{d}_1 \equiv \mathbf{e}_1, \mathbf{d}_2 \equiv \mathbf{e}_2, \mathbf{d}_3 \equiv \mathbf{e}_3$$

$$\boxed{\nu_3 = \lambda}$$

(a) Extension

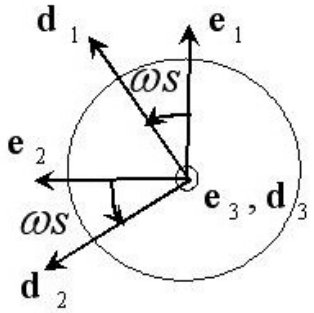

$$\mathbf{r}(s) = s\mathbf{e}_3$$

$$\begin{Bmatrix} \mathbf{d}_1 \\ \mathbf{d}_2 \\ \mathbf{d}_3 \end{Bmatrix} = \begin{bmatrix} \cos \omega s & \sin \omega s & 0 \\ -\sin \omega s & \cos \omega s & 0 \\ 0 & 0 & 1 \end{bmatrix} \begin{Bmatrix} \mathbf{e}_1 \\ \mathbf{e}_2 \\ \mathbf{e}_3 \end{Bmatrix}$$

$$\boxed{\kappa_3 = \omega, \ \nu_3 = 1}$$

(b) Twist

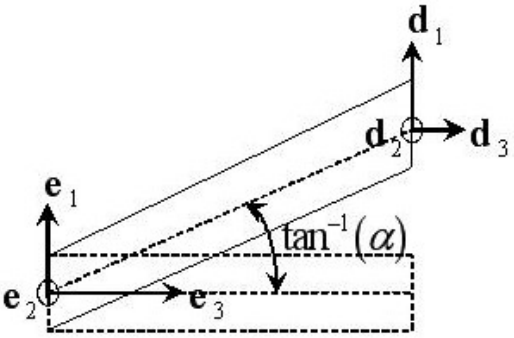

$$\mathbf{r}(s) = \alpha s \mathbf{e}_1 + s\mathbf{e}_3$$

$$\mathbf{d}_1 \equiv \mathbf{e}_1, \mathbf{d}_2 \equiv \mathbf{e}_2, \mathbf{d}_3 \equiv \mathbf{e}_3$$

$$\boxed{\nu_1 = \alpha; \ \nu_3 = 1}$$

(c) Shear in the 1 – 3 plane

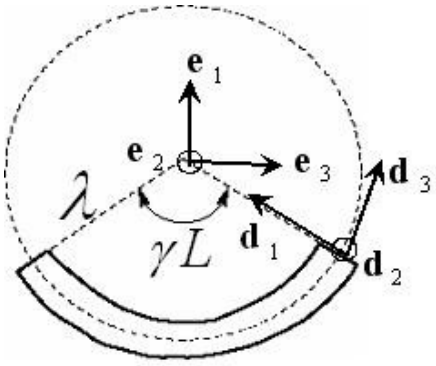

$$\mathbf{r}(s) = -\lambda \mathbf{d}_1$$

$$\begin{Bmatrix} \mathbf{d}_1 \\ \mathbf{d}_2 \\ \mathbf{d}_3 \end{Bmatrix} = \begin{bmatrix} \cos \gamma s & 0 & -\sin \gamma s \\ 0 & 1 & 0 \\ \sin \gamma s & 0 & \cos \gamma s \end{bmatrix} \begin{Bmatrix} \mathbf{e}_1 \\ \mathbf{e}_2 \\ \mathbf{e}_3 \end{Bmatrix}$$

$$\boxed{\kappa_2 = \gamma, \ \nu_3 = \lambda\gamma}$$

(d) Bending in the 1 – 3 plane

Figure 5.2: Cosserat rod kinematics and strain measures in some primary deformation modes.

5.3 Hyperelastic constitutive model and strain energy representations

For a hyperelastic rod, the existence of a differentiable, scalar-valued, strain energy density function, $\Phi(\mathbf{r}', \mathbf{R}, \mathbf{R}', s)$, can be assumed, such that the integral

$$\int_0^L \Phi ds \tag{5.8}$$

represents the total strain energy of a rod of undeformed length L. Next, restrictions on the form of Φ are imposed due to material objectivity and transverse material symmetry. The representations of Φ that arise from each case are presented below. The following sub-sections are intended to summarize the main results from strain energy representations [38] that are relevant to the present work.

5.3.1 Material objectivity

It is required that the strain energy density function, Φ, satisfy the principle of material objectivity, namely, invariance of its functional form under superposed rigid body motions, as follows:

$$\Phi(\mathbf{Q}\mathbf{r}', \mathbf{Q}\mathbf{R}, \mathbf{Q}\mathbf{R}', s) = \Phi(\mathbf{r}', \mathbf{R}, \mathbf{R}', s) \forall \mathbf{Q} \in O(3) \quad . \tag{5.9}$$

In particular, the choice $\mathbf{Q} = \mathbf{R}^T$ gives [38]

$$\Phi = W(\nu_1, \nu_2, \nu_3, \kappa_1, \kappa_2, \kappa_3, s) \quad . \tag{5.10}$$

Further, the internal contact force, $\mathbf{n}(s)$, and the internal contact couple, $\mathbf{m}(s)$, respectively, acting on the cross-section originally at s in the reference configuration, can be obtained by application of the stationary potential energy principle to get [38]

$$\mathbf{n} = n_i \mathbf{d}_i; \quad \mathbf{m} = m_i \mathbf{d}_i \quad , \tag{5.11}$$

with

$$n_i = \frac{\partial W}{\partial \nu_i}; \quad m_i = \frac{\partial W}{\partial \kappa_i}; \quad i = 1, 2, 3 \quad , \tag{5.12}$$

where n_1, n_2 are 'shear forces', n_3 is the 'axial force', m_1, m_2 are 'bending moments', and m_3 is the 'torque' or 'twisting moment'.

5.3.2 Transverse material symmetry

In the present section, symmetry-based restrictions on the functional form of the strain energy density, W (Equation 5.10), are considered, to present representations of W.

Definitions

Let a proper rotation of the rod about $\mathbf{e}_3$ by an angle $\theta(0 \leq \theta < 2\pi)$ (illustrated in Figure 5.3) be represented by $\mathbf{Q}_\theta$, and a reflection of the rod across the plane spanned by $\mathbf{e}_1$ and $\mathbf{e}_3$ be represented by E. Further, let the matrix representation of any two-tensor, with respect to the fixed basis $\{\mathbf{e}_1, \mathbf{e}_2, \mathbf{e}_3\}$, be denoted by an overbar. Then, with respect to $\{\mathbf{e}_1, \mathbf{e}_2, \mathbf{e}_3\}$,

$$\overline{E} = \begin{pmatrix} 1 & 0 & 0 \\ 0 & -1 & 0 \\ 0 & 0 & 1 \end{pmatrix} \tag{5.13}$$

and

$$\overline{Q}_\theta = \begin{pmatrix} \cos\theta & -\sin\theta & 0 \\ \sin\theta & \cos\theta & 0 \\ 0 & 0 & 1 \end{pmatrix} . \tag{5.14}$$

Next, the group of proper rotations, $SO_C(2) \equiv \{\overline{Q}_\theta : 0 \leq \theta < 2\pi\}$, and the orthogonal group of rotations and reflections, $O_C(2) \equiv \{\overline{Q}_\theta, \overline{E}\,\overline{Q}_\theta : 0 \leq \theta < 2\pi\}$, are defined.

To motivate the definition of transverse material symmetry, a deformation of the rod corresponding to some configuration $(\mathbf{r}, \mathbf{R})$ with associated strains ν_i, κ_i $(i = 1, 2, 3)$, is imagined. Next, the straight, undeformed rod is subject to either a rotation or reflection, $\mathbf{P}$, and then the same deformation as before is imagined to be applied to the rotated or reflected rod, the net effect corresponding to the configuration $(\mathbf{r}, \mathbf{RP})$. The accompanying strains can now be determined,

and a transverse symmetry, **P**, can be defined [38] as an undetectable transformation that does not change the strain energy density function, i.e., $\overline{P} \in O_C(2)$ such that, if

$$\overline{v} = \begin{pmatrix} v_1 \\ v_2 \\ v_3 \end{pmatrix} \tag{5.15}$$

and

$$\overline{k} = \begin{pmatrix} \kappa_1 \\ \kappa_2 \\ \kappa_3 \end{pmatrix} \quad , \tag{5.16}$$

then

$$W(\overline{P}\overline{v}, \det(\overline{P})\overline{P}\overline{k}, s) = W(\overline{v}, \overline{k}, s) \quad . \tag{5.17}$$

The group of symmetry transformations that satisfy Equation 5.17 form the transverse material symmetry group of the rod. In the following sub-sections, specific symmetry transformations relevant to rods with helical microstructures are considered. Their application to SWNTs is motivated, and strain energy representations derived from the corresponding restrictions they impose, are presented.

Transverse hemitropy and isotropy

A transversely hemitropic rod is defined as one in which the symmetry transformation group $\overline{P} \equiv$ entire $SO_C(2)$.

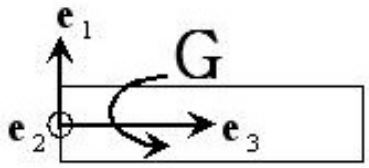

Figure 5.3: Rotational symmetry **G** about $\mathbf{e}_3$.

Further, a transversely isotropic rod can be defined as one in which the symmetry transformation group $\overline{P} \equiv$ entire $O_C(2)$. It can be shown [38] that a rod is transversely hemitropic if and only if

$$W(\overline{v}, \overline{k}, s) \equiv \Gamma_{hemi}(v_\alpha v_\alpha, v_3, v_\alpha \kappa_\alpha, \kappa_\alpha \kappa_\alpha, \varepsilon_{\alpha\beta} v_\alpha \kappa_\beta, \kappa_3) \quad , \tag{5.18}$$

where $\varepsilon_{\alpha\beta}$ is the alternating symbol, i.e., $\varepsilon_{\alpha\beta} v_\alpha \kappa_\beta = v_1 \kappa_2 - v_2 \kappa_1$. Further, a transversely hemitropic rod is also transversely isotropic if and only if [38]

$$W(\overline{v}, \overline{k}, s) \equiv \Gamma_{iso}(v_\alpha v_\alpha, v_3, (v_\alpha \kappa_\alpha)^2, \kappa_\alpha \kappa_\alpha, \varepsilon_{\alpha\beta} v_\alpha \kappa_\beta, (\kappa_3)^2, v_\alpha \kappa_\alpha \kappa_3) \quad , \tag{5.19}$$

where Γ_{hemi} and Γ_{iso} are reduced forms of the strain energy density function.

5.3.3 Flip symmetry

Yet another symmetry that can be defined for rods corresponds to invariance of the strain energy density function under proper 180° rotations about axes within the cross-section. This is illustrated in Figure 5.4.

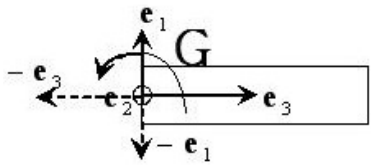

Figure 5.4: Flip symmetric operation **G** about $\mathbf{e}_2$.

It can be shown [38] that if a rod is flip symmetric in addition to being transversely hemitropic or isotropic, the strain energy density function is independent of '$\varepsilon_{\alpha\beta}\nu_\alpha\kappa_\beta$' in Equations 5.18 and 5.19. Further, if the strain energy density function were truncated at quadratic order and assumed to be explicitly independent of s, it follows that the most general quadratic representation of the strain energy density function for transversely hemitropic and flip symmetric rods is of the form [38]

$$W = \frac{1}{2}[A\kappa_\alpha\kappa_\alpha + B{\kappa_3}^2 + C\nu_\alpha\nu_\alpha + D\epsilon^2 + 2E\epsilon\kappa_3 + 2F\nu_\alpha\kappa_\alpha] \quad , \tag{5.20}$$

where, as mentioned before, $\epsilon \equiv \nu_3 - 1$ (the extensional strain), and A, B, C, D, E, F are material constants. A, B, C, and D are the bending, twisting, shearing, and extensional 'moduli' respectively, E is the extension-twist coupling (studied previously in Chapters 3 and 4 in the present dissertation [12, 13]) coefficient, and F the bending-shear coupling coefficient. Further, imposing the physically realistic assumption that the quadratic form 5.20 is positive definite, the following

necessary and sufficient conditions [38] on the material constants are obtained for positive-definiteness:

$$A, B, C, D > 0; \quad BD - E^2 > 0; \quad AC - F^2 > 0 \quad . \tag{5.21}$$

Further, for transversely isotropic rods, the 'coupling constants' vanish, i.e., $E = F = 0$.

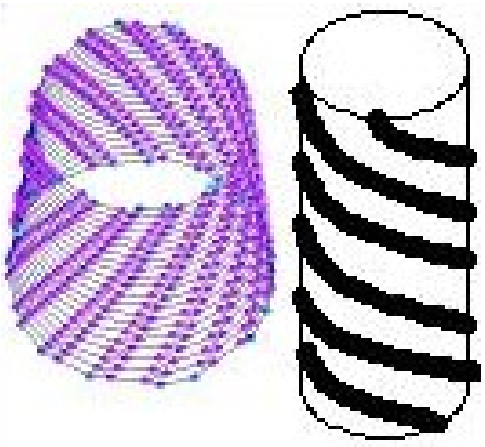

Figure 5.5: Helical idealization of a chiral SWNT.

In the context of a constitutive law for SWNTs, as illustrated in Figure 5.5, it is observed that SWNTs usually have only a small number of atoms around their circumference compared to their length and hence would fail to satisfy transverse hemitropy in a strict sense. However, helical symmetries can be identified and exploited as discussed in the next sub-section.

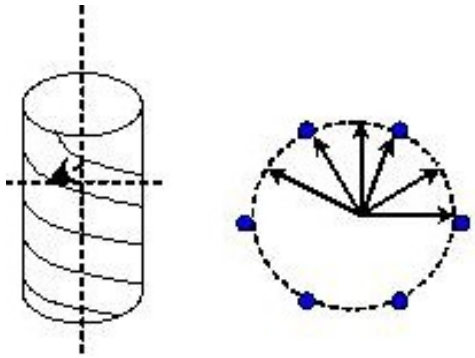

Figure 5.6: Single and multiple (for $n = 6$) axes of helical symmetry.

5.3.4 Single and multiple helical symmetry

It is observed that rods possessing a single-helical structure exhibit a special flip symmetry (180° rotation invariance) about a unique axis passing through the intersection of the helix with a plane perpendicular to the rod axis (as illustrated in Figure 5.6) at any point along the axis. This symmetry axis 'rotates' as we move from one cross-section to another along the length of the rod (Figure 5.6).

Further, in the case of chiral SWNTs, the atomic arrangement can be viewed as comprising of multiple helices (Figure 5.5). The number of such helices can be computed as a function of the chirality of the SWNT (Appendix B). In this case, there exist two or more equally spaced flip-symmetric axes (Figure 5.5). Consequently, it can be shown [38] that for rods exhibiting $n-$fold multiple helical symmetry with $n \geq 3$ (true for most SWNTs grown experimentally in practice), the most general quadratic strain energy density is identical to the case of transverse hemitropy + flip symmetry, i.e., the strain energy density function *up to quadratic order* is the same as Equation 5.20. Further, when $n \to \infty$ (relevant to SWNTs with very large diameters – Appendix B), the strain energy density function is identical to the case of transverse hemitropy + flip symmetry *up to*

any order. Since the atomic arrangement in armchair and zigzag SWNTs can be treated as special cases of a chiral SWNT, the above description applies to such SWNTs as well (Appendix B). Hence, the strain energy density function (which provides the constitutive model for a hyperelastic rod) at least up to quadratic order for SWNTs is immediately realized once the parameters A, B, C, D, E, F in Equation 5.20 can be evaluated for SWNTs.

5.4 Atomistic-continuum bridging hypothesis

Bridging of the Cosserat rod model to SWNTs (outlined in Figure 5.7) is performed by determining the coefficients in Equation 5.20 subject to the constraints in Equation 5.21 through sufficient number of unit cell atomistic simulations performed on a representative chiral $(9, 6)$ SWNT, capturing the primary deformation modes and their corresponding energies. As mentioned in Section 1.1, the SCC-DFTB method [21, 22, 27] is employed to perform the atomistic simulations in this work.

The SWNT unit cell has a diameter of 1 *nm*, length of 2 *nm*, and contains 228 atoms with 3 atoms at each axial location which are used to define cross-sectional planes and directors as required in the rod model (Section 5.2). Simulations are performed over a range of imposed deformation magnitudes corresponding to extension, twist, bending (in the $1-3$ as well as $2-3$ planes), and shear (in the $1-3$ as well as $2-3$ planes). In each case, the strains are imposed by fixing certain degrees of freedom of the end planes of the unit cell and allowing the rest of the atoms to relax to the local energy minimum. In this relaxed configuration, the strain energy is computed by subtracting away the energy

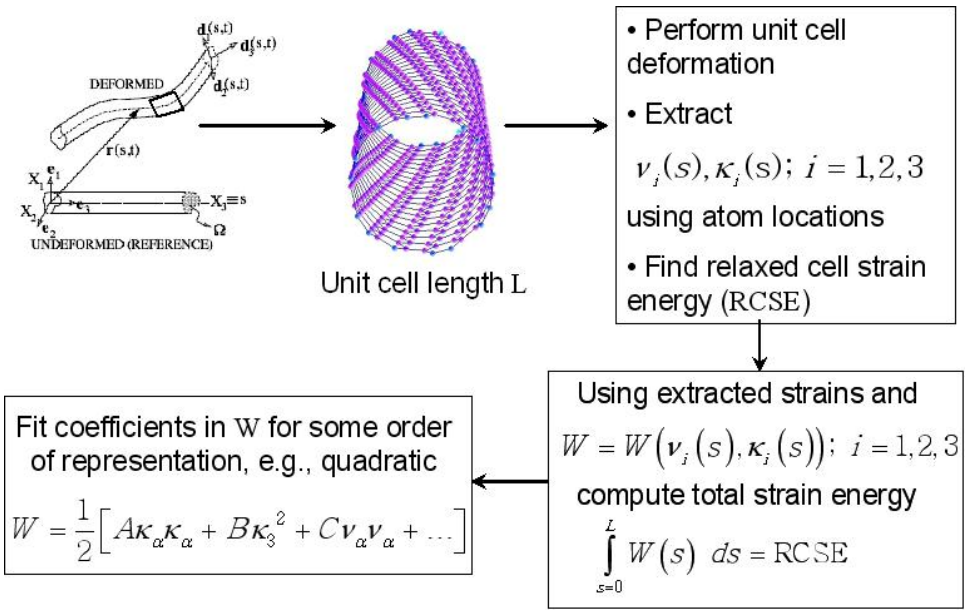

Figure 5.7: Atomistic-continuum bridging approach through parameter estimation.

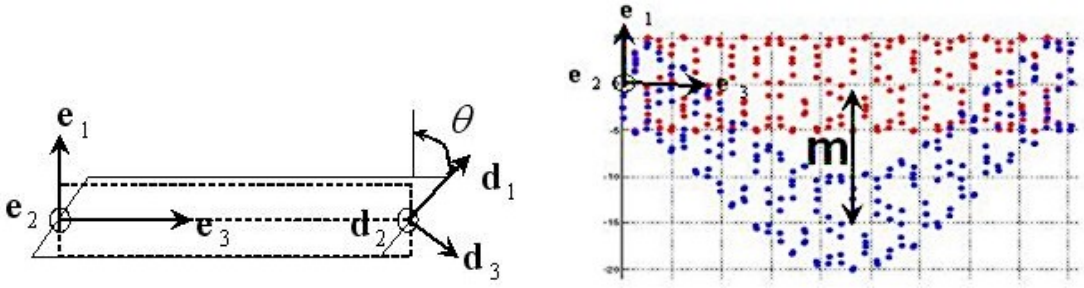

(a) Imposed shear (in 1−3 plane) using angles of rotation (θ) of cross-sections about in-plane axes

(b) Imposed bending (in 1 − 3 plane) using mid point deflections (m) of the centroidal curve – Figure 5.1

Figure 5.8: Imposed deformation profiles in shear and bending deformations.

corresponding to the undeformed configuration and the induced strains are extracted by using the relaxed atomic locations (3 atoms at each axial location in the (9, 6) SWNT) to find the deformed cross-sectional planes and orientations of the directors as required in the rod model.

Simulations of imposed extension, shear (by rotations of cross-sectional

planes about the two in-plane axes – Figure 5.8(a)), and bending (Figure 5.8(b)) are carried out with periodic boundary conditions, while imposed twist simulations are performed on a finite tube by capping the carbon atoms at the ends with hydrogen atoms because of arbitrary twist deformations not satisfying periodicity. Further, in order to use a bending deformation pattern that satisfies periodicity at the ends, a particular bent profile corresponding to a beam clamped at both ends (zero slopes and bending deflections at both ends leading to a quartic bent shape) is chosen with maximum deflection at the mid point (Figure 5.8(b)). The equation of interest is Equation 5.20. The strains extracted using the aforementioned procedure are, in general, functions of the axial coordinate, s. In order to find the coefficients A, B, C, D, E, F, Equation 5.20 is integrated on both sides with respect to the axial coordinate, s, (carried out using the trapezoidal rule in the present work) over the length of the unit cell, L, at each step of imposed extension, twist, bending, and shear to set up a rectangular system of the form

$$[M]_{nsim\times 6}\{u\}_{6\times 1} = \{f\}_{nsim\times 1} \quad , \tag{5.22}$$

where $nsim \gg 6$ is the total number of simulation steps including all the deformation modes, and $\{u\} = \{A, B, C, D, E, F\}^T$. As an illustration, let the relaxed cell strain energy (Figure 5.7) of a particular simulation step j, $1 \leq j \leq nsim$, with associated strains $\nu_i^{(j)}(s), \kappa_i^{(j)}(s)$ $(i = 1, 2, 3)$ – either imposed or induced – be denoted by $RCSE^{(j)}$. Then, the elements of the j^{th} row in Equation 5.22 are

$$M_{j1} = \int_0^L \frac{1}{2}\kappa_\alpha{}^{(j)}(s)\kappa_\alpha{}^{(j)}(s)ds;\ M_{j2} = \int_0^L \frac{1}{2}\kappa_3{}^{(j)^2}(s)ds;\ M_{j3} = \int_0^L \frac{1}{2}\nu_\alpha{}^{(j)}(s)\nu_\alpha{}^{(j)}(s)ds;$$

$$M_{j4} = \int_0^L \frac{1}{2}\epsilon^{(j)^2}(s)ds;\ M_{j5} = \int_0^L \epsilon^{(j)}(s)\kappa_3{}^{(j)}(s)ds;\ M_{j6} = \int_0^L \nu_\alpha{}^{(j)}(s)\kappa_\alpha{}^{(j)}(s)ds \tag{5.23}$$

and

$$f_j = RCS\,E^{(j)} \quad . \tag{5.24}$$

The system of Equations 5.22 is solved by minimizing $\| [M]\{u\} - \{f\} \|_2$ in a constrained least-squares fitting procedure with the set of constraints in Equation 5.21 (using a gradient-based, constrained minimization subroutine in the MATLAB® software), where

$$\| \{x\} \|_2 = \sqrt{x(1)^2 + x(2)^2 + \ldots + x(n)^2} \tag{5.25}$$

for any arbitrary vector, $\{x\}$, of length n.

5.5 Numerical results and discussion

The following are simplifying assumptions that are found to aid the parameter fitting procedure outlined in Section 5.4, and important observations made during that fitting:

- It is observed that the extension-twist and bending-shear modes can be considered to be decoupled, i.e., in the cases of imposed ϵ $(= \nu_3 - 1)$ and κ_3, the induced $\nu_\alpha, \kappa_\alpha$ $(\alpha = 1, 2)$ are observed to be negligible. Similarly, in

the case of imposed ν_α and κ_α ($\alpha = 1, 2$), the induced ϵ and κ_3 are observed to be negligible. This results in decoupling the fitting procedure into two separate problems – one of fitting the coefficients B, D, E corresponding to the extension-twist simulations, and the other of coefficients A, C, F corresponding to the bending-shear simulations. Further, it is observed that the extracted strain measures $\epsilon, \kappa_3, \nu_1$, and ν_2 are uniform over the length of the SWNT whenever each of them is imposed, while κ_1, κ_2 always vary over the length (this is expected from the bending profile imposed, as explained in Section 5.4).

- In order to minimize numerical scatter in the fitting data, the following steps are carried out:
  - All the atomic coordinates are normalized by the undeformed maximum axial coordinate, $Z_{max} \approx L$ (length of the unit cell), with the origin of coordinates located on the centerline on one end of the SWNT unit cell. Hence, the axial coordinates run from $s \equiv \frac{Z}{Z_{max}} = 0 \longrightarrow 1$.
  - In the imposed extension and twist simulations, ν_3 and κ_3, between $s = 0 \longrightarrow 0.2$, are replaced by a straight line connecting the values of ν_3 and κ_3 at $s = 0.2$ to their values at $s = 0$ which, in turn, are assumed to be the average of their values over the region $s = 0.2 \longrightarrow 1$.
- In the imposed bending and shear simulations, κ_1 is observed to be negligible when κ_2 or ν_1 are imposed, while κ_2 is observed to be negligible when κ_1 or ν_2 are imposed.
- Computing derivatives of the centroidal position vector to find $\nu_\alpha, \kappa_\alpha$ ($\alpha = 1, 2$): Since the locus of centroidal positions obtained during the simulations can be non-smooth, a smooth quartic polynomial (found to

be sufficient in terms of degree, as well as consistent with the imposed bending profile (Section 5.4)) is fit through the centroidal points and the derivatives computed in closed-form. Such an approach avoids the use numerical derivatives which can be unreliable when employed for non-smooth functions. Further, atoms with $s < 0.2$ and $s > 0.85$ are neglected, with $\nu_\alpha, \kappa_\alpha$ ($\alpha = 1, 2$) over those regions replaced with straight lines in a procedure identical to the case of imposed extension and twist.

- Finally, considering the bending-shear fitting problem

$$W = \frac{1}{2}[A\kappa_\alpha\kappa_\alpha + C\nu_\alpha\nu_\alpha + 2F\nu_\alpha\kappa_\alpha] \quad , \tag{5.26}$$

it is found necessary to neglect the $C\nu_\alpha\nu_\alpha$ term when κ_1 or κ_2 are imposed in order to obtain a fit. However, it is found not to be necessary to neglect the $A\kappa_\alpha\kappa_\alpha$ term when ν_1 or ν_2 are imposed. Numerical results are provided with both keeping (indicated by '2' in Figures 5.11) and dropping (indicated by '1' in Figures 5.11) the $A\kappa_\alpha\kappa_\alpha$ term when ν_1 or ν_2 are imposed, and are observed to be only slightly different. This indicates that the induced shear during imposed bending is much more significant than the induced curvature during imposed shear.

- For the primary 'moduli', A, B, C, D, a comparison between the corresponding values obtained from an isolated deformation mode fit (indicated by 'bend-only fit', 'twist-only fit', 'shear-only fit', and 'extension-only fit' respectively for A, B, C, D in Figures 5.10 and 5.11), and the coupled deformation mode fit gives an indication of the amount of strain energy distributed in the induced terms. For example, in the case of the twist modulus, the value of B obtained from fitting $W = \frac{1}{2}B{\kappa_3}^2$ (imposed twist alone) is compared with the value of B obtained from fitting

$$W = \frac{1}{2}[B{\kappa_3}^2 + D\epsilon^2 + 2E\epsilon\kappa_3] \tag{5.27}$$

Table 5.1: Small-strain elastic moduli in extension, twist, bending, and shear of a $(9, 6)$ SWNT. Converted bulk quantities (Appendix D), with units specified in square braces, and corresponding one-dimensional quantities in parantheses (fit using strain energies in Hartrees and strains extracted with atomic coordinates normalized by Z_{max} – Section 5.5 – and hence have units of Hartrees).

B_R [aJ.nm] (A)	G [GPa] (B)	S [GPa] (C)	Y [GPa] (D)
2.43 (0.30)	420 (15.36)	409 (187.10)	1081 (494.51)

corresponding to coupled extension and twist. Since the induced effects are expected to be small, the parameter values obtained from both cases are expected to be comparable.

5.5.1 Small-strain elastic moduli

Table 5.5.1 summarizes the linearized (small-strain) elastic moduli in extension, twist, bending, and shear deformations of a $(9, 6)$ SWNT. These are considered to be useful in performing small-strain simulations involving these primary deformation modes. The small-strain elastic moduli in extension and twist have also been reported in Chapter 4 (Section 4.4) using different approaches, and compared to several values in the literature. A more detailed study of nonlinear behavior such as variations of the elastic moduli with deformation regimes, as well as aspects of coupling between deformation modes, is contained in Figures 5.10 and 5.11 with related discussions in Sections 5.5.2 and 5.5.3 respectively.

In Table 5.5.1, B_R, G, S, and Y are, respectively, the bending rigidity, twist modulus, shear modulus, and Young's modulus. It is observed that B_R is of the

order of 1.68% of the bending rigidity obtained from using a Bernoulli-Euler beam theory (i.e., Young's modulus (Y) $\times$ cross-sectional bending moment of inertia (I), YI, [28]) indicating a string-like behavior of the SWNT under consideration, with low bending rigidity. This aspect of SWNTs has also been studied and reported by [75, 87]. The twist and shear moduli (G and S respectively) are close to each other and around 38% of Y. Further, it is observed that the Young's modulus (Y) agrees with most reported values in the literature (that also assume an artificial wall thickness of 3.35 Å) (for example, Chapter 4 in the present dissertation [14] contains a list of reported values from the literature on SWNT Young's moduli).

5.5.2 Coupled extension-twist deformations

Figure 5.9 displays kinematic coupling results from the extension-twist simulations. Figure 5.9(a) shows the induced angle of twist under imposed extension as a function of the axial coordinate for some representative deformation steps. It is observed that successive planes of atoms rotate by equal and opposite angles. While this non-smooth kinematic behavior is different from the smooth kinematic behavior observed in [12] (Figures 7(b,d), 8(b,d), 9(b,c,d)), Chapter 3 – Figures 3.2(b,d) ([13] – Figures 6(b,d)), it is noted that the periodicity of the two-dimensional honeycomb lattice of graphene is explicitly imposed in Chapters 2, 3, and 4 [12, 13] leading to restricted deformation patterns while no such restrictions are imposed in the present case. Figure 5.9(b) shows the induced axial strain under two equal and opposite imposed twists. In this case, it is observed that the induced axial strains are equal (excluding some scatter at the ends of the cell) for both senses of imposed twist. This is also observed in [12]

(Figures 7(d), 8(d), 9(b,c,d) – in the neighborhood of the origin) and in Chapter 3 – Figure 3.2(b) ([13] – Figure 6(b)), where the coupled extension-twist problem is addressed using a completely independent approach – the Tersoff-Brenner [8, 86] interatomic potential within a quasicontinuum membrane framework. This observation can be used to show that the quadratic extension-twist coupling coefficient should vanish (or the contribution from the $2E\epsilon\kappa_3$ term in Equation 5.20 should be vanishingly small) as follows. Equation 5.20 can be used in Equations 5.12 to get

$$n_3 = D\epsilon + E\kappa_3 \tag{5.28}$$

and

$$m_3 = B\kappa_3 + E\epsilon \quad . \tag{5.29}$$

In the case of imposed twist, since the axial strain is admitted, $n_3 = 0$, and, from Equation 5.28,

$$\epsilon = -\frac{E}{D}\kappa_3 \quad . \tag{5.30}$$

Now, it is straightforward to show that if (ϵ_1, ϵ_2) are the induced axial strains corresponding to equal and opposite imposed twists of $(\kappa_3, -\kappa_3)$, and $\epsilon_1 = \epsilon_2$ (as in Figure 5.9(b), [12](Figures 7(d), 8(d), 9(b,c,d)), and Chapter 3 – Figure 3.2(b) ([13] – Figure 6(b))), then, from Equation 5.30, the coupling coefficient $E = 0$.

Alternatively, from [12](Figures 7(d), 8(d), 9(b,c,d)), and Chapter 3 – Figure 3.2(b) ([13] – Figure 6(b)), it is observed that $\frac{\partial \epsilon}{\partial \kappa_3} \mid_{\kappa_3=0} = 0$. This can also be

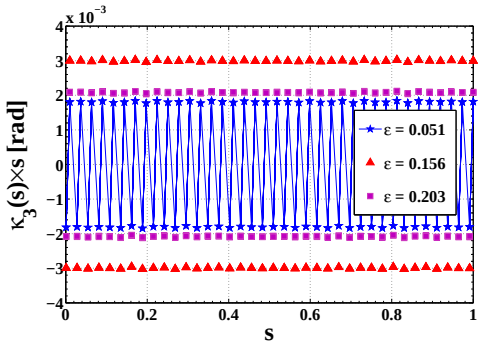

(a) Induced twist (angle of twist in radians) during imposed extension (ϵ)

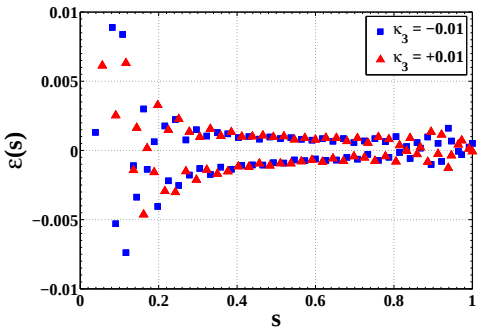

(b) Induced extension ($\epsilon(s)$) during imposed twist (κ_3 in rad/Å)

Figure 5.9: Coupled extension-twist results from representative deformation steps.

used with Equation 5.30 to show that $E = 0$. Further, it is easy to show, from Equations 5.28 and 5.29, that when $E \neq 0$ in Equation 5.20, a rod with $E > 0$ will contract ($\epsilon < 0$) when $\kappa_3 > 0$ (termed as a 'right-handed' rod [38]) while a rod with $E < 0$ will extend ($\epsilon > 0$) when $\kappa_3 > 0$ (termed as a 'left-handed' rod [38]). From the observations in the present work, as well as Chapter 3 – Figures 3.2 [12, 13], it can be concluded that the extension-twist coupling for the SWNT under consideration should be at least cubic or higher, and is negligible at quadratic order.

Figures 5.10 show the results from fitting the parameters B, D, E to the extension and twist atomistic simulations over a range of deformation magnitudes corresponding to each imposed mode. Details of the procedure used to obtain the curves in Figures 5.10 are given in Appendix C, while conversions from the one-dimensional primary moduli, B and D in this case, to more physically appealing bulk quantities (twist modulus G corresponding to B, and Young's modulus Y corresponding to D) are outlined in Appendix D. It is expected that there be some variation in the resulting values of the parameters over the deformation ranges because of the same quadratic model (Equation 5.20) being fit

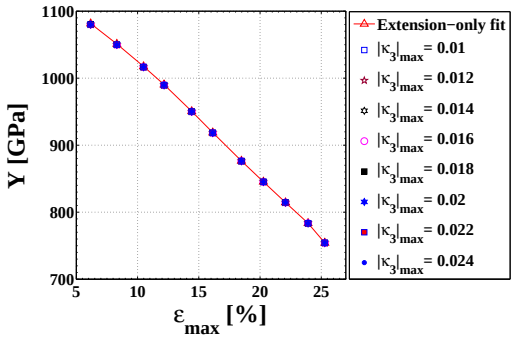

(a) Young's modulus (Y)

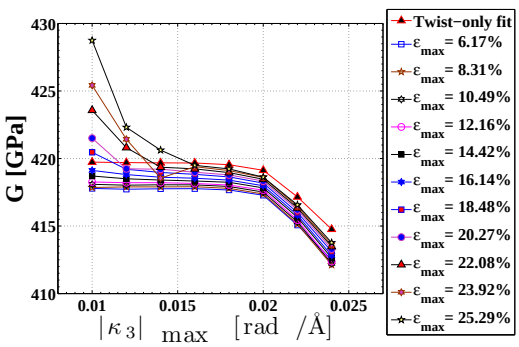

(b) Twist modulus (G)

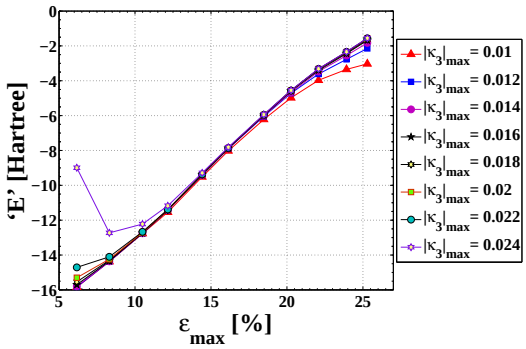

(c) Extension-twist coupling coefficient (E)

Figure 5.10: Fitting results for elastic moduli in extension and twist deformation modes corresponding to different ranges of imposed extension (axial strain %) and imposed twist (angle of twist per unit undeformed length in rad/Å).

to atomistic simulations over increasing amounts of imposed strain. As pointed out in [6, 31, 93], as well as evident from Figures 5.10, the elastic properties of the SWNT are nonlinear and strain-dependent. Hence, the quadratic rod parameters depend on the range of deformation over which they are fit.

Further, it is observed that, although non-zero fit values are obtained for E in Figure 5.10(c), the contribution of the extension-twist coupling term to the total strain energy in imposed extension or twist (Equation 5.27) is negligible – as will be elaborated subsequently in Appendix E. As stated in Section 5.5.1, it is observed that the values of the Young's modulus obtained in Figure 5.10(a)

agree with most reported values in the literature (that also assume an artificial wall thickness of 3.35 Å) (for example, Chapter 4 in the present dissertation [14] contains a list of reported values from the literature on SWNT Young's moduli). As described in Section 5.5.1, Table 5.5.1 summarizes the primary elastic moduli in extension and twist useful in small-strain simulations.

5.5.3 Coupled bending-shear deformations

Figures 5.11 show the results from fitting the parameters A, C, F to the bending and shear atomistic simulations over a range of deformation magnitudes corresponding to each imposed mode. Details of the procedure used to obtain the curves in Figures 5.11 are given in Appendix C, while conversions from the one-dimensional primary moduli, A and C in this case, to more physically appealing bulk quantities (bending rigidity B_R corresponding to A, and shear modulus S corresponding to C) are outlined in Appendix D.

As in the case of extension-twist deformations (Section 5.5.2), some variations of the resulting parameter values are observed over the deformation ranges. As pointed out in Section 5.5.2, as well as evident from Figures 5.11, the elastic properties of the SWNT are nonlinear and strain-dependent. Hence, the quadratic rod parameters depend on the range of deformation over which they are fit.

As mentioned in Section 5.5.1, an interesting aspect of the SWNT under consideration emerges from comparing the bending modulus obtained from the bending simulations (Figure 5.11(a)) to one obtained from using a Bernoulli-Euler beam theory (i.e., Young's modulus (Y) $\times$ cross-sectional bending moment

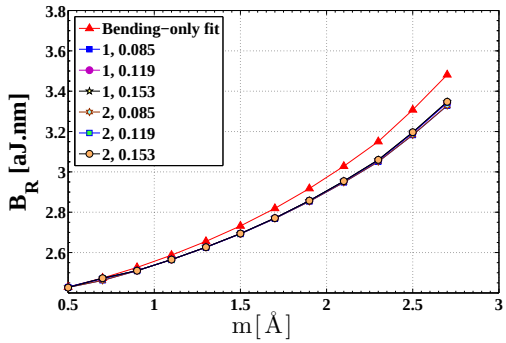

(a) Bending rigidity (B_R): Compare with YI = 144.9 aJ.nm for Y = 1 TPa

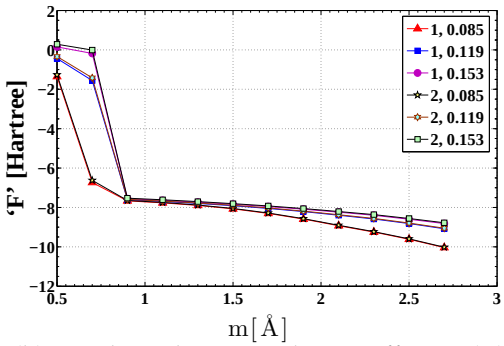

(b) Bending-shear coupling coefficient (F)

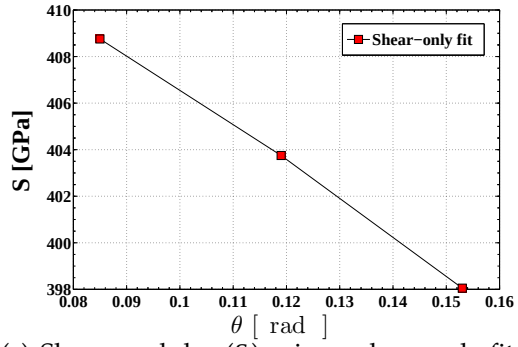

(c) Shear modulus (S) using a shear-only fit

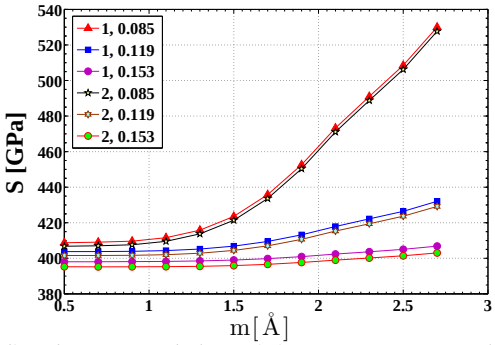

(d) Shear modulus (S) using a coupled bending-shear fit

Figure 5.11: Fitting results for elastic moduli in bending and shear deformation modes corresponding to different ranges of imposed curvatures (reflected in the mid point deflections (m in Å – Figure 5.8)), and shear deformations (angles of rotation of cross-sections about in-plane axes (θ in radians – Figure 5.8)). In the legends, for example, '2, 0.085' indicates keeping and '1, 0.085' indicates dropping the $A\kappa_\alpha\kappa_\alpha$ term when ν_1 or ν_2 are imposed (of magnitude indicated by θ = 0.085 rad – Figure 5.8) – Equation 5.26 and Section 5.5.

of inertia (I), YI, [28]). It is observed that the obtained bending rigidities are much lower than predictions from a Bernoulli-Euler beam theory thus indicating that the SWNT under consideration behaves more like a string, with low bending rigidity, than a beam. This aspect of SWNTs has also been reported by [75, 87] in which the frequency dependence of suspended SWNT oscillators is studied and the behavior classified based on the amount of slack (defined as

the ratio of the excess length of the SWNT to the distance between clamping points) and the transverse force. Further, in the present work, it is observed that identical shear and bending moduli are obtained for deformations in the $1-3$ and $2-3$ planes thus providing an *a posteriori* justification for the applicability of the hemitropic + flip symmetric rod model with Equation 5.20 to the present case. Although there appears to be no straightforward interpretation of the bending-shear coupling coefficient (F) in a manner analogous to the extension-twist coupling coefficient (E) (Section 5.5.2), it is observed (as will be elaborated subsequently in Appendix E) that the energetic contribution of the bending-shear coupling term to the total strain energy in imposed bending or shear deformations (Equation 5.26) is relatively small compared to the primary bending or shearing strain energies respectively. As described in Section 5.5.1, Table 5.5.1 summarizes the primary elastic moduli in bending and shear useful in small-strain simulations.

5.6 Concluding remarks

An approach to model SWNTs is presented in this chapter using a one-dimensional, nonlinearly elastic rod theory that suitably exploits certain symmetries in the underlying atomic structure. While prior work on coupling of deformation modes in SWNTs has focused on extension and twist alone [12, 13], the present model captures extension, twist, bending, and shear deformation modes including extension-twist and bending-shear coupling.

5.6.1 Summary of findings

The material properties for an SWNT are contained in the elastic parameters of the strain energy density function, which are computed by performing atomistic simulations over a range of deformation magnitudes (Figures 5.10 and 5.11). As pointed out in Sections 5.5.2 and 5.5.3, as well as evident from Figures 5.10 and 5.11, the elastic properties of the SWNT are nonlinear and strain-dependent. Hence, the quadratic rod parameters depend on the range of deformation over which they are fit.

With regard to the primary moduli in extension, twist, bending, and shear deformation modes, it is observed that values of the Young's modulus (Y) (over the specified deformation ranges) agree with most reported values in the literature (Sections 5.5.1 and 5.5.2). The twist and shear moduli (G and S respectively) are close to each other and around 35 – 40% of Y (Sections 5.5.1, 5.5.2, and 5.5.3). The bending rigidity (B_R) is found to be of the order of 1.65 – 2.30% of the bending rigidity obtained from using a Bernoulli-Euler beam theory (Sections 5.5.1 and 5.5.3) indicating a string-like behavior of the SWNT under consideration, with low bending rigidity. With regard to the extension-twist and bending-shear coupling terms, it is argued that the extension-twist coupling be negligible at quadratic order of the strain energy density (Section 5.5.2 and Appendix E), and the contribution of the bending-shear coupling term to the total strain energy in bending or shear be relatively small (Section 5.5.3 and Appendix E). Table 5.5.1 summarizes the primary elastic moduli in extension, twist, bending, and shear useful in small-strain simulations.

The results (for example, of the bending rigidity) indicate benefits of accounting for important anisotropic and large-strain effects as improvements

over employing traditional, linearly elastic, isotropic, small-strain, continuum models to SWNTs. It is envisioned that these material properties can serve as useful inputs to existing nonlinearly elastic continuum rod simulation tools capable of studying complex deformation patterns that could be applicable to SWNTs (for example, in studying oscillations of suspended SWNTs [75, 87], or deformations of nanocomposites).

5.6.2 Future work

The following lines of future study are proposed.

- One of the topics of interest is to study the variations of the elastic material parameters with chirality of SWNTs. For example, it is known that the extensional modulus depends weakly on the SWNT chirality (for example, Chapter 4 [14]). Some of the other publications that characterize the variations in certain elastic properties with chirality and diameter of SWNTs are [6, 15, 31, 39, 51, 93]. But it is of interest to perform a similar study on all of the other moduli – both by keeping the diameter of the SWNT fixed and varying the configuration (chiral, armchair, or zigzag), as well as holding the configuration fixed and varying the diameter. Such a study can enable a rigorous quantification of the transferability of computed parameter values in this work (using the $(9, 6)$ SWNT) to other SWNTs.
- The bending properties have been evaluated by imposing a particular bent profile (Section 5.4) and it is of interest to inspect if these properties change upon changing the imposed bent profile. An additional source of inconsistency arises from the imposed twist simulations being performed on

a finite SWNT (without periodic boundary conditions) that make them somewhat different from the remaining deformation modes. Future efforts could address such aspects of the present study.

- One of the key assumptions in the rod model employed in this work is that of rigid cross-sections (Section 5.2). This assumption neglects effects such as the Poisson's effect [28] (change in the cross-sectional dimensions due to axial strain) which can be especially important for thin-walled hollow tubes and systems that are single-atomic layer thick such as SWNTs. A natural approach to follow is to use a shell or a membrane theory (as has already been carried out, for example, in Chapters 2, 3, and 4 [2, 3, 12, 13, 14, 44, 52, 101]). But such an approach loses the reduced dimensionality advantage that the rod model holds over the shell or membrane model. [34] present an approach to take into account cross-sectional deformations by adding the cross-sectional strain energy as an additional term to the total strain energy of the rod. However, this approach still fails to capture the Poisson's effect since it decouples the axial and cross-sectional deformations. Moreover, the model by [34] assumes a linearly elastic, isotropic, Kirchhoff-like constitutive model [34] that is devoid of the coupling between different deformation modes as has been studied in the present work.

- Based on some preliminary work (details in Appendix F), a key idea to account for cross-sectional deformations in the rod model is to relax the orthonormality constraint imposed on directors in the restricted theory (Section 5.2) to obtain a more general rod model. This enables capturing cross-sectional shear deformations through the change in angle between directors, and change in cross-sectional thickness using magnitudes of the di-

rectors. These additional strain measures characterize cross-sectional deformations. It is noted that the restricted theory described in Section 5.2 is immediately realized as a special case of the general formulation when the directors are defined to be mutually orthonormal (Equation 5.2). Within the nonlinearly elastic material assumption, the next steps are to derive strain energy density representations for this general rod model, similar to published work on the special rod model [38]. This general rod model will, then, enable a unified treatment of extension, twist, bending, shear, coupled modes, and in-plane cross-sectional deformations. This is expected to be a significant step in improving the applicability of a rod model to hollow structures such as SWNTs and biomolecules such as DNA. The only neglected effect in comparison to a three-dimensional approach will be that of warping (out-of-plane deformations) of cross-sections, which is not expected to be significant for slender structures such as SWNTs and DNA. Application of this improved rod model to SWNTs will require fitting additional coefficients (that arise in this model due to cross-sectional deformations) although the data generated from atomistic simulations already carried out in the present work can be used to estimate these additional coefficients.

The following chapter presents some conclusions, including directions for future work.

CHAPTER 6

CONCLUSIONS AND FUTURE WORK

The following remarks are in order in concluding the present dissertation.

- This dissertation is primarily motivated by the need to incorporate atomistic details into continuum mechanical models in order to build accurate yet computationally tractable methods capable of simulating large atomic systems (Chapter 1). An SWNT is the atomic system of interest in the present dissertation.
- The dissertation deals with two atomistic-continuum models to study mechanical deformations of SWNTs – (i) a two-dimensional, quasicontinuum membrane model (Chapters 2, 3, and 4), and (ii) a one-dimensional rod model (Chapter 5).
- The two-dimensional, quasicontinuum SWNT model (Chapter 2) has been employed in prior, published work [2, 3, 12, 13, 14, 44, 52, 101]. The key contributions of the present dissertation are in modifying the atomistic-continuum kinematic hypothesis – the CB rule – to deal with inhomogeneous deformations, to account for the energetic differences between a planar graphene sheet and a cylindrical SWNT by considering a cylindrical reference configuration, investigating coupled extension and twist deformations in SWNTs (Chapter 3), and accounting for this coupling behavior in determining elastic moduli and stress-strain curves in extension and twist deformations (Chapter 4).
- The one-dimensional SWNT rod model (Chapter 5) is an improvement over linearly elastic, isotropic, small-strain, one-dimensional SWNT models. It contains the capability to model material as well as geometric non-

linearity, and anisotropic effects that arise in large-strain regimes. In a unified framework, it captures extension, twist, bending, and shear deformation modes including extension-twist and bending-shear coupling.

- It is envisioned that the material properties derived in the rod model can serve as useful inputs to existing nonlinearly elastic continuum rod simulation tools (based, for example, on the finite element method) capable of studying complex deformation patterns that could be applicable to SWNTs (for example, in studying oscillations of suspended SWNTs [75, 87], or deformations of nanocomposites).
- The deformable cross-section atomistic-continuum rod model (Section 5.6.2 and Appendix F) is proposed as a future line of study that relaxes the constraint of rigid cross-sections in the present rod model, thereby improving the applicability of the rod model to hollow structures such as SWNTs, and biomolecules such as DNA.
- It is also envisioned that the ideas presented in this dissertation can be extended to other atomic systems such as silicon [76] or boron nitride [32] nanotubes by use of appropriate lattices and energetic descriptions.

APPENDIX A

CAUCHY-BORN RULE FOR INHOMOGENEOUS DEFORMATIONS

Let x_i and x_j denote points on a curve parameterized by s, with curvilinear coordinates s_i and s_j respectively. Let x_m denote the mid point between x_i and x_j, and s_m denote its curvilinear coordinate. Then, for an arbitrary function $\phi(x)$ (assumed to be sufficiently smooth and differentiable in $[x_i, x_j]$) defined on the curve, and $\xi_1 \in [x_i, x_m]$, $\xi_2 \in [x_m, x_j]$,

$$\phi(x_i) = \phi(x_m) + (s_i - s_m)\phi_{,s}(x_m) + \frac{1}{2!}(s_i - s_m)^2\phi_{,ss}(\xi_1) \quad , \tag{A.1}$$

and

$$\phi(x_j) = \phi(x_m) + (s_j - s_m)\phi_{,s}(x_m) + \frac{1}{2!}(s_j - s_m)^2\phi_{,ss}(\xi_2) \quad , \tag{A.2}$$

where $,s$ denotes a derivative with respect to s. Now, if ϕ is assumed to be quadratic, $\phi_{,ss}(\xi_1) = \phi_{,ss}(\xi_2)$. Using this, along with the fact that x_m is the mid point, and subtracting Equation A.1 from Equation A.2 gives

$$\phi(x_j) - \phi(x_i) = \phi_{,s}(x_m)(s_j - s_i) \tag{A.3}$$

which amounts to Equation 3.32 for a quadratic f evaluated using the 'mid point rule'. Further, if ϕ is of any higher degree (than quadratic), Equation 3.32 can be readily employed to obtain a location $x_{exact} \in [x_i, x_j]$ at which

$$\phi(x_j) - \phi(x_i) = \phi_{,s}(x_{exact})(s_j - s_i) \quad . \tag{A.4}$$

APPENDIX B

COMPUTATION OF THE NUMBER OF HELICES IN AN SWNT

This section presents formulas for the number of helices in the rod model (Section 5.3.4) in terms of the chirality of SWNTs (Figures B.1, B.2 and B.3). In terms of the carbon-carbon bond length in graphene, a, and the SWNT chiral indices, (n, m), the circumference of the rolled-up SWNT can be expressed [20, 70, 92] as

$$C = \sqrt{3}a\sqrt{n^2 + m^2 + nm} \quad , \tag{B.1}$$

and the chiral angle, θ, is given by

$$\theta = \arctan\frac{\sqrt{3}m}{m + 2n} \quad . \tag{B.2}$$

The orientation of the helices with respect to the circumferential direction (Figure B.1) is

$$\phi = \frac{\pi}{3} + \theta \quad . \tag{B.3}$$

If the number of helices (each of width $a/2$ and parallel to each other with spacing a) is h, the following relation can be written (from Figure B.1(b)):

$$\frac{\sqrt{3}a}{2\sin\phi}h = C = \sqrt{3}a\sqrt{n^2 + m^2 + nm} \quad , \tag{B.4}$$

from which $h = m + n$. As special cases, an armchair SWNT (Figure B.2) has $m = n$ which gives $h_{armchair} = 2n$, and a zigzag SWNT (Figure B.3) has $m = 0$ which gives $h_{zigzag} = n$.

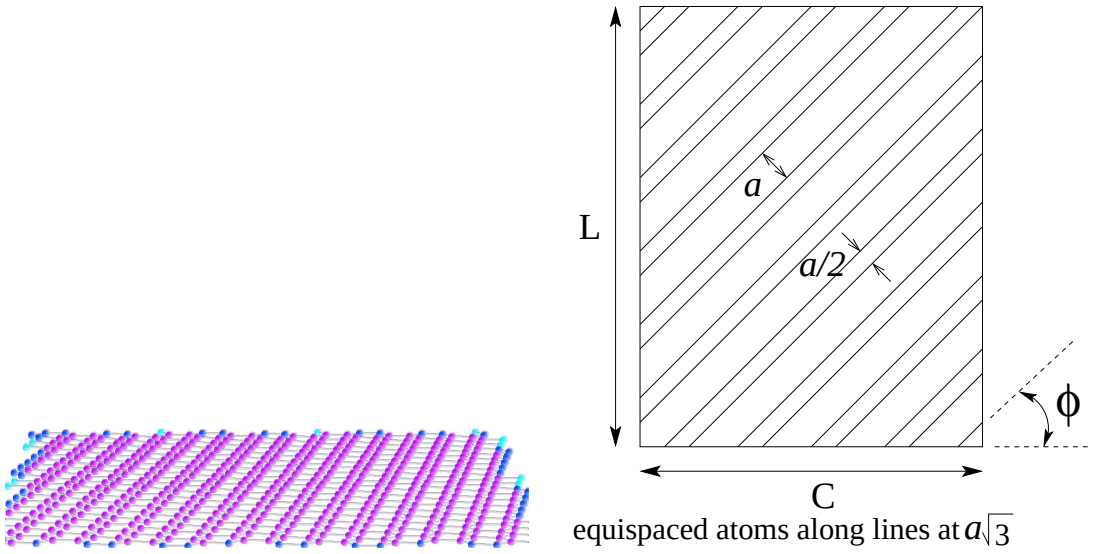

(a) Atomic structure in the planar configuration

(b) Helices at an orientation of ϕ from the circumferential direction

Figure B.1: Helical idealization of a chiral SWNT.

According to the kinematic extension-twist coupling results from Chapter 3 and [30, 31, 51], it is observed that armchair and zigzag SWNTs do not exhibit any induced twist during imposed extension. In terms of the proposed helical idealization, this observation can be interpreted as follows. In the case of armchair SWNTs, helices can be formed at 30°, 90°, and 150° (Figure B.2(b) shows helices corresponding to the 90° orientation alone) from the circumferential direction (the 60° orientational spacing between successive possible helices, which applies to all SWNT configurations, arises from the 60° rotational symmetry of the underlying hexagonal lattice). Similarly, in the case of zigzag SWNTs, helices can be formed at 60° and 120° from the circumferential direction (Figure B.3(b) shows helices corresponding to the 60° orientation).

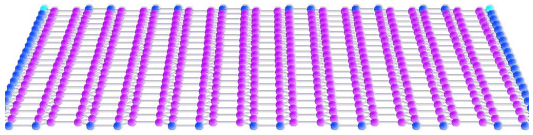

(a) Atomic structure in the planar configuration

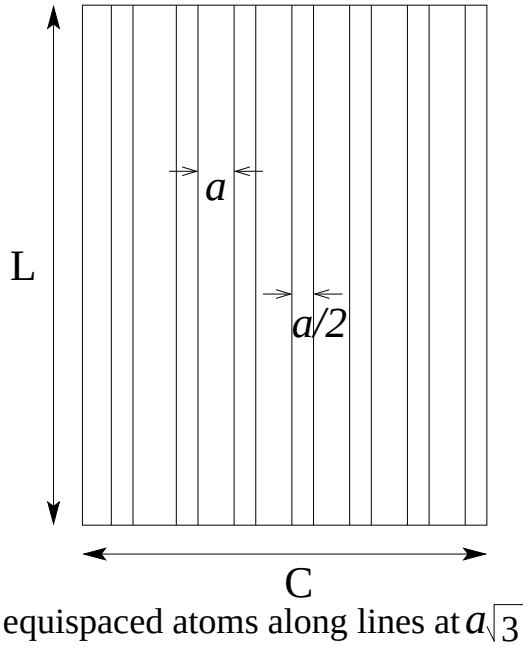

(b) Helices at an orientation of 90° from the circumferential direction

Figure B.2: Helical idealization of an armchair SWNT.

Further, it is noted, from symmetry, that helices at orientations of $90° \pm \omega$ ($0° \leq \omega \leq 90°$) induce an equal and opposite handedness to the rod. Hence, it follows that there is no net handedness in the case of armchair and zigzag SWNTs (leading to zero induced twist during imposed extension – Chapter 3 and [30, 31, 51]), while chiral SWNTs retain a net handedness that induces twist during imposed extension (Chapter 3 and [30, 31, 51]).

Further, consideration of the number of atoms along the SWNT circumferential direction (circumference C is fixed once the chiral indices are chosen), and along the helices, provides the necessary motivation to consider the helices as continua. The following formulas are given for chiral SWNTs with chiral indices (n, m) and the corresponding expressions for armchair and zigzag SWNTs follow immediately upon setting $n = m$ and $m = 0$ respectively. From Figure B.1,

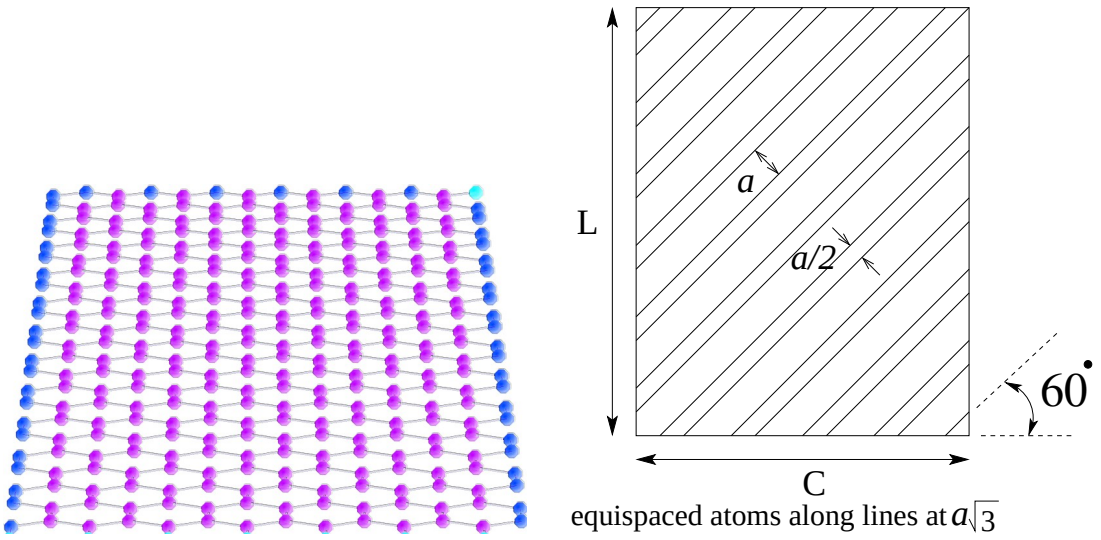

(a) Atomic structure in the planar configuration

(b) Helices at an orientation of 60° from the circumferential direction

Figure B.3: Helical idealization of a zigzag SWNT.

the number of atoms in the circumferential direction, ${n_{atoms}}^{(C)}$, is given by

$$ {n_{atoms}}^{(C)} = 2h = 2(m+n) \quad , \tag{B.5} $$

while the number of atoms along the helices, ${n_{atoms}}^{(L)}$, is given by

$$ {n_{atoms}}^{(L)} = \frac{L}{a\sqrt{3}\sin\phi} \quad , \tag{B.6} $$

where L is the SWNT length. Upon using Equations B.2 and B.3, Equation B.6 can be rewritten as

$$ {n_{atoms}}^{(L)} = \frac{2L}{3a}\frac{\sqrt{m^2+n^2+nm}}{m+n} \quad . \tag{B.7} $$

Since, typically, $L \gg a$ for long SWNTs (continuum limit), it follows that ${n_{atoms}}^{(L)} \gg {n_{atoms}}^{(C)}$ and hence the helices may be considered as continua in comparison to the circumferential direction.

APPENDIX C

DETERMINATION OF ROD PARAMETERS OVER DIFFERENT RANGES OF DEFORMATIONS

As pointed out in Sections 5.5.2 and 5.5.3, as well as evident from Figures 5.10 and 5.11, the elastic properties of the SWNT are nonlinear and strain-dependent. Hence, the quadratic rod parameters depend on the range of deformation over which they are fit. As an example, one of the curves in Figures 5.10(a,b,c) can be considered. Each point on this curve corresponds to a specific value of $|\kappa_3|_{max}$ and ϵ_{max}. Such a point in obtained as follows.

First, $|\kappa_3|_{max}$ is imposed in increments $\kappa^{(i)} : \kappa^{(1)}, \kappa^{(2)}, \kappa^{(3)}, \ldots, \kappa^{(n)}$, where n is the number of imposed twist simulations taken to reach $|\kappa_3|_{max}$. It is noted that $\kappa^{(i)}$ denotes the *imposed* angle of twist per unit undeformed length, which gives rise to an *induced* axial strain $\epsilon^{(i)}$. If $W^{(i)}$ denotes the strain energy density of the corresponding deformed state, from Sections 5.4 and 5.5, and Equation 5.27,

$$W^{(i)} = \frac{1}{2}[B{\kappa^{(i)}}^2 + D{\epsilon^{(i)}}^2 + 2E\epsilon^{(i)}\kappa^{(i)}]; \quad i = 1, 2, 3, \ldots, n \quad . \tag{C.1}$$

Next, ϵ_{max} is imposed in increments $\epsilon^{(j)} : \epsilon^{(1)}, \epsilon^{(2)}, \epsilon^{(3)}, \ldots, \epsilon^{(m)}$, where m is the number of imposed extension simulations taken to reach ϵ_{max}, and m equations analogous to Equation C.1 are written in terms of the *imposed* axial strain, $\epsilon^{(j)}$, and the *induced* angle of twist per unit undeformed length, $\kappa^{(j)}$.

These $n + m$ equations are used together in a least-squares fitting procedure (as outlined in Section 5.4) to obtain the values of the coefficients D, B, and E for this pair $(|\kappa_3|_{max}, \epsilon_{max})$. Finally, the Young's modulus (Y) and the twist modulus (G) are obtained, corresponding to coefficients D and B respectively, as

described subsequently in Appendix D. Figures 5.11, corresponding to coupled bending-shear deformations, are obtained in an analogous manner using Equation 5.26.

APPENDIX D

CONVERSION OF MATERIAL PROPERTIES FROM ROD PARAMETERS TO BULK QUANTITIES

This section presents the conversions from raw parameter values obtained by data fitting in the quadratic strain energy – Equation 5.20 – to bulk quantities assuming that the rod is of undeformed length, L, has a thin-walled circular cross-section of undeformed radius, R, wall thickness, t, and is subject to small enough deformations with constant strain states that can be adequately described by classical small-strain models [28]. These conversions are also employed in certain cases of large deformations (Figures 5.10 and 5.11 contain the ranges of deformation in each mode) during which it is noted that their applicability is only approximate. It is also noted that the cross-sectional assumptions are only required as a means to convert the rod material parameters to bulk quantities. As mentioned earlier (Section 5.1), the present rod model does not require any information on the cross-section and treats the continuum as a one-dimensional curve.

D.1 Extensional modulus

For a bulk cylinder subject to tension or compression, the strain energy per unit volume is given by $\frac{1}{2}Y\epsilon^2$ [28], where Y is the Young's modulus and ϵ is a constant axial strain. Hence, the total strain energy stored is given by $\frac{1}{2}Y(2\pi RtL)\epsilon^2$. From the parameter fitting in the rod model (Equation 5.20) with normalized coordinates, the total strain energy stored in an extension-only mode with the same constant axial strain, ϵ, is $\frac{1}{2}D\epsilon^2$ (since the length becomes unity upon normalization). Equating the strain energies in the bulk cylinder and the rod model

gives the relation between the rod parameter, D, and the bulk Young's modulus, Y, to be $Y = \frac{D}{2\pi RtL}$.

D.2 Twist modulus

For a bulk cylinder subject to Saint Venant torsion, the strain energy per unit volume is given by $\frac{1}{2}G{\kappa_3}^2R^2$ [28], where G is the twist modulus and κ_3 is a constant angle of twist per unit undeformed length of the cylinder. Hence, the total strain energy stored is given by $\frac{1}{2}G{\kappa_3}^2R^2(2\pi RtL)$. From the parameter fitting in the rod model (Equation 5.20) with normalized coordinates, the total strain energy stored in a twist-only mode with the same constant angle of twist per unit undeformed length is $\frac{1}{2}B{\kappa_{3norm}}^2$, where $\kappa_{3norm} = \kappa_3 Z_{max}$ is the angle of twist per unit undeformed length in normalized coordinates. Equating the strain energies in the bulk cylinder and the rod model with the assumption that $Z_{max} \approx L$ gives the relation between the rod parameter, B, and the bulk twist modulus, G, to be $G = \frac{BZ_{max}}{2\pi R^3 t}$.

D.3 Bending modulus

For a bulk cylinder modeled as a Bernoulli-Euler beam subject to bending, the total strain energy stored is given by [28] $\frac{1}{2}B_R{\kappa_{bend}}^2L$, where B_R is the bending rigidity (for an isotropic Bernoulli-Euler beam, $B_R = YI$, where Y is the Young's modulus of the material and I is the cross-sectional bending moment of inertia [28]), and κ_{bend} is a constant bending curvature. From the parameter fitting in the rod model (Equation 5.20) with normalized coordinates, the total strain energy

stored in a bend-only mode with the same constant bending curvature is (noting that when κ_1 is imposed, κ_2 is assumed to be zero, and when κ_2 is imposed, κ_1 is assumed to be zero) $\frac{1}{2}A{\kappa_{bendnorm}}^2$, where $\kappa_{bendnorm} = \kappa_{bend}Z_{max}$ is the bending curvature in normalized coordinates. Equating the strain energies in the bulk cylinder and the rod model with the assumption that $Z_{max} \approx L$ gives the relation between the rod parameter, A, and the bulk bending rigidity, B_R, to be $B_R = AZ_{max}$.

D.4 Shear modulus

The conversion from the rod parameter, C, to the shear modulus closely follows Appendix D.1. For a bulk cylinder subject to shear, the strain energy per unit volume can be expressed as $S\nu^2$, where S is the shear modulus and ν is a constant shear strain. Hence, the total strain energy stored is given by $S(2\pi RtL)\nu^2$. From the parameter fitting in the rod model (Equation 5.20) with normalized coordinates, the total strain energy stored in shear-only modes with the same constant shear strain, ν, is (noting that both ν_1 and ν_2 are allowed to be non-zero when either of them, or κ_1 or κ_2 are imposed) $C\nu^2$ (since the length becomes unity upon normalization). Equating the strain energies in the bulk cylinder and the rod model gives the relation between the rod parameter, C, and the bulk shear modulus, S, to be $S = \frac{C}{2\pi RtL}$.

APPENDIX E

STRAIN ENERGY PROPORTIONS

Figures E.1, E.2, and E.3 show the percentage contributions of the extension, twist, and coupled extension-twist terms in Equation 5.20 at the points of maximum imposed $\epsilon, +\kappa_3, -\kappa_3$ respectively (corresponding to the same deformation ranges as presented in Figures 5.10).

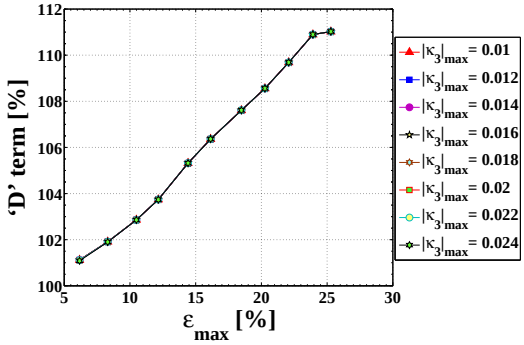

(a) Percentage of strain energy from the 'D' term

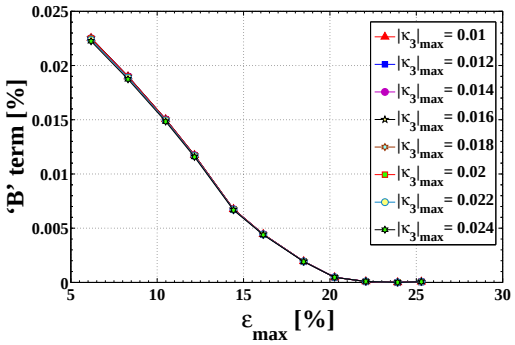

(b) Percentage of strain energy from the 'B' term

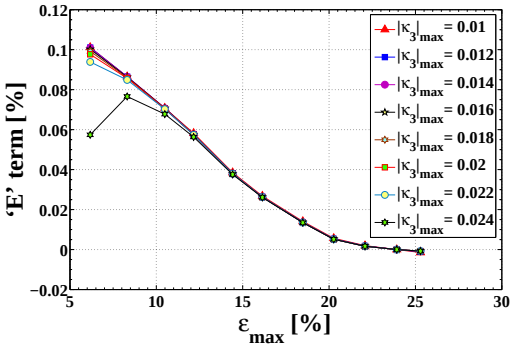

(c) Percentage of strain energy from the 'E' term

Figure E.1: Percentage contributions to the total strain energy in coupled extension-twist deformations corresponding to different ranges of imposed extension (axial strain %) and imposed twist (angle of twist per unit undeformed length in rad/Å) at points of maximum imposed ϵ.

It is observed, from Figures E.1, E.3, E.2, that although we obtain non-zero fit values for E in Figure 5.10(c), the contribution of the extension-twist coupling

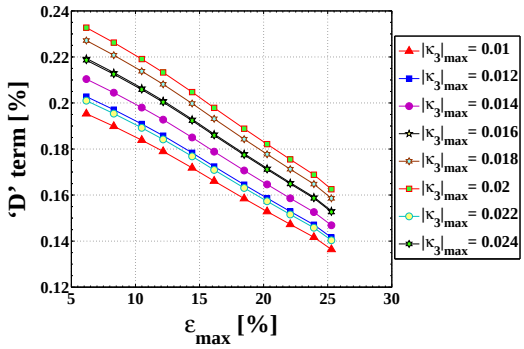

(a) Percentage of strain energy from the 'D' term

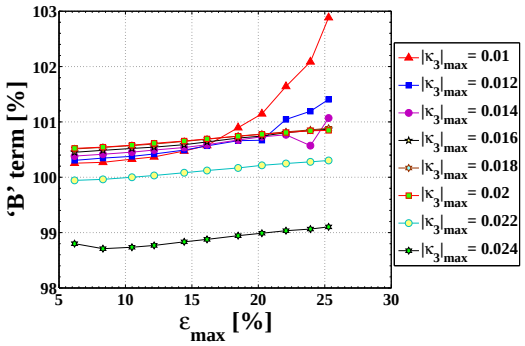

(b) Percentage of strain energy from the 'B' term

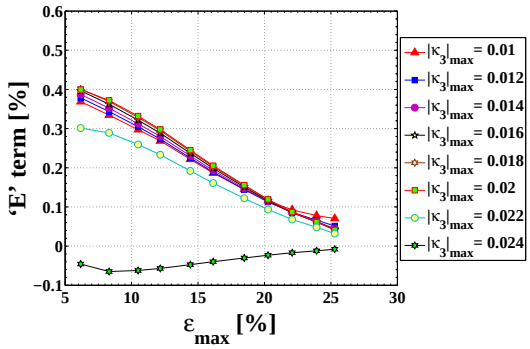

(c) Percentage of strain energy from the 'E' term

Figure E.2: Percentage contributions to the total strain energy in coupled extension-twist deformations corresponding to different ranges of imposed extension (axial strain %) and imposed twist (angle of twist per unit undeformed length in rad/Å) at points of maximum imposed $+\kappa_3$.

term to the total strain energy in imposed extension or twist is negligible (as mentioned in Section 5.5.2).

Further, instances when the contribution to the total strain energy from some of the terms is negative can be viewed as strain release modes (since positive strain energy is due to built-up strain, negative strain energy can be viewed as arising from strain release or relaxation – assuming no (inelastic) dissipation).

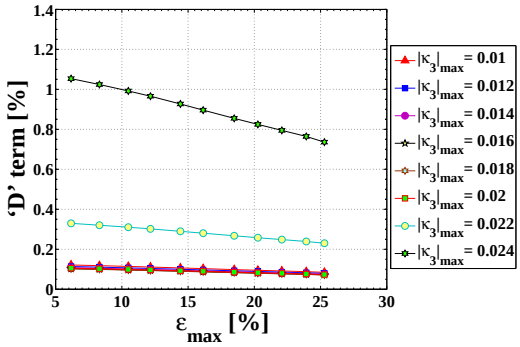

(a) Percentage of strain energy from the 'D' term

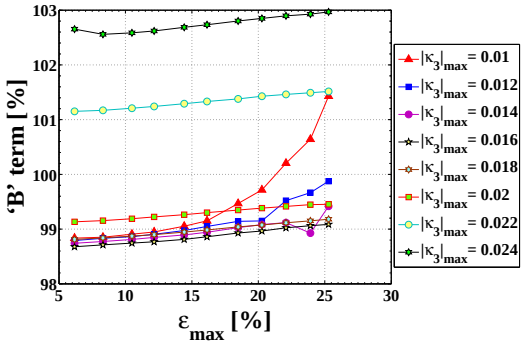

(b) Percentage of strain energy from the 'B' term

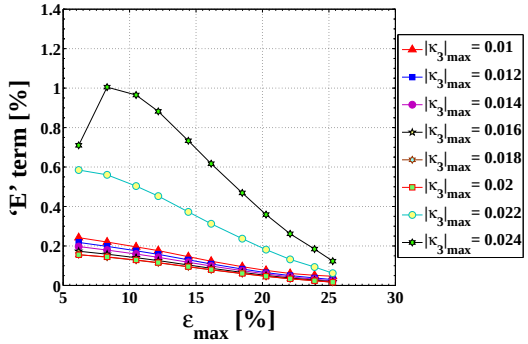

(c) Percentage of strain energy from the 'E' term

Figure E.3: Percentage contributions to the total strain energy in coupled extension-twist deformations corresponding to different ranges of imposed extension (axial strain %) and imposed twist (angle of twist per unit undeformed length in rad/Å) at points of maximum imposed $-\kappa_3$.

Also, instances when the strain energy contributions from the D, B, E terms do not add up exactly to the total strain energy can be viewed as ones in which a part of the total strain energy is stored in the A, C, F terms that are not accounted for in the extension-twist simulations, or as arising from the least-squares fitting approximation (Section 5.4).

Figures E.4, E.5, E.6, and E.7 show the percentage contributions of the bending, shear, and coupled bending-shear terms in Equation 5.20 at the points of maximum imposed $\nu_1, \nu_2, \kappa_2, \kappa_1$ respectively (corresponding to the same defor-

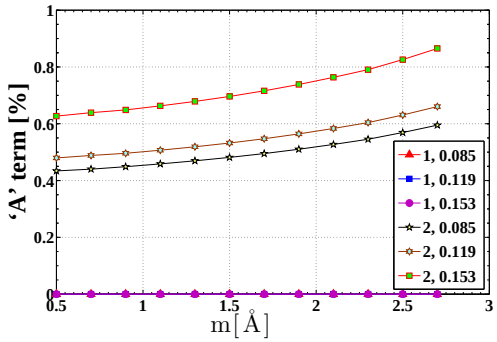

(a) Percentage of strain energy from the 'A' term

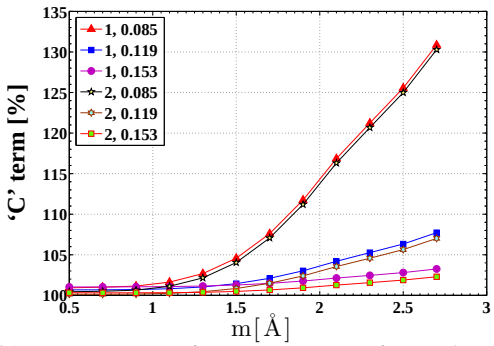

(b) Percentage of strain energy from the 'C' term

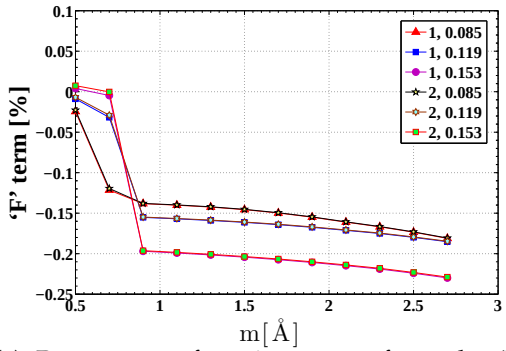

(c) Percentage of strain energy from the 'F' term

Figure E.4: Percentage contributions to the total strain energy in coupled bending-shear deformations at points of maximum imposed ν_1. Each point corresponds to a different range of imposed curvatures (reflected in the mid point deflections (m in Å – Figure 5.8)), and shear deformations (angles of rotation of cross-sections about in-plane axes (θ in radians – Figure 5.8)). In the legends, for example, '2, 0.085' indicates keeping and '1, 0.085' indicates dropping the $A\kappa_\alpha\kappa_\alpha$ term when ν_1 or ν_2 are imposed (of magnitude indicated by $\theta = 0.085$ rad, Figure 5.8) – Equation 5.26 and Section 5.5.

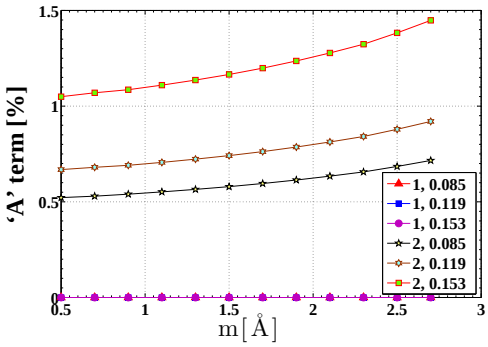

(a) Percentage of strain energy from the 'A' term

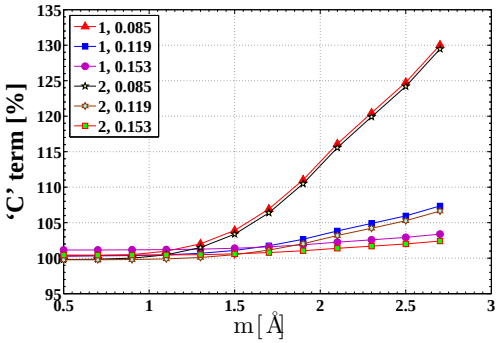

(b) Percentage of strain energy from the 'C' term

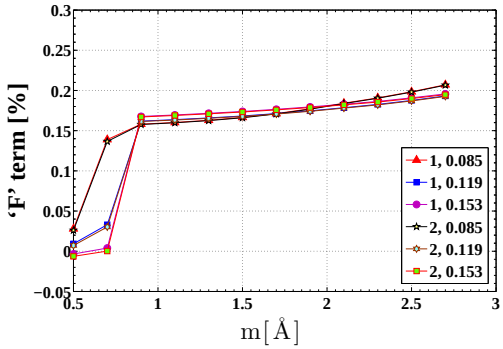

(c) Percentage of strain energy from the 'F' term

Figure E.5: Percentage contributions to the total strain energy in coupled bending-shear deformations at points of maximum imposed ν_2. Each point corresponds to a different range of imposed curvatures (reflected in the mid point deflections (m in Å – Figure 5.8)), and shear deformations (angles of rotation of cross-sections about in-plane axes (θ in radians – Figure 5.8)). In the legends, for example, '2, 0.085' indicates keeping and '1, 0.085' indicates dropping the $A\kappa_\alpha\kappa_\alpha$ term when ν_1 or ν_2 are imposed (of magnitude indicated by $\theta = 0.085$ rad, Figure 5.8) – Equation 5.26 and Section 5.5.

mation ranges as presented in Figures 5.11).

As expected, it is observed, from Figures E.4, E.5, E.6, and E.7, that most of the strain energy in each imposed deformation case is stored in the primary imposed deformation mode while the coupling term and the secondary induced effects contribute much smaller amounts to the overall strain energy (as men-

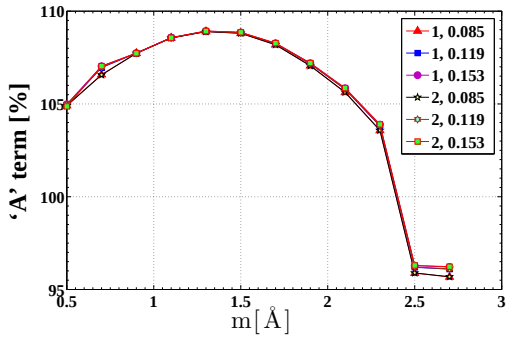

(a) Percentage of strain energy from the 'A' term

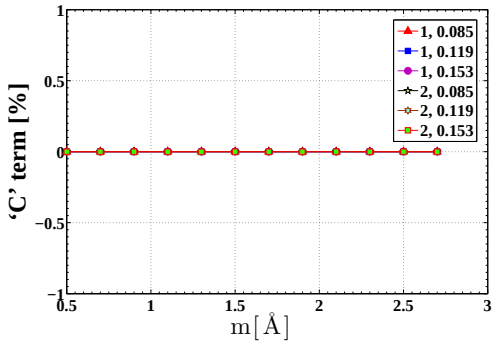

(b) Percentage of strain energy from the 'C' term

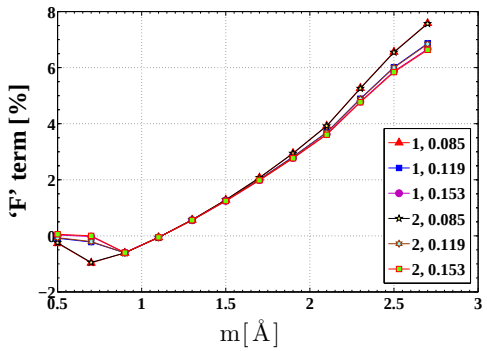

(c) Percentage of strain energy from the 'F' term

Figure E.6: Percentage contributions to the total strain energy in coupled bending-shear deformations at points of maximum imposed κ_2. Each point corresponds to a different range of imposed curvatures (reflected in the mid point deflections (m in Å – Figure 5.8)), and shear deformations (angles of rotation of cross-sections about in-plane axes (θ in radians – Figure 5.8)). In the legends, for example, '2, 0.085' indicates keeping and '1, 0.085' indicates dropping the $A\kappa_\alpha\kappa_\alpha$ term when ν_1 or ν_2 are imposed (of magnitude indicated by $\theta = 0.085$ rad, Figure 5.8) – Equation 5.26 and Section 5.5.

tioned in Section 5.5.3).

Further, as mentioned already, instances when the contribution to the total strain energy from one of the terms is negative can be viewed as strain release modes – assuming no (inelastic) dissipation. Also, instances when the strain energy contributions from the A, C, F terms do not add up exactly to the total

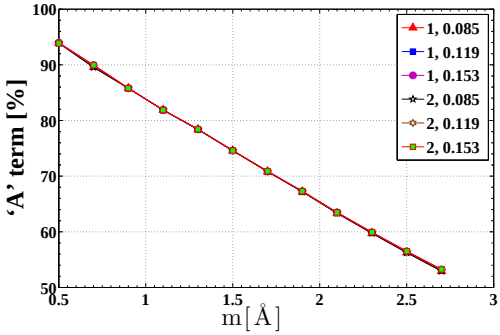

(a) Percentage of strain energy from the 'A' term

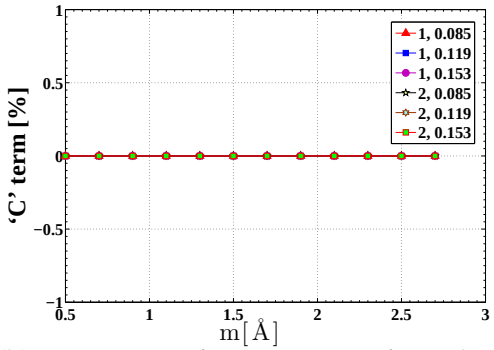

(b) Percentage of strain energy from the 'C' term

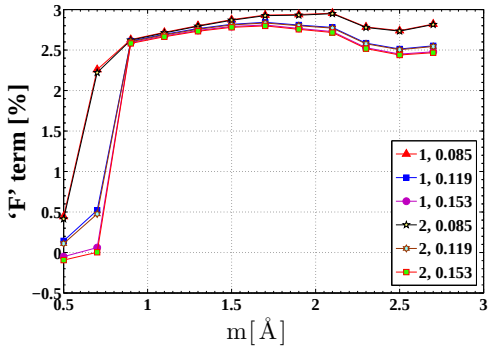

(c) Percentage of strain energy from the 'F' term

Figure E.7: Percentage contributions to the total strain energy in coupled bending-shear deformations at points of maximum imposed κ_1. Each point corresponds to a different range of imposed curvatures (reflected in the mid point deflections (m in Å – Figure 5.8)), and shear deformations (angles of rotation of cross-sections about in-plane axes (θ in radians – Figure 5.8)). In the legends, for example, '2, 0.085' indicates keeping and '1, 0.085' indicates dropping the $A\kappa_\alpha\kappa_\alpha$ term when ν_1 or ν_2 are imposed (of magnitude indicated by $\theta = 0.085$ rad, Figure 5.8) – Equation 5.26 and Section 5.5.

strain energy can be viewed as ones in which a part of the total strain energy is stored in the D, B, E terms that are not accounted for in the bending-shear simulations, or as arising from the least-squares fitting approximation (Section 5.4).

APPENDIX F

DEFORMABLE CROSS-SECTION COSSERAT ROD: KINEMATIC PRELIMINARIES

The present section describes the kinematic preliminaries of a Cosserat rod model that includes strain measures which can capture deformations of the cross-section (the special Cosserat rod model described in Section 5.2 assumes that cross-sections are rigid). The notation in the present section follows [69].

Similar to Section 5.2, $\{\mathbf{e}_1, \mathbf{e}_2, \mathbf{e}_3\}$ is defined as a fixed, right-handed, orthonormal basis that spans the reference configuration of the rod (Figure 5.1). It is assumed that the reference configuration is straight, stress-free, parallel to $\mathbf{e}_3$ with a prismatic cross-section, and that plane sections remain plane after deformation. The arc-length coordinate (of the centerline) in the undeformed rod is denoted by s, and the position vector (with respect to some fixed origin) of the material point originally at s in the reference configuration is denoted by $\mathbf{r}(s)$. It is assumed that $\{\mathbf{d}_1(s), \mathbf{d}_2(s), \mathbf{d}_3(s)\}$ denotes a linearly independent, right-handed triad of directors (neither of unit magnitude nor mutually orthogonal) attached to each cross-section in the deformed configuration, with $\mathbf{d}_3(s) \parallel \mathbf{r}'$, i.e., along the tangential direction to the deformed centroidal curve. Further, 'tangential deformation' is defined as deformation along $\mathbf{d}_3$, and 'cross-sectional deformation' as deformation in the plane perpendicular to $\mathbf{d}_3$ (i.e., normal to the deformed centroidal curve). Finally, with $d_{33} = \mathbf{d}_3 \cdot \mathbf{d}_3$, projections of $\mathbf{d}_1$ and $\mathbf{d}_2$ into the plane perpendicular to $\mathbf{d}_3$ are defined as follows:

$$\overline{\mathbf{d}_\alpha} = \mathbf{d}_\alpha - \frac{1}{d_{33}}(\mathbf{d}_\alpha \cdot \mathbf{d}_3)\mathbf{d}_3 \quad (\alpha = 1, 2) \quad , \tag{F.1}$$

giving

$$\overline{\mathbf{d}_\alpha} \cdot \overline{\mathbf{d}_\alpha} = \mathbf{d}_\alpha \cdot \mathbf{d}_\alpha - \frac{1}{d_{33}}(\mathbf{d}_\alpha \cdot \mathbf{d}_3)^2 \quad (\textit{no sum}; \quad \alpha = 1, 2) \tag{F.2}$$

and

$$\overline{\mathbf{d}_1} \cdot \overline{\mathbf{d}_2} = \mathbf{d}_1 \cdot \mathbf{d}_2 - \frac{1}{d_{33}}(\mathbf{d}_1 \cdot \mathbf{d}_3)(\mathbf{d}_2 \cdot \mathbf{d}_3) \quad , \tag{F.3}$$

and, further, automatically ensuring $\overline{\mathbf{d}_\alpha} \cdot \mathbf{d}_3 = 0 \quad (\alpha = 1, 2)$.

Now, the following deformation measures can be introduced:

(I) Tangential extension measured by $\sqrt{d_{33}} - 1$. This deformation mode can be constrained by setting $\mathbf{d}_3 \cdot \mathbf{d}_3 = \textit{constant}$.

(II) Tangential shear deformations measured by $\mathbf{d}_\alpha \cdot \mathbf{d}_3 \quad (\alpha = 1, 2)$. These deformation modes can be constrained by appropriately setting $\mathbf{d}_\alpha \cdot \mathbf{d}_3 = 0 \quad (\alpha = 1, 2)$.

(III) Cross-sectional extension measured by change in $|\overline{\mathbf{d}_\alpha}| \quad (\alpha = 1, 2)$. These deformation modes can be constrained in one of two possible ways:

(a) Setting $\overline{\mathbf{d}_\alpha} \cdot \overline{\mathbf{d}_\alpha} = \textit{constant} \quad (\textit{no sum}; \quad \alpha = 1, 2)$.

(b) Setting $\mathbf{d}_\alpha \cdot \mathbf{d}_\beta = \delta_{\alpha\beta} \quad (\alpha, \beta = 1, 2)$ ($\delta_{\alpha\beta}$ is the Kronecker delta function defined in Equation 3.36), or more generally, setting $\mathbf{d}_\alpha \cdot \mathbf{d}_\alpha = \textit{constant} \quad (\textit{no sum}; \quad \alpha = 1, 2)$.

The two possibilities, (III-a) and (III-b), are physically different as long as the tangential shear deformations are nonzero, i.e., $\mathbf{d}_\alpha \cdot \mathbf{d}_3 \neq 0 \quad (\alpha = 1, 2)$

– Equation F.2. Possibility (III-b) [1] assumes the dimensions of the material cross-section that was normal in the *reference* configuration to remain constant but allows the dimensions of the normal cross-section in the *present* configuration to change, whereas possibility (III-a) assumes the normal cross-sectional dimensions of the *present* configuration to remain constant while allowing the material cross-sectional dimensions of the *reference* configuration to change.

(IV) Cross-sectional shear deformation measured by change in angle between $\overline{\mathbf{d}_1}$ and $\overline{\mathbf{d}_2}$. Analogous to (III), this deformation mode can be constrained in one of two possible ways:

(a) Setting $\overline{\mathbf{d}_1} \cdot \overline{\mathbf{d}_2} = 0$.

(b) Setting $\mathbf{d}_1 \cdot \mathbf{d}_2 = 0$.

The two possibilities, (IV-a) and (IV-b), are physically different as long as the tangential shear deformations are nonzero, i.e., $\mathbf{d}_\alpha \cdot \mathbf{d}_3 \neq 0 \quad (\alpha = 1, 2)$ – Equation F.3. Possibility (IV-b) eliminates in-plane shear of the material cross-section that was normal in the *reference* configuration but allows in-plane shear of the normal cross-section in the *present* configuration, whereas possibility (IV-a) eliminates in-plane shear of the normal cross-section in the *present* configuration while allowing in-plane shear of the material cross-section that was normal in the *reference* configuration.

Based on the above definitions, a variety of restricted theories can be derived by imposing appropriate constraints [69]. A nonlinear Timoshenko rod is obtained by imposing constraints on modes (III) and (IV), while a nonlinear Bernoulli-Euler rod is obtained by imposing constraints on modes (II), (III), and (IV) [69]. The special Cosserat model, described in Section 5.2 and employed in

the present work, assumes cross-sections to be rigid and is realized by requiring the directors to be mutually orthonormal, i.e., to follow Equation 5.2.

BIBLIOGRAPHY

[1] Antman, S.S., 1995. Nonlinear problems of elasticity. Springer-Verlag, New York.

[2] Arroyo, M., Belytschko, T., 2002. An atomistic-based finite deformation membrane for single layer crystalline films. J. Mech. Phys. Solids 50, 1941-1977.

[3] Arroyo, M., Belytschko, T., 2004. Finite crystal elasticity of carbon nanotubes based on the exponential Cauchy-Born rule. Phys. Rev. B 69, 115415(1-11).

[4] Balaeff, A., Mahadevan, L., Schulten, K., 2006. Modeling DNA loops using the theory of elasticity. Phys. Rev. E 73, 031919(1-23).

[5] S. Baroni, A. Dal Corso, S. de Gironcoli, P. Giannozzi, C. Cavazzoni, G. Ballabio, S. Scandolo, G. Chiarotti, P. Focher, A. Pasquarello, K. Laasonen, A. Trave, R. Car, N. Marzari, A. Kokalj, PWscf (Plane-Wave Self-Consistent Field), http://www.pwscf.org/

[6] Belytschko, T., Xiao, S.P., Schatz, G.C., Ruoff, R.S., 2002. Atomistic simulations of nanotube fracture. Phys. Rev. B 65, 235430(1-8).

[7] Blöchl, P.E., Jepsen, O., Andersen, O.K., 1994. Improved tetrahedron method for Brillouin-zone integrations. Phys. Rev. B 49, 16223-16233.

[8] Brenner, D.W., 1990. Empirical potential for hydrocarbons for use in simulating the chemical vapor deposition of diamond films. Phys. Rev. B 42, 9458-9471.

[9] Brenner, D.W., Shenderova, O.A., Harrison, J.A., Stuart, S.J., Ni, B., Sinnott, S.B., 2002. A second-generation reactive empirical bond order (REBO) poten-

tial energy expression for hydrocarbons. J. Phys.: Condens. Matter 14, 783-802.

[10] Broyden, C.G., 1970. The convergence of a class of double-rank minimization algorithms. J. Inst. Math. Appl. 6, 76-90.

[11] Cao, D.Q., Liu, D., Wang, C.H.-T., 2005. Nonlinear dynamic modelling for MEMS components via the cosserat rod element. J. Micromech. and Microengg. 15(6), 1334-1343.

[12] Chandraseker, K., Mukherjee, S., 2006. Coupling of extension and twist in single-walled carbon nanotubes. ASME J. App. Mech. 73(2), 315-326.

[13] Chandraseker, K., Mukherjee, S., Mukherjee, Y.X., 2006. Modifications to the Cauchy-Born rule: Applications in the deformation of single-walled carbon nanotubes. Int. J. Solids and Structures 43, 7128-7144.

[14] Chandraseker, K., Mukherjee, S., 2007. Atomistic-continuum and *ab initio* estimation of the elastic moduli of single-walled carbon nanotubes. Comp. Mat. Sci. 40, 147-158.

[15] Chang, T., Gao, H., 2003. Size-dependent elastic properties of a single-walled carbon nanotube via a molecular mechanics model. J. Mech. Phys. Solids 51, 10591074.

[16] Cornwell, C.F., Wille, L.T., 1997. Elastic properties of single-walled carbon nanotubes in compression. Solid State Comm. 101, 555-558.

[17] Cousins, C., 1978. Inner elasticity. J. Phys. C 11, 4867-4879.

[18] Cramer, C.J., 2004. Essentials of Computational Chemistry: Theories and Models. Wiley, Ed. 2.

[19] Dewar, M.J.S., Zoebisch, E.G., Healy, E.F., Stewart, J.J.P., 1985. Development and use of quantum mechanical molecular models. 76. AM1: A new general purpose quantum mechanical molecular model. J. Americ. Chem. Soc. 107(13), 3902-3909.

[20] Dresselhaus, M.S., Dresselhaus, G., Jorio, A., 2004. Unusual properties and structure of carbon nanotubes. Annu. Rev. Mater. Res. 34, 247-278.

[21] Elstner, M., Porezag, D., Jungnickel, G., Elsner, J., Haugk, M., Frauenheim, Th., 1998. Self-consistent-charge density-functional tight-binding method for simulations of complex materials properties. Phys. Rev. B 58(11), 7260-7268.

[22] Elstner, M., Frauenheim, Th., Kaxiras, E., Seifert, G., Suhai, S., 2000. A self-consistent charge density-functional based tight-binding scheme for large biomolecules. phys. stat. sol. (b) 217, 357-376.

[23] Ericksen, J.L., 1984. The Cauchy and Born hypotheses for crystals. In: Gurtin, M.E. (Ed.), Phase transformations and material instabilities in solids. Academic Press, New York, 61-77.

[24] Fago, M., Hayes, R.L., Carter, E.A., Ortiz, M., 2004. Density-functional-theory-based local quasicontinuum method: Prediction of dislocation nucleation. Phys. Rev. B 70, 100102(R).

[25] Fantini, C., Jorio, A., Santos, A.P., Peressinotto, V.S.T., Pimenta, M.A., 2007. Characterization of DNA-wrapped carbon nanotubes by resonance Raman and optical absorption spectroscopies. Chem. Phys. Lett. 439, 138-142.

[26] Fletcher, R., 1970. A new approach to variable metric algorithms. Comp. J. 13, 317-322.

[27] Frauenheim, Th., Seifert, G., Elstner, M., Niehaus, T., Köhler, C., Amkreutz, M., Sternberg, M., Hajnal, Z., Di Carlo, A., Suhai, S., 2002. Atomistic simulations of complex materials: Ground-state and excited-state properties. J. Phys.: Condens. Matter 14, 3015-3047.

[28] Fung, Y.C., Tong, P., 2001. Classical and Computational Solid Mechanics. World Scientific, Singapore.

[29] Garg, A., Han, J., Sinnott, S.B., 1998. Interactions of carbon-nanotubule proximal probe tips with diamond and graphene. Phys. Rev. Lett. 81, 2260-2263.

[30] Gartstein, Yu.N., Zakhidov, A.A., Baughman, R.H., 2003. Mechanical and electromechanical coupling in carbon nanotube distortions. Phys. Rev. B 68, 115415(1-11).

[31] Geng, J., Chang, T., 2006. Nonlinear stick-spiral model for predicting mechanical behavior of single-walled carbon nanotubes. Phys. Rev. B 74, 245428(1-13).

[32] Golberg, D., Bando, Y., Tang, C.C., Zhi, C.Y., 2007. Boron nitride nanotubes. Advanced Materials 19(18), 2413-2432.

[33] Goldfarb, D., 1970. A family of variable metric updates derived by variational means. Math. Comput. 24, 23-26.

[34] Gould, T., Burton, D.A., 2006. A Cosserat rod model with microstructure. New J. of Phys. 8, 137(1-17).

[35] Govindjee, S., Sackman, J.L., 1999. On the use of continuum mechanics to estimate the properties of nanotubes. Solid State Comm. 110, 227-230.

[36] Goyal, S., Perkins, N.C., Lee, C.L., 2005. Nonlinear dynamics and loop formation in Kirchhoff rods with implications to the mechanics of DNA and cables. J. Comp. Phys. 209, 371-389.

[37] Gradshteyn, I.S., Ryzhik, I. M., 2000. Tables of integrals, series, and products, 6th ed. San Diego, CA: Academic Press, 1097-1098.

[38] Healey, T.J., 2002. Material symmetry and chirality in nonlinearly elastic rods. Mathematics and Mechanics of Solids 7, 405-420.

[39] Hernández, E., Goze, C., Bernier, P., Rubio, A., 1998. Elastic properties of C and $B_xC_yN_z$ composite nanotubes. Phys. Rev. Lett. 80, 4502-4505.

[40] Hernández, E., Goze, C., Bernier, P., Rubio, A., 1999. Elastic properties of single-wall nanotubes. Appl. Phys. A: Mater. Sci. Process. 68, 287-292.

[41] Hohenberg, P., Kohn, W., 1964. Inhomogeneous electron gas. Phys. Rev. 136, B864.

[42] Iijima, S., Brabec, C., Maiti, A., Bernholc, J., 1996. Structural flexibility of carbon nanotubes. J. Chem. Phys. 104, 2089-2092.

[43] Ismail-Beigi, S., Arias, T.A., 2000. New algebraic formulation of density functional calculation. Comp. Phys. Comm. 128, 1-45.

[44] Jiang, H., Zhang, P., Liu, B., Huang, Y., Geubelle, P.H., Gao, H., Hwang, K.C., 2003. The effect of nanotube radius on the constitutive model for carbon nanotubes. J. Comput. Mat. Sc. 28, 429-442.

[45] Kamien, R.D., Lubensky, T.C., Nelson, P., O'Hern, C.S., 1997. Direct determination of DNA twist-stretch coupling. Europhys. Lett. 38(3), 237-242.

[46] Kohn, W., Sham, L.J., 1965. Self-consistent equations including exchange and correlation effects. Phys. Rev. 140, A1133.

[47] Krishnan, A., Dujardin, E., Ebbesen, T.W., Yianilos, P.N., Treacy, M.M.J., 1998. Young's modulus of single-walled nanotubes. Phys. Rev. B 58, 14013-14019.

[48] Kudin, K.N., Scuseria, G.E., Yakobson, B.I., 2001. C_2F, BN, and C nanoshell elasticity from *ab initio* computations. Phys. Rev. B 64, 235406.

[49] Lennard-Jones, J.E., 1931. Cohesion. Proceedings of the Physical Society 43, 461-482.

[50] Li, C., Chou, T.-W., 2004. Vibrational behaviors of multiwalled-carbon-nanotube-based nanomechanical resonators. App. Phys. Lett. 84, 121-123.

[51] Liang, H., Upmanyu, M., 2006. Axial-strain-induced torsion in single-walled carbon nanotubes. Phys. Rev. Lett. 96, 165501(1-4).

[52] Liu, B., Jiang, H., Johnson, H.T., Huang, Y., 2004. The influence of mechanical deformation on the electrical properties of single wall carbon nanotubes. J. Mech. Phys. Solids 52, 1-26.

[53] Lu, J.P., 1997. Elastic properties of carbon nanotubes and nanoropes. Phys. Rev. Lett. 79, 1297-1300.

[54] Lu, J.P., 1997. Elastic properties of single and multilayered nanotubes. J. Phys. Chem. Solids 58, 1649-1652.

[55] Marko, J.F., Siggia, E.D., 1994. Bending and twisting elasticity of DNA. Macromolecules 27, 981-988.

[56] Marsden, J.E., Hughes, T.J., 1983. Mathematical foundations of elasticity. Prentice-Hall, Englewood Cliffs, NJ.

[57] Maruyama, S., Department of Mechanical Engineering, University of Tokyo.
http://www.photon.t.u-tokyo.ac.jp/~maruyama/wrapping3/wrapping.html

[58] Mielke, S.L., Troya, D., Zhang, S., Li, J-.L., Xiao, S., Car, R., Ruoff, R., Schatz, G.C., Belytschko, T., 2004. The role of vacancy defects and holes in the fracture of carbon nanotubes. Chem. Phys. Lett. 390, 413-420.

[59] Molina, J.M., Savinsky, S.S., Khokhriakov, N.V., 1996. A tight-binding model for calculations of structures and properties of graphitic nanotubes. J. Chem. Phys. 104, 4652-4656.

[60] Monkhorst, H.J., Pack, J.D., 1976. Special points for Brillouin-zone integrations. Phys. Rev. B 13, 5188-5192.

[61] Nardelli, M.B., Yakobson, B.I., Bernholc, J., 1998. Brittle and ductile behavior in carbon nanotubes. Phys. Rev. Lett. 81, 4656-4659.

[62] Ogden, R.W., 1984. Non-linear elastic deformations. Ellis Horwood Series in Mathematics and its Applications, UK.

[63] Pantano, A., Boyce, M.C., Parks, D.M., 2003. Nonlinear structural mechanics based modeling of carbon nanotube deformation. Phys. Rev. Lett. 91, 145504(1-4).

[64] Perdew, J.P., Burke, K., Ernzerhof, M., 1996. Generalized gradient approximation made simple. Phys. Rev. Lett. 77, 3865-3868.

[65] Pople, J., Beveridge, D., 1970. Approximate molecular orbital theory. McGraw-Hill.

[66] Popov, V.N., Van Doren, V.E., Balkanski, M., 2000. Elastic properties of single-walled carbon nanotubes. Phys. Rev. B 61, 3078-3084.

[67] Robertson, D.H., Brenner, D.W., Mintmire, J.W., 1992. Energetics of nanoscale graphitic tubules. Phys. Rev. B 45, 12592-12595.

[68] Ru, C.Q., 2000. Effective bending stiffness of carbon nanotubes. Phys. Rev. B 62, 9973-9976.

[69] Rubin, M.B., 2000. Cosserat theories: Shells, rods and points. Kluwer Academic Publishers, The Netherlands.

[70] Saito, R., Dresselhaus, G., Dresselhaus, M.S., 1998. Physical properties of carbon nanotubes. Imperial College Press, London.

[71] Salvetat, J.-P., Briggs, G.A.D, Bonard, J.M., Bacsa, R.R., Kulik, A.J., Stöckli, T., Burnham, N.A., Forró, L., 1999. Elastic and shear moduli of single-walled carbon nanotube ropes. Phys. Rev. Lett. 82, 944-947.

[72] Salvetat, J.-P., Bonard, J.-M., Thomson, N.H., Kulik, A.J., Forró, L., Benoit, W., Zuppiroli, L., 1999. Mechanical properties of carbon nanotubes. App. Phys A: Mat. Sci. and Process. 69, 255-260.

[73] Samsonidze, G.G., Samsonidze, G.G., Yakobson, B.I., 2002. Kinetic theory of symmetry-dependent strength in carbon nanotubes. Phys. Rev. Lett. 88, 065501.

[74] Sáncez-Portal, D., Artacho, E., Soler, J.M., Rubio, A., Ordejón, P., 1999. *Ab*

initio structural, elastic, and vibrational properties of carbon nanotubes. Phys. Rev. B 59, 12 678.

[75] Sazonova, V., Yaish, Y., Üstünel, H., Roundy, D., Arias, T.A., McEuen, P.L., 2004. A tunable carbon nanotube electromechanical oscillator. Nature 431, 284-287.

[76] Sha, J., Niu, J., Ma, X., Xu, J., Zhang, X., Yang, Q., Yang., D., 2002. Silicon nanotubes. Advanced Materials 14(17), 1219-1221.

[77] Shan, B., Lakatos, G.W., Peng, S., Cho, K., 2005. First-principles study of band-gap change in deformed nanotubes. Appl. Phys. Lett. 87, 173109(1-3).

[78] Shanno, D.F., 1970. Conditioning of quasi-Newton methods for function minimization. Math. Comput. 24, 647-656.

[79] Shenoy, V., Miller, R., Tadmor, E., Rodney, D., Phillips, R., Ortiz, M., 1999. An adaptive finite element approach to atomic-scale mechanics – the quasicontinuum method. J. Mech. Phys. Solids 47, 611-642.

[80] Srivastava, D., Menon, M., Cho, K., 1999. Nanoplasticity of single-wall carbon nanotubes under uniaxial compression. Phys. Rev. Lett. 83, 2973-2976.

[81] Steigmann, D.J., Ogden, R.W., 1999. Elastic surface-substrate interactions. Proc. R. Soc. Lond. A 455, 437-474.

[82] Stewart, J.J.P., 1989. Optimization of parameters for semiempirical methods I. Method. J. Comput. Chem. 10(2), 209-220.

[83] Stewart, J.J.P., 1989. Optimization of parameters for semiempirical methods II. Applications. J. Comput. Chem. 10(2), 221-264.

[84] Tadmor, E., Smith, G., Bernstein, N., Kaxiras, E., 1996. Quasicontinuum analysis of defects in solids. Philos. Mag. A 73(6), 1529-1563.

[85] Tadmor, E.B., Smith, G.S., Bernstein, N., Kaxiras, E., 1999. Mixed finite element and atomistic formulation for complex crystals. Phys. Rev. B 59, 235-245.

[86] Tersoff, J., 1988. New empirical approach for the structure and energy of covalent systems. Phys. Rev. B 37, 6991-7000.

[87] Üstünel, H., Roundy, D., Arias, T.A., 2005. Modeling a suspended nanotube oscillator. Nanoletters 5(3), 523-526.

[88] Van Lier, G., Van Alsenoy, C., Van Doren, V., Geerlings, P., 2000. *Ab initio* study of the elastic properties of single-walled carbon nanotubes and graphene. Chem. Phys. Lett. 326, 181-185.

[89] Vanderbilt, D., 1990. Soft self-consistent pseudopotentials in a generalized eigenvalue formalism. Phys. Rev. B 41, 7892-7895.

[90] Villa, E., Balaeff, A., Mahadevan, L., Schulten, K., 2004. Multiscale method for simulating protein-DNA complexes. Multiscale Model. Simul. 2(4), 527-553.

[91] Wei, C., Cho, K., Srivastava, D., 2003. Tensile strength of carbon nanotubes under realistic temperature and strain rate. Phys. Rev. B 67, 115407.

[92] White, C.T., Robertson, D.H., Mintmire, J.W., 1993. Helical and rotational symmetries of nanoscale graphitic tubules. Phys. Rev. B 47, 5485-5488.

[93] Xiao, T., Xu, X., Liao, K., 2004. Characterization of nonlinear elasticity and elastic instability in single-walled carbon nanotubes. J. App. Phys. 95, 8145-8148.

[94] Yakobson, B.I., 1998. Mechanical relaxation and "intramolecular" plasticity in carbon nanotubes. Appl. Phys. Lett. 72, 918-920.

[95] Yakobson, B.I., Avouris, Ph., 2001. Mechanical properties of carbon nanotubes. In: Dresselhaus, M.S., Dresselhaus, G., Avouris, Ph. (Eds.), Topics in Applied Physics, Springer-Verlag, Heidelberg, Germany, Carbon Nanotubes 80, 287-329.

[96] Yakobson, B.I., Brabec, C.J., Bernholc, J., 1996. Nanomechanics of carbon tubes: Instabilities beyond linear response. Phys. Rev. Lett. 76, 2511-2514.

[97] Yakobson, B.I., Campbell, M.P., Brabec, C.J., Bernholc, J., 1997. High strain rate fracture and C-chain unraveling in carbon nanotubes. J. Comput. Mat. Sc. 8, 341-348.

[98] Yang, J.Z, Weinan, E., 2006. Generalized Cauchy-Born rules for elastic deformation of sheets, plates, and rods: Derivation of continuum models from atomistic models. Phys. Rev. B 74, 184110(1-11).

[99] Yu, M.-F., 2004. Fundamental mechanical properties of carbon nanotubes: Current understanding and the related experimental studies. ASME J. Engg. Mat. and Tech. 126, 271-278.

[100] Yu, M.F., Lourie, O., Dyer, M.J., Moloni, K., Kelly, T.F., Ruoff, R.S., 2000. Strength and breaking mechanism of multiwalled carbon nanotubes under tensile load. Science 287, 637-640.

[101] Zhang, P., Huang, Y., Geubelle, P.H., Klein, P.A., Hwang, K.C., 2002. The elastic modulus of single-wall carbon nanotubes: A continuum analysis incorporating interatomic potentials. Int. J. Solids and Structures 39, 3893-3906.

[102] Zhou, G., Duan, W., Gu, B., 2001. First-principles study on morphology and mechanical properties of single-walled carbon nanotube. Chem. Phys. Lett. 333, 344-349.